SAND REPORT
SAND2005-0292
Unlimited Release
Printed May 2005

2005 Research Briefs
Materials and Process Sciences Center

Michael J. Cieslak

Prepared by
Sandia National Laboratories
Albuquerque, New Mexico 87185 and Livermore, California 94550

Sandia is a multiprogram laboratory operated by Sandia Corporation,
a Lockheed Martin Company, for the United States Department of Energy's
National Nuclear Security Administration under Contract DE-AC04-94-AL85000.

Sandia National Laboratories

Issued by Sandia National Laboratories, operated for the United States Department of Energy by Sandia Corporation.

Available to DOE and DOE contractors from
U.S. Department of Energy
Office of Scientific and Technical Information
P.O. Box 62
Oak Ridge, TN 37831

Telephone: (865)576-8401
Facsimile: (865)576-5728
E-Mail: reports@adonis.osti.gov
Online ordering: http://www.doe.gov/bridge

Available to the public from
U.S. Department of Commerce
National Technical Information Service
5285 Port Royal Rd
Springfield, VA 22161

Telephone: (800)553-6847
Facsimile: (703)605-6900
E-Mail: orders@ntis.fedworld.gov
Online order: http://www.ntis.gov/help/ordermethods.asp?loc=7-4-0#online

SAND2005-0292
Unlimited Release
Printed May 2005

2005 Research Briefs: Materials and Process Sciences Center

Michael J. Cieslak
Materials and Process Sciences Center
Sandia National Laboratories
P.O. Box 5800
Albuquerque, NM 87185-0887

Abstract

This report is the latest in a continuing series that highlights the recent technical accomplishments associated with the work being performed within the Materials and Process Sciences Center. Our research and development activities primarily address the materials-engineering needs of Sandia's Nuclear-Weapons (NW) program. In addition, we have significant efforts that support programs managed by the other laboratory business units. Our wide range of activities occurs within six thematic areas: Materials Aging and Reliability, Scientifically Engineered Materials, Materials Processing, Materials Characterization, Materials for Microsystems, and Materials Modeling and Simulation. We believe these highlights collectively demonstrate the importance that a strong materials-science base has on the ultimate success of the NW program and the overall DOE technology portfolio.

Acknowledgment

First, we want to gratefully acknowledge the importance of our many customers who not only sponsor our work, but also provide valuable guidance, feedback, and programmatic motivation. In addition, we acknowledge the substantial and significant contributions of our co-workers from within many other organizations at Sandia, from universities, and from industry.

Editors:
C. L. Porter
J. W. Braithwaite
R. J. Salzbrenner

Introductory Message from the Center Director

The core responsibility of the Materials and Process Sciences Center is to provide materials-engineering support to Sandia's Nuclear-Weapons (NW) program. As a foundational Science and Technology organization for the Laboratories, the Center also performs R&D activities that are sponsored by the other laboratory business areas (Energy & Infrastructure Assurance, Nonproliferation and Assessments, Military Technologies & Applications, and Homeland Security). Importantly, our primary product is a science-based *knowledge* of material properties and behavior and the processes to more effectively produce, transform, and analyze them. Accordingly, our sponsors engage us in a broad range of research, development, and applications activities.

This report is the latest in a continuing series that contain highlights of recent specific accomplishments. These briefs are organized into sections that involve the Center's core capabilities: three prime thematic areas (Materials Aging and Reliability, Scientifically Engineered Materials, Materials Processing), and two of our three crosscutting areas (Materials Characterization and Materials for Microsystems). The goal of the work in *Materials Aging and Reliability* is to understand the chemical and physical mechanisms that cause materials properties to change and then develop mechanistic-based models to predict how these changes affect component reliability. Activities in the *Scientifically Engineered Materials* area focus on developing new and replacement materials with desired specific properties or performance characteristics through an understanding of how materials properties depend on composition, microstructure, and manufacturing processes. Within the *Materials Processing* theme, the knowledge base needed to understand, characterize, model, and ultimately control the materials fabrication technologies that are critical to hardware production is generated. Success with all of these activities requires the availability of effective tools and techniques to characterize materials. Thus, the focus of the crosscutting *Materials Characterization* area is to develop and apply analytical techniques to detect and measure chemical and structural information about materials at various temporal and spatial scales, down to the nanoscale. Our directed work in *Materials for Microsystems* to support Sandia's emerging microsystem initiative involves aspects of the other three thematic areas, but focused on the specific challenges associated with the inherently small-length scale of these devices. The third crosscutting Center capability involves the mathematical modeling and computational simulation of materials behavior and fabrication processes. Specific modeling accomplishments are described within the context of the other five topical sections.

Consideration of this entire set of highlights in conjunction with the needs of the non-nuclear aspects of the NNSA's NW program provides a sense of the importance that a strong materials-science base has on the program's ultimate success. These briefs also demonstrate the connections between materials science and the breadth of the overall DOE technology portfolio.

We welcome your questions and comments on the work being performed in the Materials and Process Sciences Center. Contact information along with additional organizational and technical descriptions of what we do can be found by visiting our website at http://www.sandia.gov/materials/science.

Michael J. Cieslak

TABLE OF CONTENTS

MATERIALS AGING

MATERIALS CHARACTERIZATION

MATERIALS CHARACTERIZATION, cont.

MATERIALS FOR MICROSYSTEMS

MATERIALS PROCESSING

MATERIALS PROCESSING, cont.

MATERIALS SYNTHESIS

MATERIALS SYNTHESIS, cont.

Aging and Reliability of Low Temperature Co-Fired Ceramics (LTCC's)

R. Tandon, S. J. Glass, C. Newton, S. Monroe

Motivation: Ceramic and glass materials are used extensively in non-nuclear components in the weapons stockpile. These materials often provide electrical insulation and/or hermetic-environmental barriers required for device function. The low fracture toughness and brittle nature of ceramics and glasses make their mechanical behavior highly sensitive to the presence of flaws. Large defects and the failures they produce are usually detected during processing and assembly. However, sub-critical flaws exist in all ceramic and glass parts that are below the detection limits of non-destructive tests. Often features in the microstructure (pores, second phase materials etc.) may themselves act as the failure causing flaw. These sub-critical flaws may extend, over time periods of days to years, under the action of residual stresses, stresses due to thermal cycling and/or due to lowering of resistance to fracture of the material due to chemical attack at the crack tip (mostly due to moisture). The growth of these cracks may compromise device function by severing electrical connections, causing loss of hermeticity, or in severe cases causing fractures.

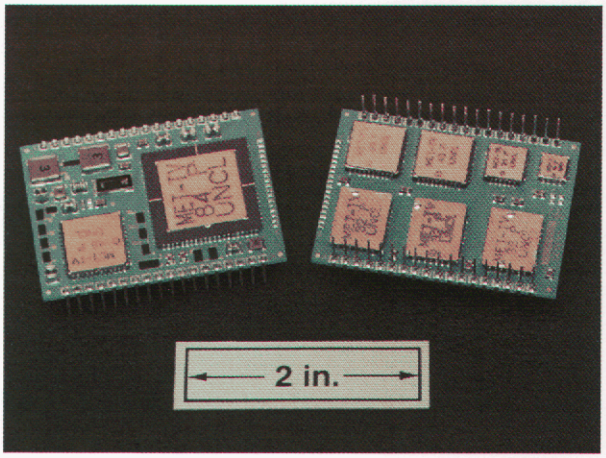

Figure 1. LTCC material in a Microelectronic Assembly

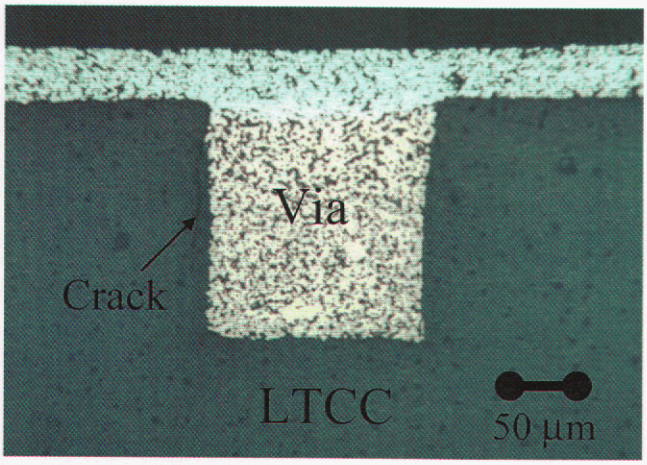

Figure 2. Crack in LTCC material (blue) near a metal-glass composite via.

LTCC's (Low Temperature Co-fired Ceramics) are candidate materials for use in interconnect platforms for many microelectronic devices. One device in the stockpile utilizing a LTCC substrate is shown in Figure 1. Cracking around metal-containing vias has been observed (Figure 2). If these cracks grow in the subcritical crack growth (SCG) mode, there is a possibility of loss of electrical connection.

A number of design methodologies now exist for predicting the fracture probability (reliability) and lifetimes for ceramic materials based on their time-independent and time-dependent strength properties. Finite element calculations are used to predict stresses in

components, and these results along with the strength properties of the material are input into life assessment software to provide engineering estimates of expected lifetime. The accuracy of the results depends on the incorporation of the correct physics in the finite element calculations, quality of the available materials response data, methods used for data analysis, and knowledge of the stress and environmental conditions encountered during the component's service life.

Accomplishment: We measured the time-dependent and time-independent fracture properties, in controlled humidity environments, for a LTCC material. Results for different humidity conditions are shown in Figure 3. Consistent with the behavior of other ceramic and glass materials, humidity and stressing rate have strong effects on the strength of this material. The crack velocity, v, can be expressed using an empirical function, $v = AK^n$, where K is the applied stress intensity factor, and A, n are SCG parameters. The data in Fig. 3 have been used to obtain the values of A, n for this LTCC material. It is found that the exponent n is ~ 24 for both extremes of humidity, whereas the value of A differs, being significantly higher in the higher humidity. This indicates that this LTCC will have a shorter lifetime when it is under stress in high humidity environments. The crack velocity law was used to estimate lifetimes at different stress levels. We determined that the correct assignment of the inert strength value is critical for lifetime predictions using this approach, and we have outlined an experimental plan to obtain this value. We have also determined the appropriate stressing rates for obtaining true SCG parameters and have compared our results to available literature values.

Significance: The capability to accurately predict fracture in brittle components is critical at several levels: during new design, during production, and once components are in the field. Fracture susceptibility predictions and lifetime considerations are used to refine design concepts and pick alternative materials for new components. Fracture mechanics based models are used to support failure analysis for production. As materials data and analysis techniques improve, fielded hardware can be analyzed for its end of life.

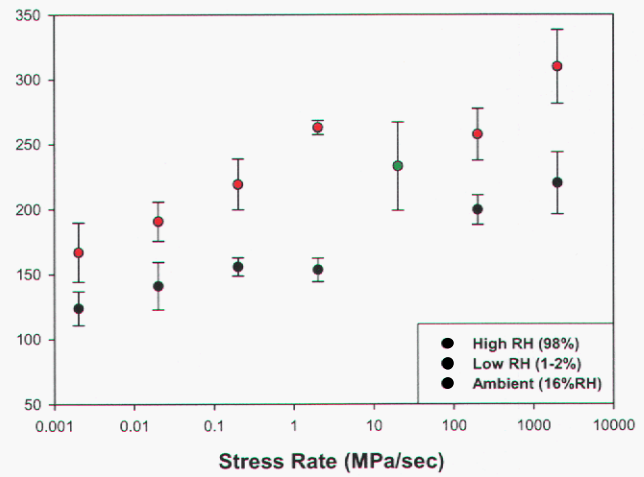

Figure 3. Biaxial flexure strength vs. stressing rate for different humidity conditions for LTCC. Five samples were tested at each rate.

Contact: Rajan Tandon, Microsystem Materials and Mechanical Behavior Dept.
Phone: (505) 844-1187
Fax: (505) 844-7910
Email: rtandon@sandia.gov

NMR Structural Refinement of Absorbate Environments: Application to Zeolite Desiccants

T. Alam, G. Holland

Motivation: Adsorbates in inorganic materials such as zeolites play a crucial role in the performance and chemical activity of these materials. Zeolites are extensively used in a wide variety of applications including catalysis, gas separation, and as drying agents. Within the weapons stockpile, zeolite desiccants are used in a wide variety of systems. Small molecules will adsorb in the cage-like structures of these aluminosilicate materials if the adsorbate has a critical diameter smaller than the pore size of the zeolite. Varying the cations present in the cage can control this pore size, and in many instances the cation sites are the dominant site of adsorption. Structural details of the local environment formed between adsorbates and cation sites is still not well understood in zeolites, but solid state NMR techniques allow structural details to be obtained.

Accomplishment: This laboratory has recently explored the cation/adsorbate structure for the zeolite-A molecular sieves. It has been shown that the presence of NH_3 (produced by material off-gassing) influences the adsorption properties of H_2O within the zeolite-A desiccants. By utilizing solid-state NMR spectroscopy the adsorption of ^{15}N-labeled ammonia (NH_3) gas on the Type 3A desiccant has been probed. Using ^{15}N-^{23}Na and ^{15}N-^{27}Al rotational echo adiabatic passage double resonance (REAPDOR) NMR experiments (Figure 1) it was possible to determine the N-Na and N-Al distances for the adsorbed NH_3 within the zeolites. From the analysis of the REAPDOR curves the ^{15}N-^{23}Na and ^{15}N-^{27}Al distances were determined to be 3.3 ± 0.1 and 3.5 ± 0.2 Å, respectively. These distance constraints were used to produce a structural model of the NH3 binding site at low concentrations. Figure 2 shows the resulting structural model.

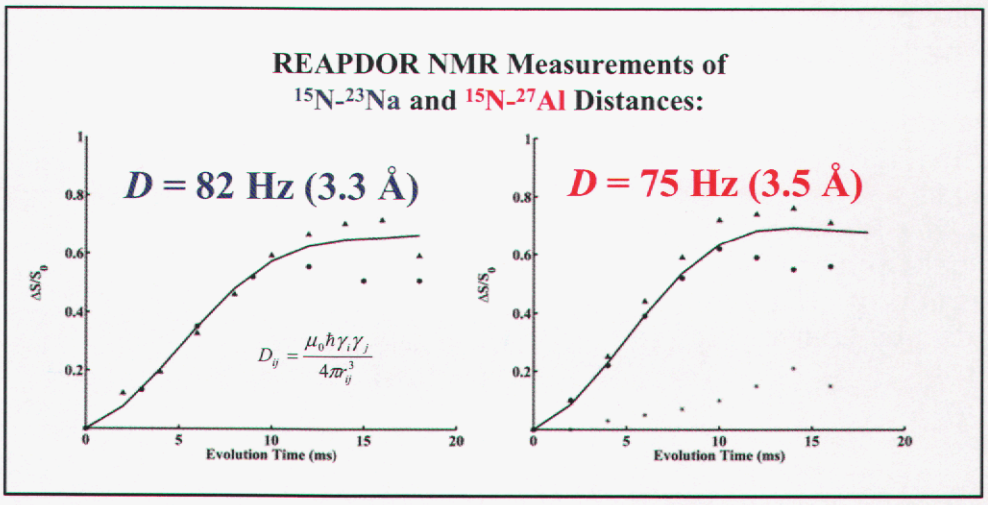

Figure 1. The 15N/23Na and 15N/27AL REAPDOR NMR build-up curves for the rigidly bound NH3 site (δ = -386.4 ppm) in 3A zeolite molecular sieve at 21 °C. These distance constraints are used as input for the creation of a structural model.

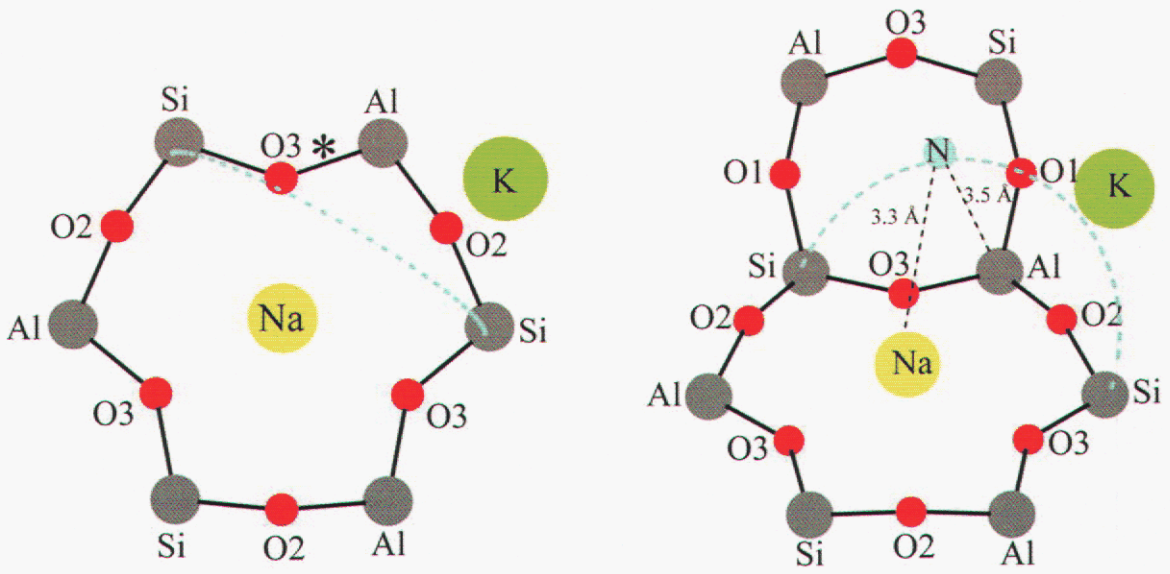

Figure 2. Ammonia adsorption site with the N-Na and N-Al distances measured with REAPDOR NMR. The 1H/23Na and 1H/27Al REAPDOR measurements indicate that the protons point toward the 4-ring to allow for hydrogen bonding at the O3 and O1 sites.

Significance: The details obtained from these NMR experiments represent some of the first structural information about the binding sites of NH_3 in zeolites. The presence of multiple binding sites for ammonia adsorption has been identified and quantified using NMR spectroscopy. The first NH_3 binding site occupied, is also the sight with the highest binding efficiency, but only represents a fraction of the total binding environments. These NMR results suggest that NH_3 in this initial tight binding site blocks the pore opening within the zeolite, and may be responsible for the reduced water uptake performance of the Type 3A desiccant in the presence of NH_3. These multi-nuclear NMR results were obtained at ambient temperatures, and did not require the use of frozen conditions to resolve the structure. More importantly, this NMR structural information was obtained for low absorbate loadings in a randomly oriented powder, without the requirement of high quality crystals. These types of experiments can readily be applied to amorphous materials. Structural information from diffraction type experiments is not easily obtained at these low absorbate loadings. These results also represent the first NMR experiments that provide structural constraints between the adsorbate and both a framework and cation nuclei. Given the number of different nuclei accessible to NMR investigations, these types of experiments can find utility in a wide range of materials and systems.

Contact: Todd M. Alam, Biomolecular & Chemical Analysis Dept.
Phone: (505) 844-1225
Fax: (505) 844-2974
Email: tmalam@sandia.gov

A Combinatorial Technique for High Throughput Electrochemical Characterization

F. Wall, M. Martinez

Motivation: A critical component of all batteries and fuel cells is the catalyst on which species are oxidized or reduced. For systems where the electron transfer reaction occurs at a metal-solution interface, electrochemical characterization is an ideal tool for identifying promising catalyst materials. However, fabricating and testing electrodes one-by-one can be costly and time consuming and may place practical limits on the scope of a search for new and better catalysts. Combinatorial techniques offer a promising methodology for increasing the phase space that can be explored, thus improving the probability of finding more efficient catalyst materials. The technique described here was developed to characterize combinations of materials and environment for glucose oxidation in support of the bio-micro fuel cell grand challenge LDRD program.

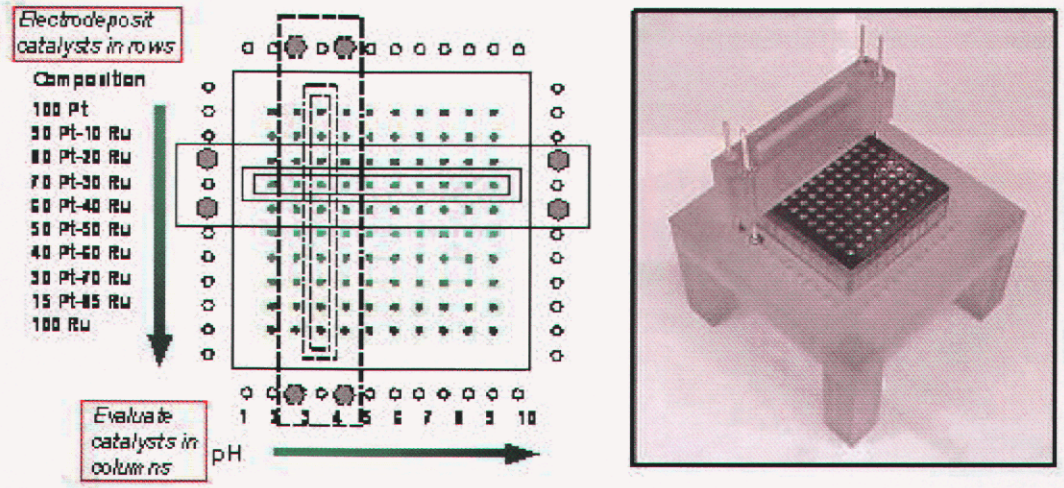

Figure 1. 100-element electrode for performing combinatorial studies.

Accomplishment: A combinatorial approach to catalyst fabrication and characterization was developed that relies on fabricating and testing electrodes in groups of ten. Figure 1 shows the 10 by 10 array of Pt wires that comprises the 100-element electrode for catalyst studies. A test cell can be configured to expose either an individual row or column. Candidate binary Pt-Ru catalysts were electroplated onto the structure in rows, with each row containing a different elemental ratio. By characterizing the materials in columns, 10 different alloys were evaluated simultaneously. A multi-channel potentiostat enabled individual electrochemical signatures to be simultaneously measured on each of the ten electrodes. A different environment (in this case pH) was evaluated for each column. After 10 electrodepositions and 10 electrochemical tests, 100 combinations

of composition and environment were evaluated – a 10X increase in efficiency over performing sequential electrodeposition and characterization runs. The metric for catalytic efficiency used in this study was the integrated charge for glucose oxidation (this takes into account both the power density and catalyst lifetime). The dependence of efficiency on composition and environment pH for a 0.3M glucose solution is shown in Figure 2. From these studies an optimal catalyst system was identified of 55:45 Pt:Ru in pH 8 glucose solution. This result was in turn used to identify starting conditions for developing a ternary Pt-Ru-Pb catalyst.

Significance: This study has lead to the successful development and application of a combinatorial technique for electrochemically screening material/environment combinations. The immediate benefit of this work is an increase in efficiency for identifying potential catalysts in the bio-micro fuel cell project. The greater and more far-reaching impact of this work is the establishment of a generic high-throughput characterization technique. The potential applications include screening other catalyst systems (for fuel cells, batteries, electrolyzers, etc.) and identifying other unique environment-electrode interactions that may find applications in sensing technologies.

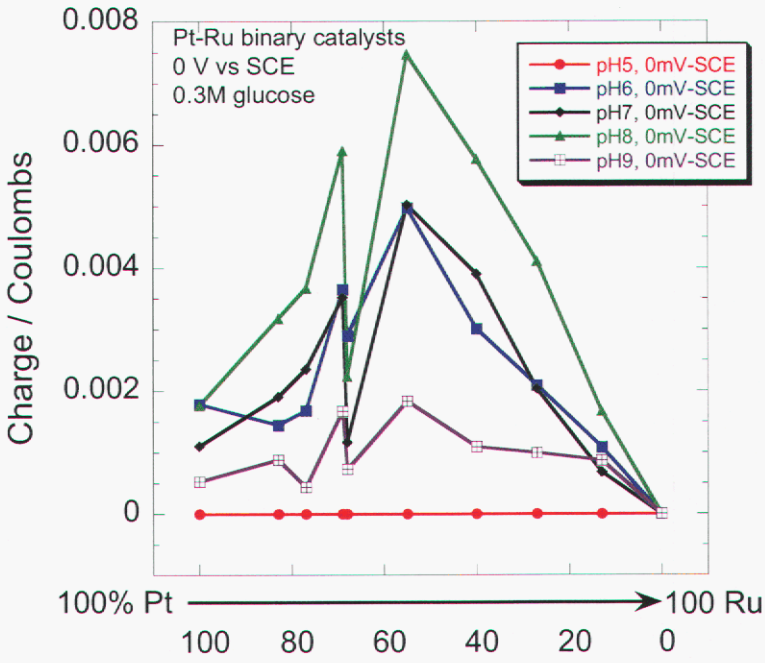

Figure 2. Data from combinatorial experiment.

Contact: Doug Wall, Corrosion & Electrochemical Sciences Dept.
Phone: (505) 844-6904
Fax: (505) 844-7910
Email: fdwall@sandia.gov

Computational Science of Solutes

K. Janssens, E. Holm, S. Foiles

Motivation: In many technical materials the evolution of the microstructure, either at the moment of manufacturing or during its lifetime in a component, is influence by the presence of solutes. Whether the solute atoms are intentionally introduced into the material or not, their presence has a direct effect on the grain boundary mobility and energy, which in turn are important factors in the kinetics of grain growth. In this study, we develop a combined model for the grain growth process in the presence of diffusing solute atoms. In addition, ab initio molecular dynamics are applied to gain a more quantitative insight in the effects of solute atoms on the grain boundary energy—the driving force for grain growth.

Accomplishment: Curvature driven migration of grain boundaries is a process in which a polycrystalline material minimizes its free energy by reducing the grain boundary surface area per unit volume. Neighboring grains typically have different crystallographic orientations. Depending on the orientation difference, a grain boundary will differ more or less from the ideal crystal structure hence have a different energy. Solute atoms will locally modify the crystallographic structure of the grain boundary, thus altering its energy. Although this concept is today common knowledge, quantitatively computing this segregation energy has proven much more difficult.

In this project, we implement ab initio density functional based calculations of the interaction of Mn impurities with critical defects. An example structure for a S5{310} grain boundary is shown in Figure 1. The magnitude of the interaction varies strongly between different boundaries. The interaction with the twin boundary is weak, 0.05 eV. For the S5{310} boundary, a very strong segregation energy of 0.48 eV was computed. These results indicate that the degree of interaction of Mn with boundaries will depend strongly on the character of the boundary. Thus, experiments may show no segregation (as observed in the single case studied to date) or considerable segregation, depending on the boundary examined. Also, this variation indicates that solutes will impact the stability and mobility of different types of boundaries in quite different ways.

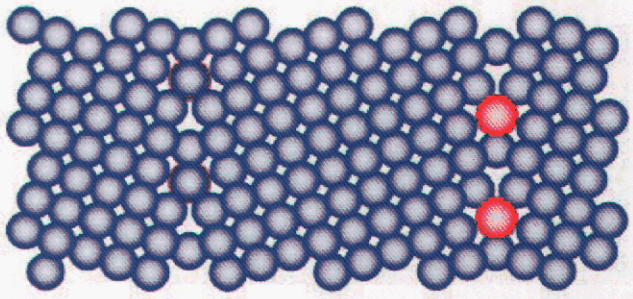

Figure 1. An example structure for solute atoms at a S5{310} grain boundary, used to compute density functional theory based estimates of the solute-grain boundary interaction energy.

In a second branch of this project, we are developing a computational, mesoscale model allowing the coupled simulation of grain growth, solute diffusion and the interaction between solutes and grain boundary motion. The grain growth process is

simulated using a recently developed approach: an irregular, shapeless cellular automaton model, which allows taking into account local variations of grain boundary mobility and energy. As most interest lies in the simulation of large collections of grains—to obtain statistically relevant information on the microstructure evolution—an MPI-based massive parallel code is under construction. A typical result for a small size problem run on a single processor machine is shown in Figure 2.

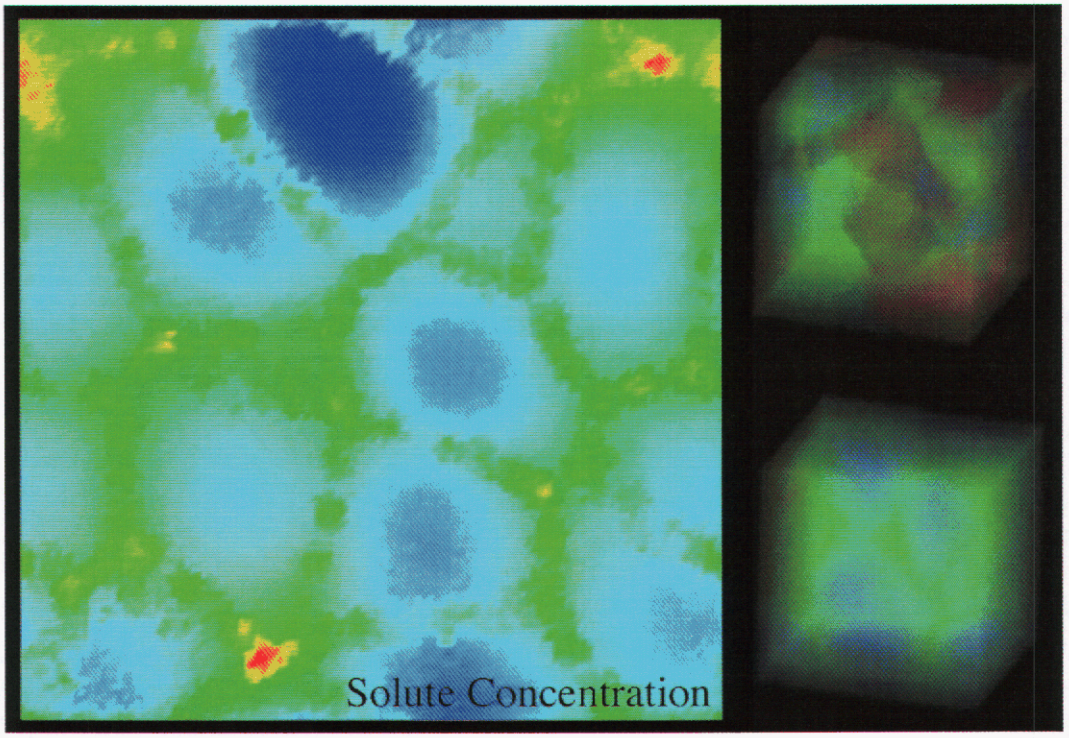

Figure 2. Solute concentration in a polycrystalline material during grain growth, as simulated using an irregular, shapeless cellular automaton.

Significance: This study is the first to present quantitative data on grain boundary energy in the presence of solute atoms. This information is essential if the cellular automaton is to successfully predict the grain growth process for non-ideal materials of technical importance.

Contact: Koenraad G. F. Janssens,
Computational Materials & Molecular Sciences Dept.
Phone: (505) 844-6678
Fax: (505) 844-9781
Email: kgjanss@sandia.gov

Corrosion Behavior and Electrical Contact Resistance of LIGA Electrical Contact Spring

L.M. Serna

Motivation: LIGA technology allows for the fabrication of structural metal electrodeposits with feature definition superior to that achieved by other micro-machining technologies (e.g. wire EDM). The high precision tolerances characteristic of LIGA make these parts desirable over existing conventional designs. Thus, LIGA may play an increasingly important role in new component designs for high-reliability applications (e.g. weapon surety). As one example, a LIGA contact spring has been designed to replace a conventional spring in a specific electro-mechanical application. The conventional spring is made of a gold-based alloy, whereas the Ni-based LIGA part must be gold-plated to enhance its electrical contact properties.

Corrosion resistance and electrical contact resistance are critical properties relevant to sliding contact electrical applications. Although wrought Ni is a fairly stable material (atmospheric corrosion rate is typically microns/year), the corrosion behavior of electrodeposited LIGA Ni-Mn materials have yet to be fully characterized. As an additional risk factor, due to the miniature sizes of MEMs devices, even the initiation of corrosion and minute amounts of corrosion products may adversely impact device performance. In an ongoing study, the atmospheric corrosion (i.e. aging) behavior and its effect on the electrical contact resistance of bare LIGA Ni-Mn is being examined.

Accomplishment: State-of-the-art techniques were used to conduct atmospheric exposures and measure the electrical contact resistance of LIGA parts. For this study, aggressive conditions were selected to simulate a compromised service environment (i.e. non-hermetic with halide contamination). The exposure environment was comprised of 78% N_2, 21% O_2, 30% RH and 10 ppb Cl_2 (g). Additional acceleration factors include increased temperature (30°C) and the use of a constantly replenished (rather than finite) gaseous source of contamination. Exposure to the test environment results in localized (pitting) corrosion for both bare LIGA Ni-Mn and wrought Ni 201, with a slightly higher density of pits on the LIGA material (Figure 1).

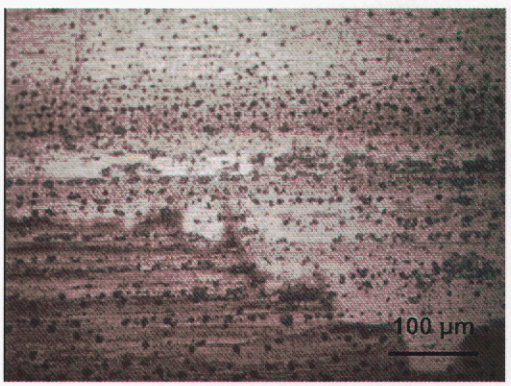

(a)

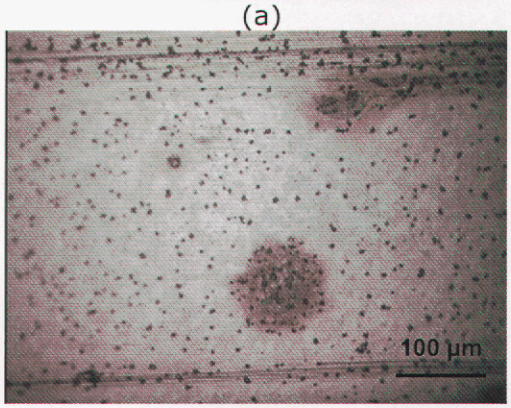

(b)

Figure 1. Pitting on (a) LIGA Ni-Mn and (b) wrought Ni 201 after 6 weeks exposure to 78% N_2, 21% O_2, 30% RH, 10 ppb Cl_2 at 30°C.

Unlike wrought Ni in which pitting is random, LIGA Ni-Mn exhibits a pattern of pits (rows perpendicular to the plating direction) that is potentially related to differences in composition arising from local plating conditions. The SEM/BSE images (Figure 2) more clearly show the pitting pattern as well as the cracked mud-cake appearance of the corrosion products which were identified by EDS as NiCl. Future experiments will focus on using solid phase contamination at levels relevant to service environments and correlating local alloy composition to pitting behavior. As a component intended to complete an electrical circuit, the LIGA spring is required to maintain low contact resistance. The findings of this work show that corrosion products on bare LIGA Ni-Mn result in a significant increase in contact resistance despite wiping contact. By comparison, corrosion product build-up on gold-plated LIGA Ni-Mn has no apparent effect on contact resistance.

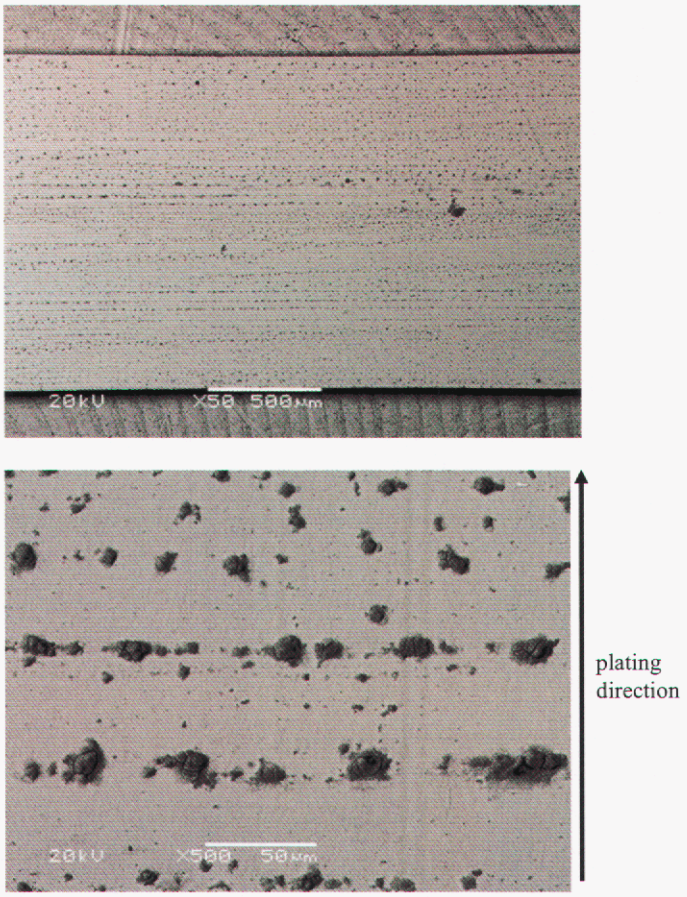

Figure 2. SEM / BE image showing atmospheric corrosion induced pitting and corrosion product morphology on LIGA Ni-Mn

Significance: These studies show that the atmospheric corrosion behavior of LIGA Ni-Mn is significantly different than conventional Ni, and is likely related to layered compositional differences in the small electrodeposits. Our findings highlight the need to better understand the relationship between processing conditions and corrosion behavior of LIGA materials. Finally, the effects of corrosion can be mitigated by the gold-plating or avoided by environmental control.

Contact: Lysle Serna, Corrosion & Electrochemical Sciences Dept.
Phone: (505) 284-4495
Fax: (505) 844-7910
Email: lmserna@sandia.gov

Corrosion Modeling of Digital Microelectronic Devices

N. R. Sorensen, J. Braithwaite

Motivation: Atmospheric corrosion of the metallic features in microelectronic devices is a degradation mode that often must be considered when assessing the reliability of electrical circuits. Corrosion of the prime susceptible material, aluminum, requires two conditions: the presence of moisture, and a halide contaminant (typically chloride ion) that cause localized breakdown of the oxide film. Because of availability and cost, plastic-encapsulated microelectronic (PEM) devices are now being used in place of ceramic hermetic packages (CHP) in high consequence military hardware. Contrary to CHP devices, the environment at the die surface of a PEM device may not remain dry over long periods of time due to the inherently high moisture permeability of the plastic encapsulant. In addition, because the devices are unpowered during long-term dormant storage, a typical drying event (ohmic heating during active use) does not occur. Thus, concern exists that corrosion may reduce the reliability of PEM devices.

Historically, two types of corrosion-related phenomena have been observed in field returns: Au wire/Al bondpad interfacial degradation and distributed Al track corrosion. Track corrosion typically correlates with moisture penetration through defects in the passivation layer (e.g. SiN). Bondpads have no passivation treatment and are susceptible to accelerated attack due to galvanic coupling with the Au wire.

Accomplishment: We are currently developing phenomenological-based corrosion models that will allow us to predict the effects of atmospheric corrosion on system or sub-system performance and reliability. An important aspect of the models is a link between materials changes predicted by the mathematical model and electrical function of the device. For example, an increase in resistance of 50% for a bleed resistor may have little effect on circuit performance, while the same increase in an op-amp circuit may result in failure. Therefore, we are making an attempt to couple materials degradation processes (e.g. corrosion) with electrical system models to help us determine how corrosion affects performance, and thus, reliability.

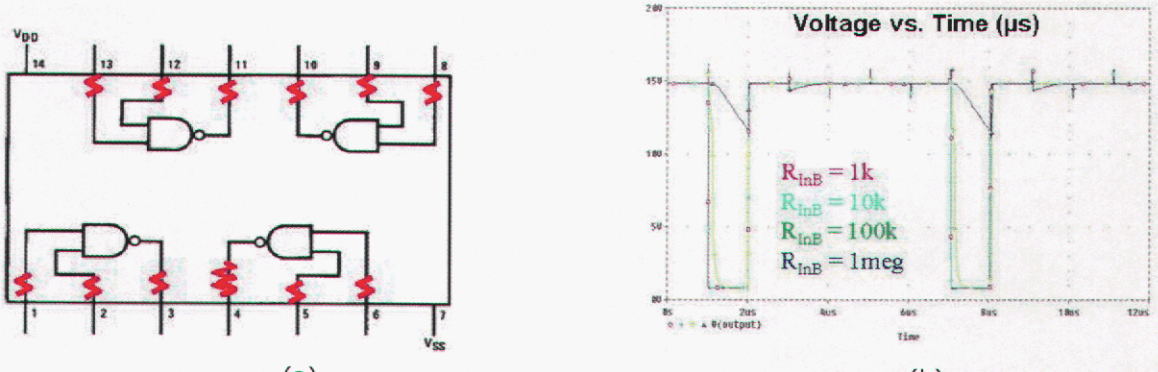

(a) (b)

Figure 1. PSPICE simulations for a CD4011 device. The schematic for the CD4011 along with resistors that simulate bondpad corrosion are shown in (a), with the PSPICE simulations for different values of resistance at one of the input bondpads shown in (b).

Figure 1 shows the results of simulating the effects of bondpad corrosion in a CD4011 (dual input quad nand gate). The device layout and the resistors representing corrosion at the bondpads (in red) are shown in (a). Results of PSPICE simulations, an electrical circuit emulator, are presented in (b). Corrosion of the Al bondpads is simulated by an increase in the values of the resistors. In this series of simulations, only the resistor associated with corrosion of one of the input bondpads was allowed to change. The shape of the output square wave changes with increasing resistance, eventually resulting in failure of the device when the output signal remains high. It is important to note that a very high value of resistance (~1MΩ) is required to significantly degrade device performance.

Figure 2 presents failure data for CD4011 with bondpads contaminated with NaCl and exposed to an elevated humidity environment. It appears that the quantity of contaminant has little effect on the minimum time to failure, but significantly affects the distribution of time to failure. The photomicrograph in (b) shows bondpads that have been attacked during exposure. No Al metallization is visible in the regions of the bondpads, and corrosion products can be seen on the die surface.

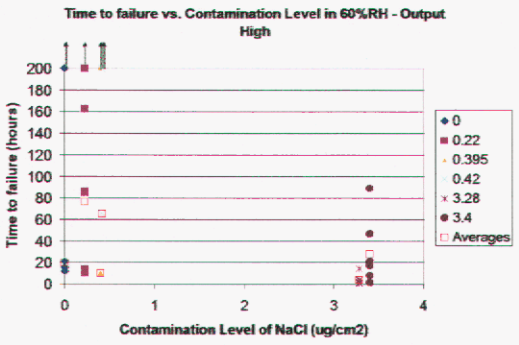

(a)

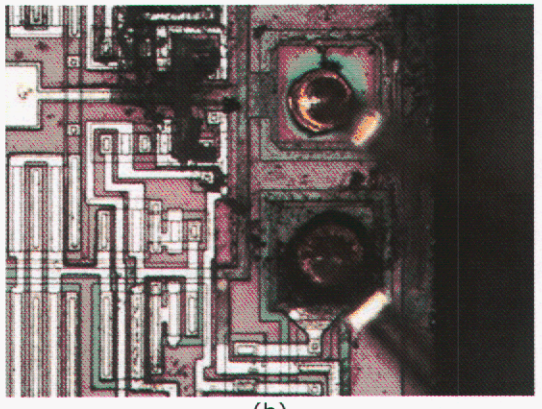

(b)

Figure 2. Failure data for CD4011 devices contaminated with NaCl and exposed to humidity and temperature. The photomicrograph on the right shows Al bondpads that have been consumed during exposure, resulting in open circuits between the bondwire and the die.

Significance: This is the first time that we have been able to make a direct tie between corrosion and the electrical system model. Experimental results confirm that the electrical model is providing the correct form for device failure. These results also demonstrate the robustness of digital circuits, and suggest that analog devices such as op amps may be more susceptible to atmospheric corrosion-induced degradation.

Contact: Rob Sorensen, Corrosion & Electrochemical Sciences Dept.
Phone: (505) 844-5558
Fax: (505) 844-5558
Email: nrsoren@sandia.gov

Effect of Copper Sulfidation on Connector Performance

D. Enos, H. Moffat, A. Sun

Motivation: Electronic connectors are typically constructed of a copper alloy with a protective noble metal electroplate (typically gold). Atmospheric corrosion of these connectors in sulfur containing environments results in sulfidation of the underlying copper through defects in the noble metal layer. Figure 1 illustrates the type of localized damage typically observed (indicated by arrow). The impact of this corrosion product layer is an increase in the resistance of electrical contacts which can lead to failure or malfunction of a device. As such, there is a critical need for a means to predict the extent of this degradation as a function of the exposure environment, the physical properties of the connector itself, and time. Meeting this need requires both a detailed understanding of the degradation mechanisms, as well as the formulation of a model which accurately captures this phenomenon. The primary goal of this task is to characterize the degradation mechanisms of gold plated copper as used in microelectronic connectors, along with the construction of an appropriate mathematical model. To achieve this, a number of objectives be met – first, the validity of any assumptions/simplifications required by the model must be proven. Second, a detailed understanding of the kinetics of the sulfidation process must be obtained. Finally, calibration data describing the overall atmospheric corrosion process (macroscopic and microscopic effects) must be provided such that the model can effectively predict the behavior of actual devices.

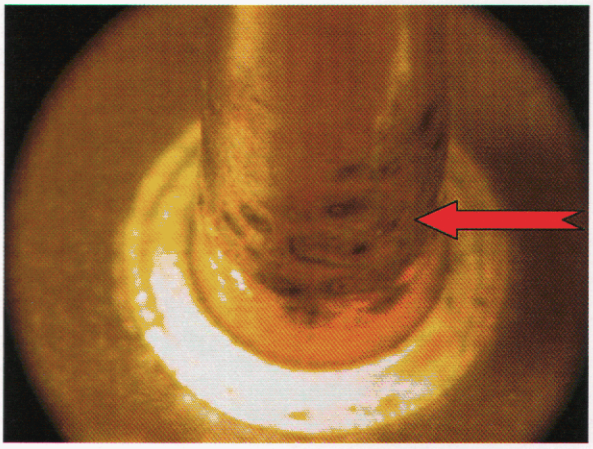

Figure 1: Connector pin which has undergone atmospheric sulfidation.

Accomplishment: A mathematical model has been formulated which integrates local phenomena (i.e., sulfidation at a defect site) and the functional mechanics of an electrical connector (contact area and force, substrate roughness, wipe, etc.). To facilitate the mathematical simulation, certain simplifications to the assumed composition of the exposure environment were made. As a result, it was essential that the impact of these simplifications on the extent and nature of the observed atmospheric corrosion be quantified in terms of material characteristics of importance to the model (i.e., rate of attack, electrical properties of the corroded surface, etc.) Atmospheric corrosion tests were performed on nominally identical gold plated copper samples within a gas exposure system (see Figure 2). All samples were exposed both to a Battelle Class 2 environment (an accelerated environment containing H_2S, Cl_2, and NO_2 used extensively to simulate a light industrial environment) as well as the simplified environment (in which Cl_2 and NO_2 were omitted).

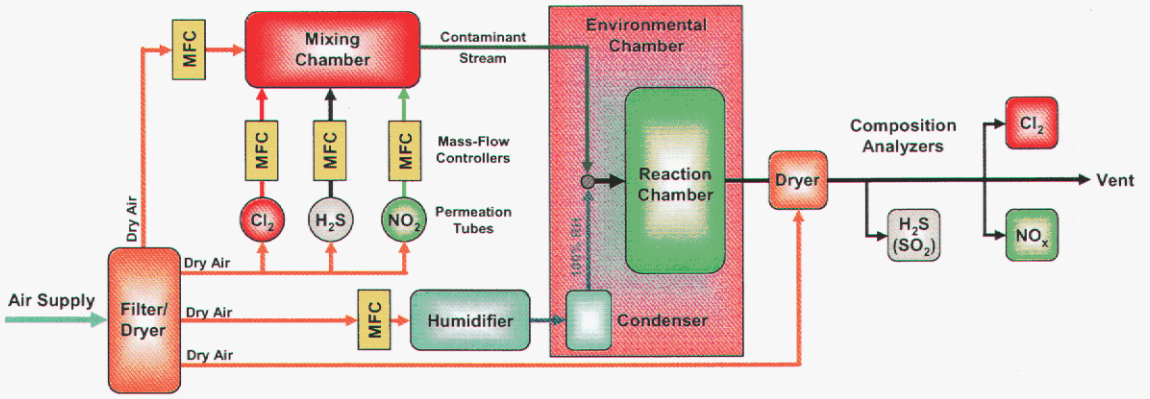

Figure 2: Mixed-flowing-gas exposure system.

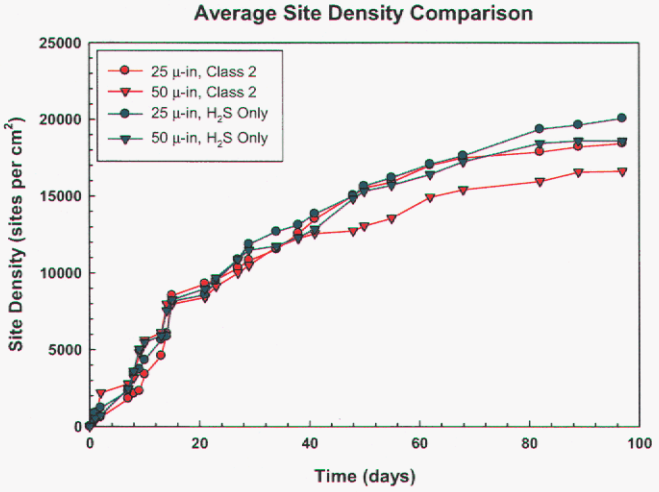

Figure 3: Number density of corrosion sites as a function of exposure environment.

The number density of corrosion sites (Figure 3), the growth rate of copper sulfide from a bare copper surface, and the electrical (i.e., resistance) properties of the resulting corrosion product were found to be equivalent for the two environments over relevant time scales. As such, this experimentation demonstrated that the simplified environment resulted in similar corrosion behavior in terms of the properties relevant to the model, and could be used to as calibration data to effectively model the impact of atmospheric corrosion on gold plated copper components. Furthermore, this result confirms that the wealth of historic data taken under Battelle Class 2 exposure conditions can be used for validation of the model.

Significance: A model has been formulated which based upon an experimentally derived understanding of the relevant degradation processes will allow the long term reliability of an electrical connector to be assessed as a function of its materials of construction and the exposure environment. While the model makes some simplifying assumptions to the exposure environment, it has been experimentally verified that these simplifications do not alter the electrical properties of the resulting corrosion product when compared to that from exposure to the Battelle Class 2 environment. As such, both new and historically obtained data can be used for model validation.

Contact: David G. Enos, Corrosion & Electrochemical Sciences Dept.
Phone: (505) 844-2701
Fax: (505) 844-7910
Email: dgenos@sandia.gov

Solder Interconnect Predictor (SIP) Software for Assessing Fatigue in Electronic Solder Joints

P. Vianco, M. Neilsen, T. Clifford, S. Burchett

Motivation: The long-term reliability of military, space, and high-consequence electronics requires that the solder interconnections be able to provide electrical and mechanical functions over the service life of the system.

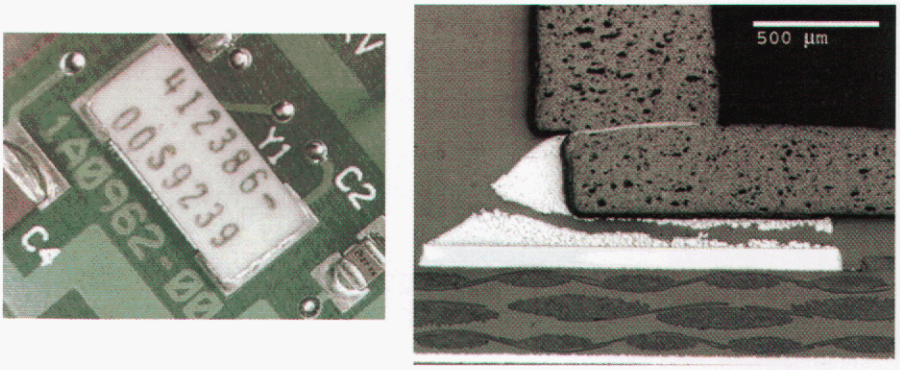

Figure 1. Fatigue degradation in a 63Sn-37Pb surface-mount component solder joint.

Increased functionality and further miniaturization have placed a greater emphasis on the need for level 2 interconnections (package-to-circuit board) to meet more stringent reliability requirements. Moreover, because new package designs and materials are being created at a rapid pace, the development of empirical reliability databases for predicting solder joint fatigue failures (Fig. 1), is quickly becoming impractical. Therefore, computational models/software that predict solder-joint fatigue will become critical for the fielding of future, high-reliability electronics assemblies.

A new modeling approach was needed to improve upon both the flexibility and fidelity of solder joint fatigue predictions in order to accommodate new electronic packages, materials, and use conditions. Moreover, the new model has to be accessible to *novice* design and process engineers who are tasked with the development and manufacturing, respectively, of electronic systems and sub-systems. This capability should provide a higher level of confidence that electronics hardware will meet mission reliability requirements without the need for excessive safety factors that increase costs and/or exclude critical packaging technologies (designs and materials) that could enhance system functionality. A partnership was established with Lockheed Martin, Missiles and Space Organization, the objective of which was to develop a software package for the design or process engineer that predicts solder fatigue degradation in second-level 63Sn-37Pb (wt.%, Sn-Pb) solder interconnections.

Accomplishment: The COMPSiR© constitutive model was developed at Sandia to predict fatigue degradation in 63Sn-37Pb solder interconnections. The constitutive equation uses a microstructure feedback state-variable – namely, the Pb-rich phase particle size – to incorporate real-time changes to the solder mechanical properties (yield strength, creep resistance, etc.) resulting from the evolution of the microstructure – the so-called "microstructure-properties relationship." A finite

element mesh locates the fatigue deformation at each (x, y, z) location within the geometry of the solder joint. The COMPSiR© numerical code was streamlined in order to minimize the computational time required to execute a solder-joint analysis. Then, the Sandia-Lockheed partnership was expanded to include Strikewire Technologies, LLC to incorporate appropriate graphical user interfaces (GUIs) at the front and back ends of the COMPSiR© model. The GUIs expedited data input by the user, as well as facilitated the interpretation of the model output at the close of the computation. In addition, an interactive library of material properties and solder-joint geometries was added to the model input. Examples of the geometries included leadless chip devices, leaded flat package, and complex area array interconnections. This addition allows for the analysis of a variety of electronic package configurations. The resulting software was named Solder Interconnect Predictor (SIP). Concurrently, an extensive test program was put into place at Lockheed Martin Missiles and Space Organization to develop the experimental data needed to validate the SIP predictions. The SIP software continues to undergo extensive testing at several Lockheed Martin locations.

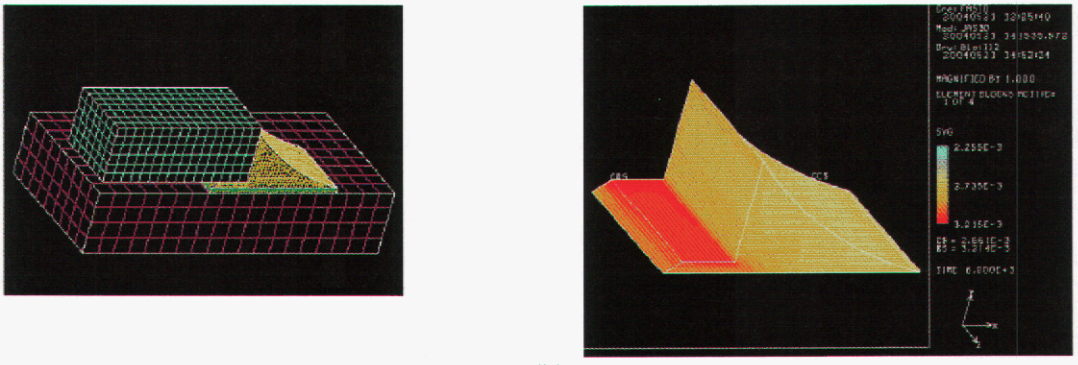

(a) (b)

Figure 2. SIP software output showing the degree of fatigue degradation in a Sn-Pb solder interconnection.

Significance: The SIP software will significantly improve the fidelity of solder joint fatigue predictions, which in turn, will allow engineers to design-for-reliability more effectively at the early stages of a project. Also, there will be a significant reduction in the need for accelerated aging tests, thereby lowering the cost and time resources invested in the development of much-needed reliability databases. Besides the computational successes that were represented by the adaptation of the highly-complex COMPSiR© model to the level of a desktop computer, was creation of a methodology whereby Sandia modelers were integrated with commercial software developers in order to put complex computational tools into the hands of scientist and design engineers for their wider application.

Contact: Paul T. Vianco, Materials Reliability Dept.
Phone: (505) 844-3429
Fax: (505) 844-4816
Email: ptvianc@sandia.gov

Foundations of the Nonlinear Viscoelasticity of Polymers

D. Adolf, J. Budzien, J. McCoy

Motivation: We previously developed a nonlinear viscoelastic theory for polymers (Adolf, Chambers, and Caruthers) that quantitatively predicts a wide range of response including creep, yield, physical aging, volume recovery, and enthalpy relaxation (Fig. 1). Not only is ours is the first and only approach capable of such broad, quantitative predictions, each model input represents a physically significant, easily measured quantity. That is, the model incorporates no free fitting parameters. Not only has this model allowed us to calculate stresses in encapsulated components more accurately but has proven to be an enabling technology for quantitative prediction of the initiation of cohesive and adhesive failure in polymers.

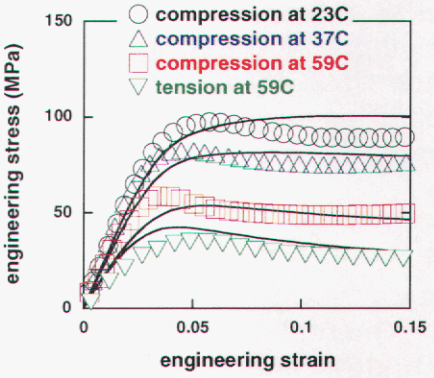

(a)

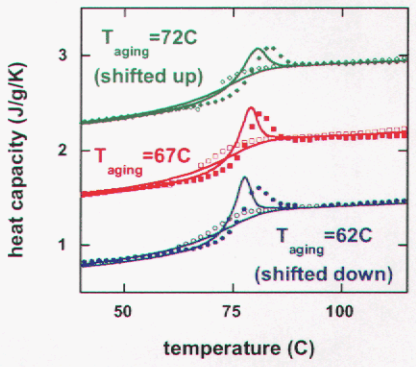

(b)

Figure 1. Examples of quantitative predictions made by the nonlinear viscoelastic theory (symbols=data, lines=predictions) for an epoxy: (a) mechanical yield and (b) enthalpy relaxation.

The basic assumption of this approach states that the relaxation rates of polymers depend on the potential energy of the system. While this assumption produces a formalism that yields quantitative predictions, it nevertheless was assumed without validation. Our current research focused on proving this assumption using molecular dynamics simulations of chain molecules. While it is often difficult to connect molecular simulations directly to macroscopic response, our particular problem is an exception. It is rather straightforward to calculate both polymer mobility and potential energy within molecular simulations. The connection to macroscopic response lies in the nonlinear viscoelastic theory that specifically relates these two quantities.

Accomplishment: Systems of 80 ten-monomer chains interacting with Lennard-Jones (L-J) potentials were simulated at numerous pressures, P, densities, ρ, and temperatures, T. The polymer mobility, ζ, was determined by the center-of-mass diffusivity of the chains, D, divided by temperature: that is, $\zeta = D/T$, as usual. The raw data are plotted in Fig. 2a. It is apparent that mobility is not a function of temperature alone. The non-bonded potential energy of the system is readily available by summing the L-J interactions. The mobilities in Fig. 2a are re-plotted in Fig. 2b as a function of the system non-bonded potential energy density, E_{nb}, at

that particular equilibrated thermodynamic (P-ρ-T) state. A single master curve is produced for all simulations indicating that polymer mobility is a function of E_{nb}. The mobility apparently vanishes at a non-bonded potential energy density of roughly -6. Interestingly, this value of E_{nb} in these reduced units is very close to the minimum potential energy that can be realized by this system. This implies that the glass transition occurs near the point when the potential energy reaches its minimum.

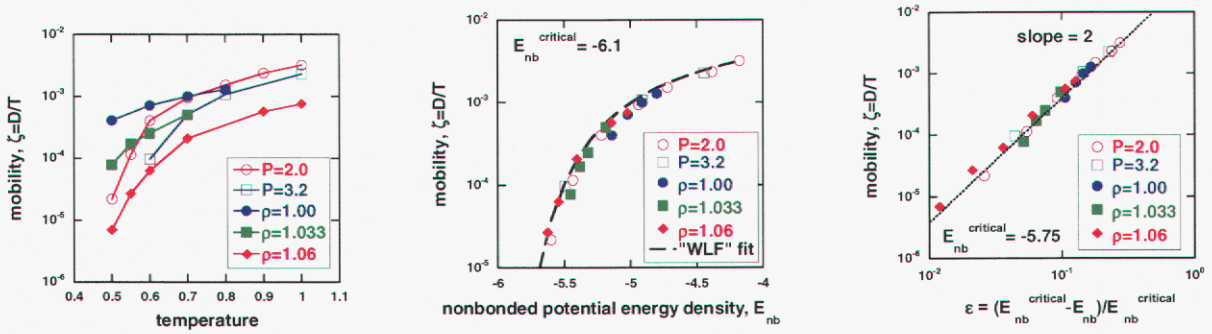

(a) (b) (c)

Figure 2. Mobilities of the polymer systems at different thermodynamic states plotted vs. (a) temperature, (b) potential energy density, and (c) the reduced potential energy as in critical phenomena.

The same data are re-plotted in yet another fashion in Fig. 2c. Here, the mobilities are plotted against the normalized difference between the current potential energy density and its minimum. This type of plot is typically used for analyzing critical phenomena. The fact that Fig. 2c exhibits power-law behavior with an exponent of roughly 2 (a reasonable value) suggests that the glass transition itself is a critical phenomena yet not a thermodynamic transition, since no calculated thermodynamic quantities show any divergence.

Significance: We have demonstrated it is not coincidental that our nonlinear viscoelastic theory can quantitatively predict glassy polymer response with physically-based model inputs. Molecular dynamics simulations prove that the foundation of this approach (relaxation rates depend on potential energy) accurately reflects the physics of polymers.

Contact: Douglas Adolf, Organic Materials Dept.
Phone: (505) 844-4773
Fax: (505) 844-9624
Email: dbadolf@sandia.gov

High-Sensitivity Chemical Derivatization NMR Analysis for Condition Monitoring of Aged Elastomers

R. Assink, J. Skutnik, M. Celina

Motivation: The development of accurate service lifetime prediction models for polymeric materials is crucial for high consequence applications. Lifetimes are often predicted by altering a critical environmental factor, such as temperature, to accelerate the aging of the material and monitoring changes in mechanical properties as a function of the aging time. An Arrhenius plot is then used to extrapolate the accelerated data to the operating range of the polymer. Although this technique is generally useful, deviation from linearity in the Arrhenius plot may exist when the data span a large temperature range, leading to difficult extrapolations and inaccurate lifetime predictions.

Chemical methods offer the potential for increased sensitivity and the possibility of measuring degradation rates under ambient conditions so that extrapolations are not required. In this study, we utilize an anhydride-alcohol esterification reaction to label all alcohols present and track the formation of alcohol functionalities during the course of thermo-oxidative aging of a hydroxy terminated polybutadiene (HTPB) elastomer. We have previously shown that 60 mole % of the oxygen involved in the oxidation process are converted to alcohols. Trifluoroacetic anhydride (TFAA) is reacted with HTPB to convert the alcohol groups in HTPB into trifluorinated esters. The intensity of the ^{19}F NMR signal from the trifluorinated esters is then used to determine the concentration of alcohol groups present in the polymer. ^{19}F is an ideal NMR nucleus, with an absolute intensity 4,700 times that of natural abundance ^{13}C and offers the possibility of measuring very low degradation rates of polymers.

Accomplishment: Organic reagents containing various functional groups were reacted with TFAA to determine the 19F chemical shifts of the resultant products. Functional groups investigated reflect several possible functionalities in the polymer such as (a) normal oxidation products, including 1°, 2° and 3° alcohols and hydroperoxides, (b) important cross-linking agents containing isocyanate derivatives, amines and urethanes to represent possible functionalities produced during the HTPB curing process, and (c) groups with known anti-oxidant properties, such as hindered phenols. Relatively narrow resonances and reasonable chemical shift dispersion enabled these functionalities to be assigned. TFAA was also reacted with differing amounts of simple alcohol reagents, in quantities as small as 1 µmol, to establish the detection limits. Figure 1 shows that the ^{19}F

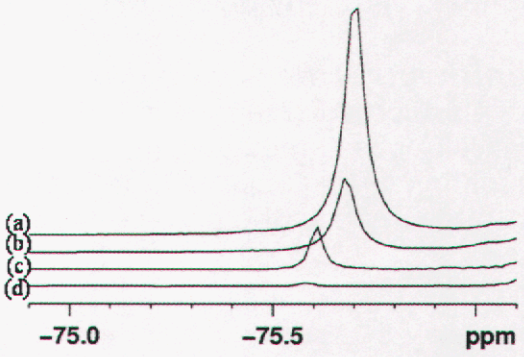

Figure 1. The ^{19}F NMR spectra of ester resulting from reaction of (a) 100, (b) 30, (c) 10 and (d) 1 µmol of 1-butanol with TFAA.

resonance from even the lowest level of alcohol, corresponding to less than 0.2% oxidation, can be detected after 4 scans requiring less than 30 seconds of instrument time. Finally, TFAA was reacted with HTPB samples that had been thermally aged for varying periods of time to determine the extent of oxidation of the material. Figure 2 shows a comparison between the ^{19}F NMR results and oxidative aging data obtained by conventional oxygen consumption methods. The nonzero intercept of the ^{19}F results reflects initial reactive groups in the elastomer. The rates of oxidation, represented by the slopes of the two lines, are comparable.

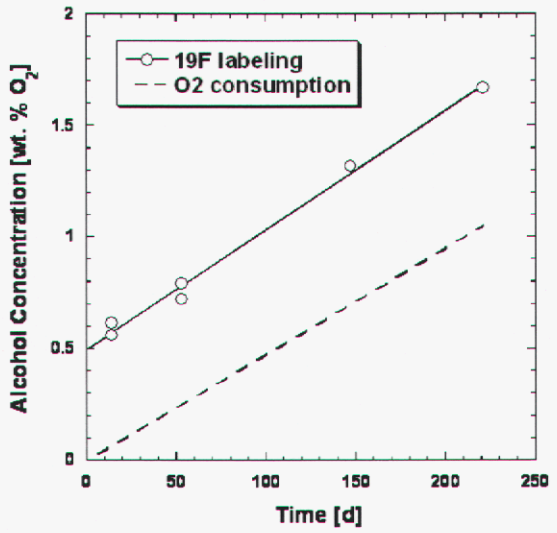

Figure 2. Increase in oxidation level of HTPB with aging time at 80°C measured by ^{19}F labeling and oxygen consumption methods.

Significance: This research has established a very sensitive method that is useful for investigating both the chemistry of polymer aging and detecting low levels of oxidation in field samples. The 19F NMR technique has the advantage that analyses may be conducted quickly and performed on actual field samples. Investigations of the reactions of TFAA with other functional groups in HTPB may provide additional information on the chemistry of both the curing and aging processes.

Contact: Roger Assink, Organic Materials Dept.
Phone: (505) 844-6372
Fax: (505) 844-9781
Email: raassin@sandia.gov

Modeling Hydrolysis in Organosilane Films

M. Kent, H. Yim, D. Tallant, M. Garcia

Motivation: Organosilanes have achieved widespread use as adhesion promoters in composite materials. They have the general structure $X_mSi(CH_2)_nY$, where m is typically 3 and n = 0 – 3. X is a group that can be hydrolyzed, typically ethoxy or methoxy and Y is an organofunctional group chosen to react with a given organic material. Once hydrolyzed, the silanetriol is effectively a trifunctional monomer that can polymerize with itself via condensation or can react with an inorganic substrate. Such coupling agents are often deposited as thin films of a few hundred angstroms. The distribution of crosslinks within such films can vary depending upon the nature of the organofunctional group Y and the extent of hydrolysis, and affects their ability to interpenetrate with resins, their ability to transfer stress, and their hydrolytic stability.

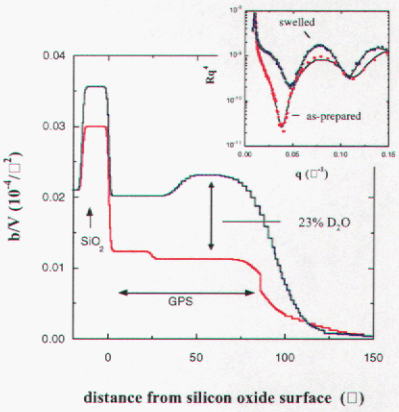

Figure 1. Neutron reflectivity for a ~100 Å film of GPS as-prepared and after swelling with D2O vapors.

Hydrolysis of the siloxane (Si-O-Si) network bonds or Si-O-M bonds to the substrate, where M is the metal substrate atom, is believed to be the primary degradation mechanism when organosilane films are exposed to the environment. Despite the importance, a kinetic model of hydrolysis based on first principles has not yet been attained. Direct measurement of the rate of hydrolysis and the water content within ultrathin silane films pose the primary challenges. We have used neutron reflection to measure the local concentration of water and infrared (IR) spectroscopy in the attenuated total reflection mode to measure the rate of hydrolysis of Si-O-Si bonds. This allows a first order kinetic model to be formulated.

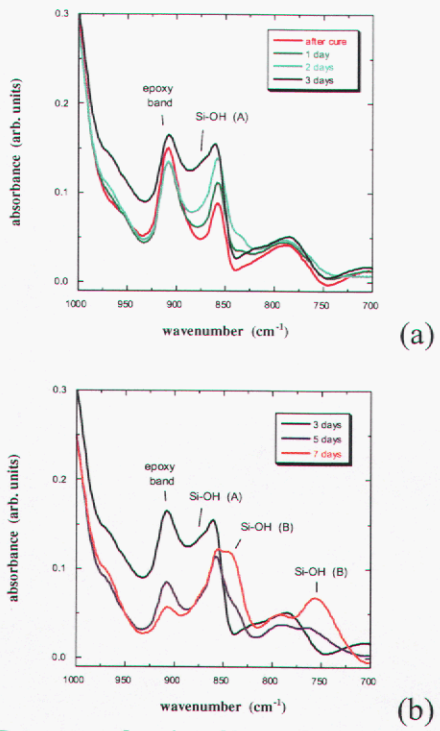

Figure 2. IR spectra for thin films of GPS on silicon coated germanium ATR plates as-prepared and after exposure to saturated H_2O vapors at 80°C for a) 0 to 3 days, and b) 3 to 7 days.

Materials Aging

Accomplishment: The local concentration of water within silane films was measured using neutron reflectivity (NR) at the LANSCE facility at Los Alamos National Laboratory. Ultrathin films of 3-glycidoxypropyltrimethoxy-silane (GPS) were spin-coated onto silicon wafers. NR was collected in the dry state and then after swelling with D_2O vapors. The reflectivity curves for each state are shown in Figure 1. Analysis of these data leads to the scattering length density (SLD) profiles also shown in Figure 1. The SLD is a function of the atomic composition and the density. The data indicate greater swelling in the bulk of the film than near the substrate surface. The difference in SLD in the bulk of the film corresponds to about 23% D_2O.

The rate of hydrolysis of Si-O-Si was measured using IR-ATR. Germanium ATR plates were used because of their low absorption in the wavenumber range of interest (700-1100 cm-1). The Ge plates were coated with 1000 Å of evaporated silicon to provide a silicon oxide surface. The IR spectrum was measured as-prepared and after exposure to saturated H_2O vapors at 80°C for various periods of time. The spectra are shown in Figure 2a and Figure 2b. The data show an increase in a band peaking around 870 cm^{-1} through three days of conditioning that we assign to vicinal Si-OH. Beyond 3 days of conditioning, the band at 870 cm^{-1} decreases and is replaced by bands at 840 and 750 cm^{-1}. We assign these bands to geminal Si-OH.

Finally, X-ray reflectivity has shown that structural degradation within the film roughly coincides with the appearance of the bands assigned to geminal Si-OH. A silicon wafer with a ~100 Å GPS film was first examined as-prepared. The sample was then exposed to saturated H_2O vapors at 80°C for a given period of time. Then the sample was dessicated overnight and examined by X-ray reflectivity. The data for various periods of conditioning are shown in Figure 3. A large change in the structure of the film is apparent between 4 and 7 days of conditioning, which corresponds roughly the time for appearance of the IR bands assigned to geminal Si-OH.

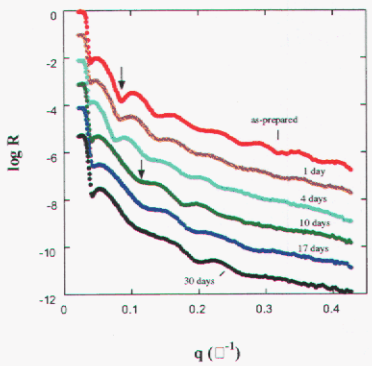

Figure 3. X-ray reflectivity data from a GPS sample as a function of conditioning time. The arrows highlight the shift observed beyond 4 days of conditioning.

Significance: These measurements provide a direct measurement of the rate of hydrolysis, the local concentration of water within the film, and a measurement of the extent of hydrolysis at which substantial structural degradation occurs. These are the necessary elements for establishing a kinetic model for the lifetime of such films.

Contact: Mike Kent, Biomolecular & Chemical Analysis Dept.
Phone: (505) 845-8178
Fax: (505) 844-9781
Email: mskent@sandia.gov

Structure and Mechanical Properties of Polymer Networks Near Surfaces: Effects of Humidity and Network Architecture

D. Heine, M. Stevens, A. Frischknecht

Motivation: Adhesive joining is used extensively in the assembly of many devices manufactured at Sandia. As a result, adhesive failure is a major degradation mode affecting the reliability of these devices. Although a detailed mechanism for adhesive failure is not known, the presence of water vapor in the atmosphere during the manufacture or storage of a device is one means of accelerating the degradation process. Understanding how humidity influences the interaction between the adhesive and the surface allows us to develop approaches to minimize the degradation of adhesives. Possibly the most practical approach to implement is to modify the chemical structure of the polymer adhesive itself. Understanding the relationship between the network architecture of the adhesive and the failure mechanism makes it possible to maximize their resistance to degradation.

Accomplishment: The diffusion of water in poly(dimethylsiloxane) (PDMS) melts and networks is being studied using molecular dynamics (MD) simulation. Fully atomistic potentials are required to capture the important hydrogen bonding interactions of the water molecules as well as the orientations of water and polymer molecules near surfaces. Our simulations demonstrate the formation of water clusters (Figure 1) for all but minimal concentrations of water inside the PDMS. The formation of these clusters drastically reduces the rate of water diffusion through the polymer. Free water molecules and small clusters diffuse via a hopping motion where temporary channels of free space form in the polymer allowing the water molecules to transit from one "cage" to another. The calculated bulk diffusion rate of 1.72×10^5 cm^2/s is in good agreement with the experimental value of 1.45×10^5 cm^2/s. In the presence of a silicon dioxide substrate, the water molecules also aggregate on the substrate resulting in a reduced surface density of PDMS and thus a less effective adhesive.

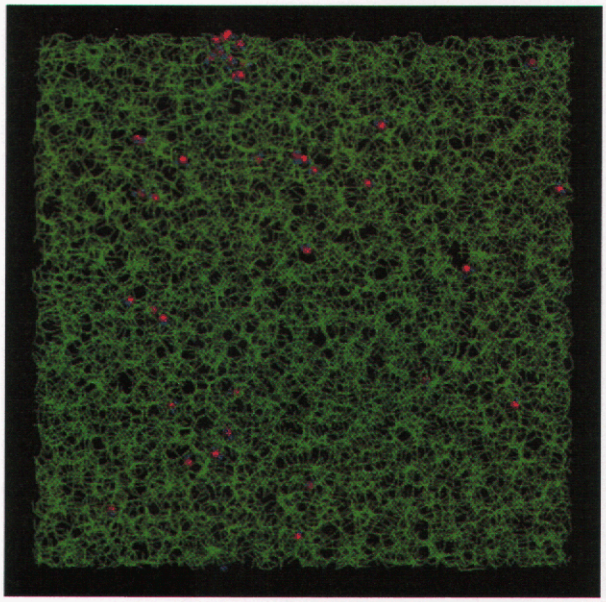

Figure 1. Water molecules forming clusters in a PDMS melt.

The effects of mixed functionality and degree of curing on the stress-strain behavior of highly cross-linked polymer networks are also being studied by MD (Figure 2).

The networks are made dynamically in a manner similar to epoxy network formation, and

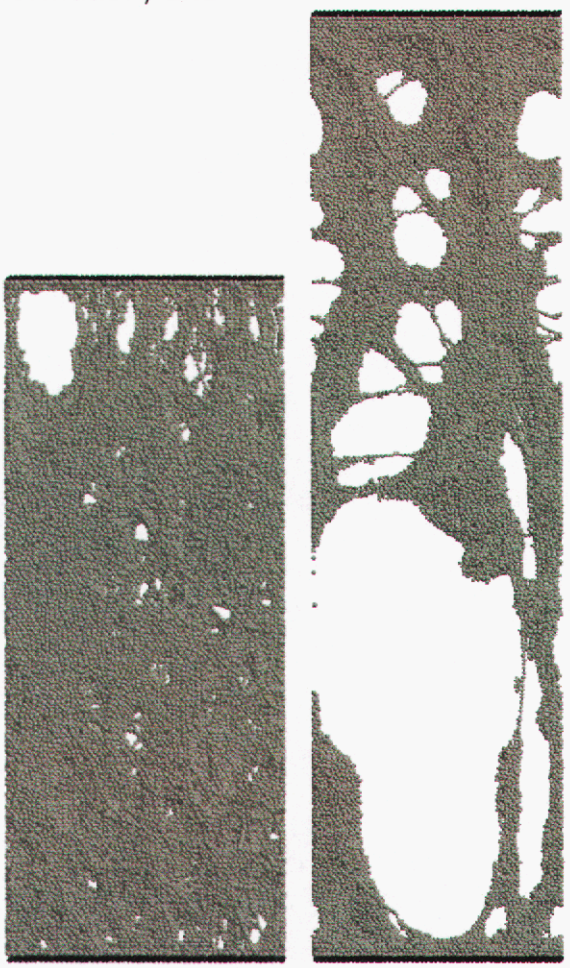

Figure 2. Images before failure for f = 3 at full cure cross-linking 75% cure.

the average functionality of the cross-linker, f_{av}, is systematically varied from 3 to 6 by mixing cross-linkers with functionalities f = 3, 4, and 6. Stress-strain curves are determined for each system from tensile pull simulations. The range of strain of the plateau region (R_P) in the stress-strain curve, failure strain (ε_f), and failure stress (ε_f) for fully cured networks are found to have a power law dependence on f_{av} as $\sim f_{av}^{\alpha}$. For R_P and ε_f, α is determined to be -1.22(3) and -1.26(4), respectively. The failure strain is equal to the strain needed to make taut the maximum of the minimal paths through the network connecting the two solid surfaces. The failure stress, however, shows two distinct regions. For $f_{av} \geq 4$, σ_f increases with increase in f_{av} and α = 1.22(5). In this f_{av} regime, the work to failure is constant. For $f_{av} \leq 4$, the systems fail interfacially, σ_f becomes a constant, and work to failure decreases with f_{av}. These mechanical properties are also found to depend on the degree of curing. With decrease in percentage of curing, failure stress decreases and failure strain increases. The mode of failure changes from interfacial to bulk.

Significance: Insight into the critical factors of water diffusion in PDMS is leading to the study of modified polymer structures, such as changes in end groups and crosslinker functionality, to minimize the aggregation of water at the substrate and to delay the onset of adhesive failure.

Contact: David Heine, Computational Materials & Molecular Sciences Dept.
Phone: (505) 284-9516
Fax: (505) 844-9781
Email: drheine@sandia.gov

An Ion Mobility Spectrometer Mass Spectrometer for Trace Detection & Identification of Controlled Substances

D. Austin, D. Hunka, J. Hunter, E. Varley

Motivation: Ion mobility spectrometry (IMS) is a highly sensitive method for separating and detecting trace components from a complex mixture. Sandia has developed several IMS instruments for such applications as explosive detection at airports and chemical agent detection on the battlefield. Although these instruments exhibit high sensitivity to target molecules, the complex chemical environments of these locations produce numerous interferences, resulting in a high level of false positives and unidentifiable spectral peaks. In order to improve the reliability and selectivity of Sandia's IMS systems, we have been modifying a triple quadrupole mass spectrometer to readily interface with various IMS systems and provide positive chemical identification of the species detected by the IMS. The ideal interface will allow sufficient ion transmission into the mass spectrometer, reduce or prevent ion clustering, and allow the mass spectrometer to operate at high vacuum while the IMS operates at atmospheric pressure. In addition, an ideal interface would be capable of rapid and simple connection to any of Sandia's IMS systems, without disruption of either the ion focusing properties of the interface or the pressure of the mass spectrometer.

Accomplishment: Efforts during the second year of this project (FY 2004) included developing PC-based control of the mass spectrometer, designing a shutter to allow vacuum to be preserved in the mass spectrometer when the ion mobility spectrometer is not in use, and designing a detection scheme to allow simultaneous ion detection at the ends of both the mobility and mass spectrometers.

The API-3 mass spectrometer purchased for this project currently runs on a Mac OS 7 system, while the ion mobility spectrometers used at Sandia all operate using PC-based systems. Due to strict millisecond synchronization and data-sharing requirements, these two systems cannot be combined in a simple way. Previous commercial and academic efforts to develop a PC-based control system for the API-3 have not succeeded. We have investigated the possibility of using LabVIEW programming architecture to create a control system that would be used for both systems. After thoroughly reviewing both the software and hardware in the current system, and after discussing options with the original source code author at Sciex, we have determined that it is not appropriate to further pursue this option. We are currently looking at other options to synchronize both instruments in their respective native software environments.

The interface between the mobility region at atmospheric pressure and the mass spectrometer at high vacuum involves a small aperture. Leaving this aperture open continuously would quickly saturate the cryogenic pumps and compromise high vacuum. At the same time, there is very little room for a physical shutter immediately in front of the aperture. We have built and tested a small shutter in

which a Teflon membrane is suspended between steel pieces in such a way that the membrane can close the aperture without disrupting any other system components. The entire shutter mechanism is less than 0.04" thick at its widest point, making it possible to be inserted between the final mobility ring and the faraday detector. A rotation manipulator allows the shutter to be moved completely outside of the ion mobility rings during operation.

In order to allow simultaneous measurement of the mobility spectrum and each peak's mass spectrum, we are using the entrance plate of the mass spectrometer as the faraday detector of the IMS. A small region of this plate is electrically isolated and floated to facilitate ion injection into the MS, while at the same time electronics allow the IMS signal to be acquired on this floated plate.

Significance: The design of the interface is such that any of Sandia's IMS systems can readily be connected to the triple quadrupole mass spectrometer. The mass spectrometer has several capabilities, such as tandem MS, that will be useful in identification of a wide range of contaminants and interferents, allowing more reliable and thorough results from IMS instruments. We expect that this instrument will become a resource for the Sandia IMS community for testing and improvement of both current and future ion mobility spectrometers.

Contact: Daniel Austin, Biomolecular & Chemical Analysis Dept.
Phone: (505) 284-9852
Email: deaust@sandia.gov

Remediation of Contaminants Using Photochemically Active Nanoparticles

S. Daniel, T. Boyle, K. McCarty, R. Kemp

Motivation: Removal of toxic agents (i.e. viruses, bacteria, nerve agents, inorganic poisons, etc.), from both air and water, present significant challenges to the "active material" used in current decontamination strategies. Photochemical oxidation is an attractive candidate to neutralize these toxins, however current photocatalyst are not sufficiently efficient because of low activity or their required use of UV radiation. For example, titanium oxide (TiO_2) has become of interest to many research groups as a photocatalyst since it is a low temperature, nontoxic, highly stable, cheap, and a highly reactive catalyst that can be used as a decontaminant. However, the processes by which TiO_2 powders have previously been synthesized have lead to extreme variations in its photoactivity. An alternative approach is to deposit metals onto the surface of TiO_2. There is experimental evidence that nanogold becomes catalytically active in the 3-5 nm range. Nanomaterials, in general, are of increased interest due to the surface dominated phenomenon expected at this size scale. Therefore, we have developed a science-based engineering approach to the synthesis of active nanoparticles and their characterization of structural and photochemical activity.

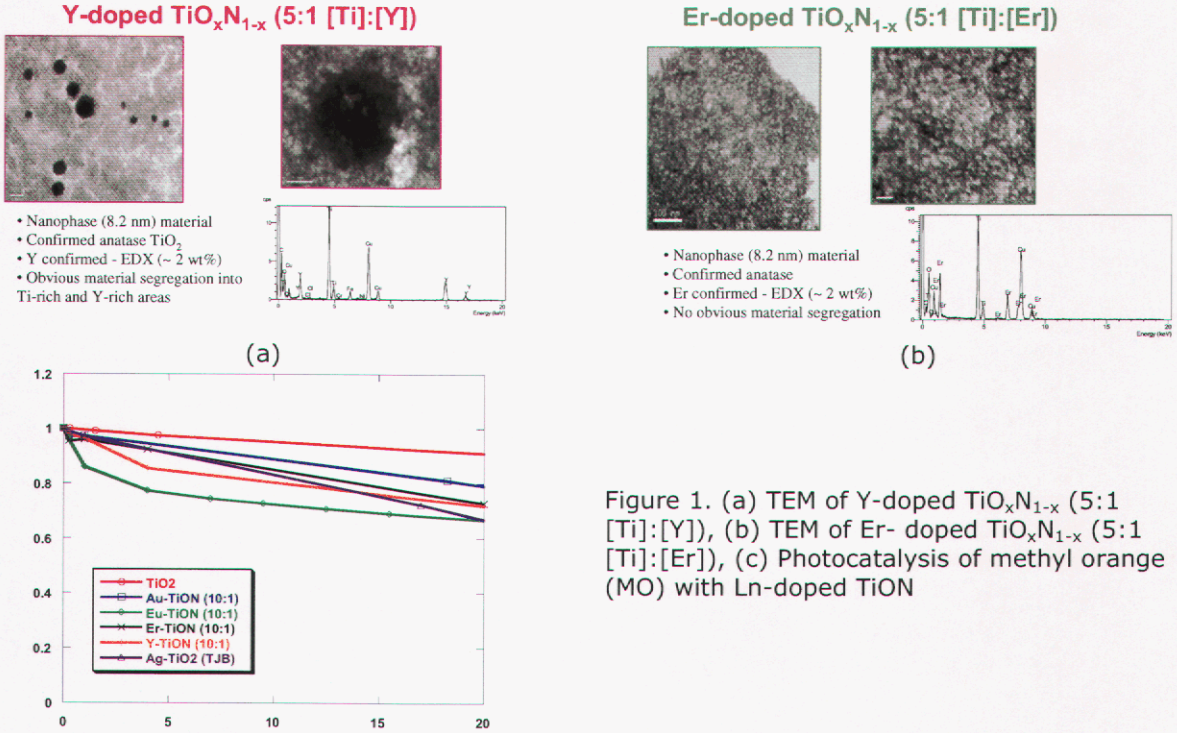

Figure 1. (a) TEM of Y-doped TiO_xN_{1-x} (5:1 [Ti]:[Y]), (b) TEM of Er- doped TiO_xN_{1-x} (5:1 [Ti]:[Er]), (c) Photocatalysis of methyl orange (MO) with Ln-doped TiON

Accomplishment: Our initial investigations focused on anionic doping forming TiO_xN_y materials. Previous experiments showed us that TiO_2 alone displayed photochemical activity in the UV region. Anionic doping of TiO_2 has shifted the

remediation ability of this material to the visible region. Further investigation included doping $TiON_x$ with lanthanides (Figures 1a and 1b). Photocatalysis results monitoring the decomposition of methyl orange (model pathogen) proved the Eu-doped species to have the best activity (Figure 1c). We have also explored alternative schemes for the doping of TiO_2: (i) coating TiO_2 nanoparticles with metals ("core-shell") and (ii) coating metal nanoparticles with TiO_2 ("shell-core"). Therefore, we investigated the deposition of particles of Au onto nano TiO_2 (Figure 2a). Again, photocatalyis results of depositing particles of Au onto the anatase surface showed increased activity. Due to the success of aforementioned experiments, a series of lanthanide oxide nanoparticles using a methyl imidazole/water or microemulsion process have been synthesized. Three precursors were used to determine the best way to prepare these nanomaterials. $LnCl_3$ and $Ln(ONep)_3$ were used in conjuction with the methyl imidazole/water synthesis while $Ln(NO_3)_2 \bullet xH_2O$ was used in a microemulsion process to prepare Ln_2O_3 nanoparticles. $LnCl_3$ and $Ln(NO_2)_3 \bullet xH_2O$ were used because these precursors are commercially available and easy to work with. $Ln(ONep)_3$ was used as a potential precursor due to the fact that our lab has prepared an entire series of $Ln(OR)_3$ materials. TEM (Figures 2b-2d) and XRD results show that the best way to prepare Ln_2O_3 nanomaterials is to use a $Ln(NO_3)_2 \bullet xH_2O$ in a microemulsion process. In addition to all materials prepared, functionalized gold, silver, and iridium nanoparticles were synthesized to gain precise control of particle size and chemical behavior.

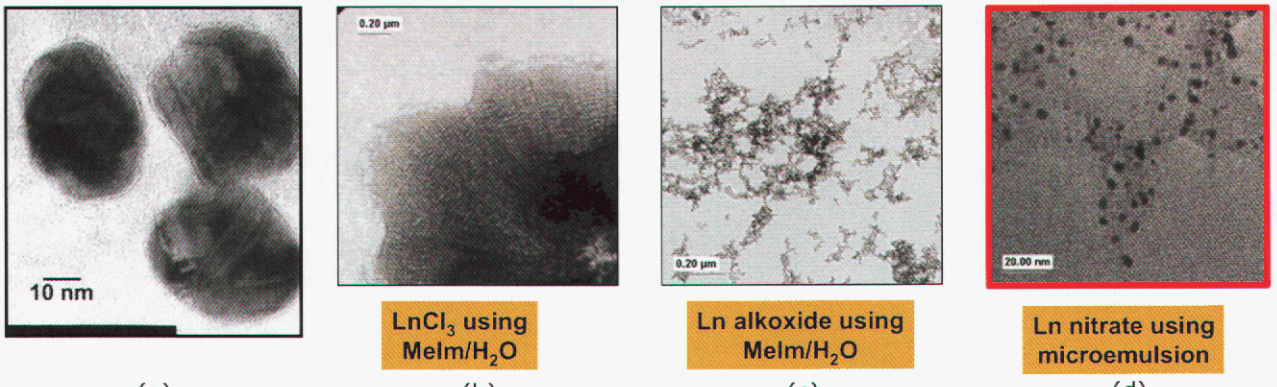

Figure 2. (a) Particles of gold onto nano TiO_2, (b) Nanomaterial prepared from $GdCl_3$, (c) Nanoparticles prepared from $Gd(ONep)_3$, (d) Nanoparticles prepared from $Ho(NO_2)_3 \bullet xH_2O$

Significance: The synthesis of novel photocatalyst with increased photoactivity will be beneficial to decontamination processes. We are also able to gain fundamental understanding of how to prepare tailor-made nanomaterials and how the precursor affects the final morphology of the materials. Lastly, we have positive results to contribute to the functionalization of coinage metals such as Au, Ag, Ir, and Pt.

Contact: Tim Boyle, Ceramic Processing & Inorganic Materials Dept.
Phone: 505-272-7625
Fax: 505-272-7336
Email: tjboyle@sandia.gov

What Is New in Biomembrane Simulations

M. Stevens, A. Frischknecht

Motivation: Understanding the properties and behavior of biomembranes is fundamental to many biological processes and technologies. Microdomains in biomembranes or 'lipid rafts' are now known to be an integral part of cell signaling, vesicle formation, fusion processes, protein tracking, and viral and toxin infection processes. Understanding how microdomains form, how they depend on membrane constituents, and how they act not only has biological implications, but also impacts efforts in development of membranes that structurally adapt to their environment in a controlled manner. The interest in 'rafts' in biology comes from the fact that the membrane influences biological function through the organization of membrane proteins. Thus, the effect of membrane proteins on the bilayer structure and dynamics, and vice versa, is of key importance to understand. This includes protein organization within a bilayer and insertion into the bilayer.

Because lipid dynamics and self-organization in membranes occur on length and time scales beyond atomistic MD, we use coarse-grained models of lipid molecules that spontaneously self-assemble into bilayers. Using such a model we have already demonstrated that the time scales of lipid diffusion and fusion intermediates are accessible to molecular dynamics (MD) simulations. This model enables the study of a whole set of membrane dynamics including those listed above. These coarse-grained models are also used in our density functional theory (DFT) code. DFT provides equilibrium information on membrane structure, free energies and routes to assembly of membrane bound proteins, and free energies of permeation for water, ions, proteins, and toxins as they traverse the membrane.

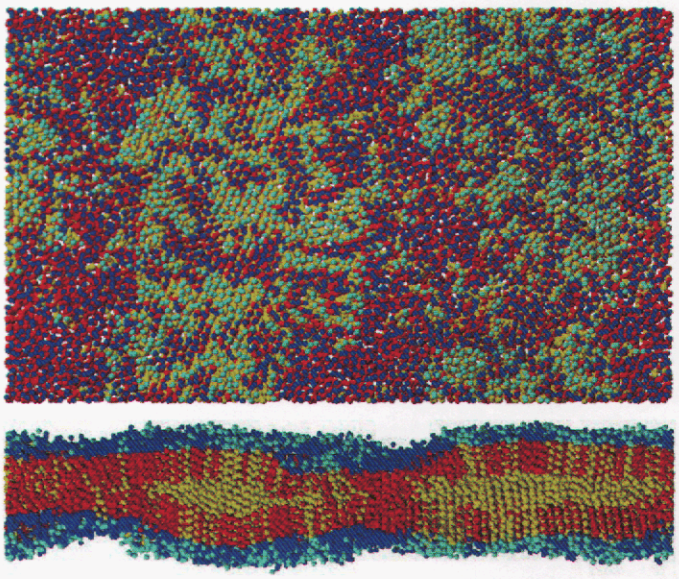

Figure 1. Image of binary lipid bilayer (short and long tail lipids) simulation showing self-assembled domains. The short lipids are colored blue (head) and red (tail). The long lipids are colored cyan (head) and yellow (tail). The solvent is not shown.

Accomplishment: The foundation of our lipid modeling is now well established. The characterization of a set of coarse-grained models for lipid molecules that yield fluid and gel phases has been completed. The area per lipid as a function of temperature has been calculated for a range of lipid tail lengths for saturated and unsaturated lipids. Phase diagrams have been calculated using DFT. This provides us with the necessary information to do simulations of mixed lipid bilayers and

study domain formation in these systems. Two-component lipid bilayers have been simulated to study domain formation. We find that starting with a circular domain for a lipid type in the gel phase surrounded by a lipid type in the liquid phase that the segregated structure is stable for long simulation times. For two-component simulations starting with random distributions, the system evolves into solid and liquid domains. Interestingly, in these simulations, the solid phase is a mixture of the two lipid types. The results are consistent with our AFM measurements for a phosphatidyl choline mixture. The initial DFT calculations of proteins in membranes have been performed. We have also observed the ripple phase in the MD simulations. This was an unexpected result of the simulations, although the ripple phase is well known experimentally

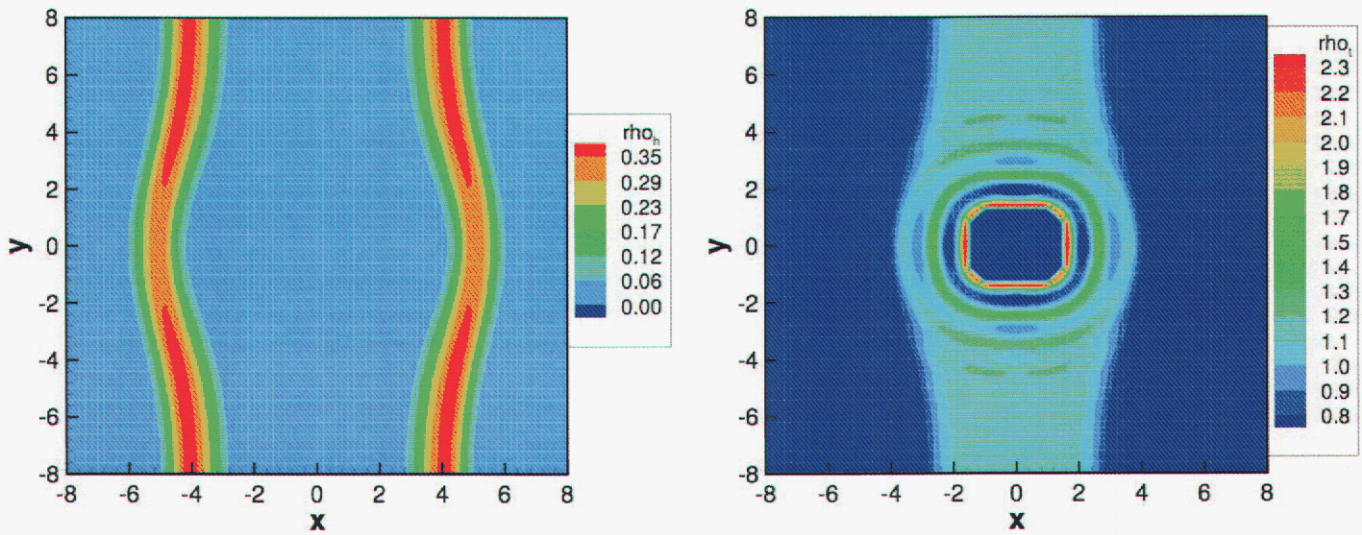

Figure 2. DFT density profiles of head group and tail group about a protein inclusion in the lipid bilayer.

Significance: We have laid the foundations for MD simulations and classical DFT calculations using coarse-grained lipid models to be applied to a variety of phenomena such as microdomain formation, membrane fusion, pattern formation, and protein insertion. We have already obtained important results about the molecular mechanisms involved in membrane fusion and domain formation. This is directing new experiments and providing a basis for interpreting ongoing experimental work.

Contact: Mark Stevens, Computational Materials & Molecular Sciences Dept.
Phone: (505) 844-1937
Fax: (505) 844-9781
Email: msteve@sandia.gov

Observation and Refinement of ErD_2 Thin Films by Time-Of-Flight Neutron Diffraction.

M. Rodriguez, J. Browning

Motivation: We are developing analysis techniques to gain a better scientific understanding of helium evolution in tritide thin films. The importance of this problem stems from the fact that tritide thin films are used in neutron tubes, a component of nuclear weapon systems that must be periodically replaced due to its limited lifetime. We have been curious to see if neutron diffraction could be used as an analytical technique to investigate tritide thin films. The use of neutron diffraction would prove beneficial for detection of hydrogen isotopes because deuterium and tritium have very good neutron scattering ability; this is quite different from X-ray diffraction where X-rays are very insensitive to the single electron present on an H, D, or T atom.

Accomplishment: Neutron diffraction can often be quite challenging for detection of small sample volumes. We hoped to be able to gain sufficient signal from a set of ErD_2 films to bring the phase into the range of detect-ability. We were fortunate to gain access to the HIPPO beam-line at the Los Alamos Neutron Science Centre (LANSCE) to perform our experiment. This beam-line benefited our experiment because the spectrometer has a high intensity neutron beam and a very large array of detector banks. Our idea to improve our chance for ErD_2 detection was to increase the film (ErD_2) sample volume by depositing the films on both sides of very thin Mo sheets. This idea worked. Figure 1 shows diffraction data for 80 ErD_2 films on 40 thin Mo substrates. Although the signal is weak, we can clearly see the ErD_2 (220) peak in the diffraction data; calculated patterns of the ErD_2 fluorite-type structure indicated that the ErD_2 (220) peak was the 100% peak in the diffraction pattern. Refinement results indicated an ErD_2 lattice parameter of a = 5.126 Å and a phase fraction of ErD_2 of 2.1 wt%. These numbers are very reasonable; the theoretical ErD_2 phase-fraction based on the film and substrate volume was 2.6 wt%. Other ErD_2 peaks were also observed but had a tendency to be overlapped with the Mo peaks. Although the Mo substrates were textured, the summed data from all 90° detector banks resulted in

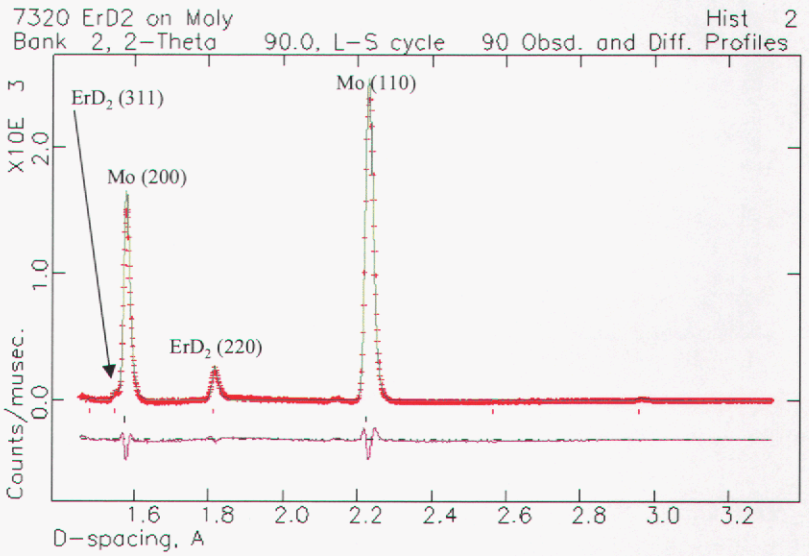

Figure 1. Time-Of-Flight neutron diffraction spectrum showing presence of Mo and ErD_2.

a reasonably random pattern that could be refined with March-Dollase texture correction.

Significance: We consider this experiment a success in that we have now been able to detect and refine ErD_2 as a film. This is significant step forward for the investigation of ErT_2 thin films as the neutron scattering lengths for D (6.671 fm) and T (4.792 fm) are similar. In the erbium hydride system, hydrogen isotopes are known to preferentially reside in tetrahedral (and possibly octahedral sites) of an FCC lattice having the fluorite structure. This raises the questions: "Does tritium site occupation strongly affect the dynamics of helium evolution in the film? Also, do octahedral site vacancies affect helium evolution?" Our refinements on the ErD_2 did verify D on the tetrahedral (¼ ¼ ¼) site and also indicated the possibility of some small site-occupancy of D on the (½ ½ ½) octahedral site in difference-Fourier maps. Figure 2 shows a model of ErD_2 with a difference-Fourier map superimposed. There is still some uncertainty about the validity of the D on the octahedral site as it is hard to refine stability. This could result from the weak signal and lack of good modeling of the texture effects. Regardless, the result gives us some hope that we can be sensitive to octahedral site occupancy in future experiments and begin to probe the impact of site occupancy on ^3He retention.

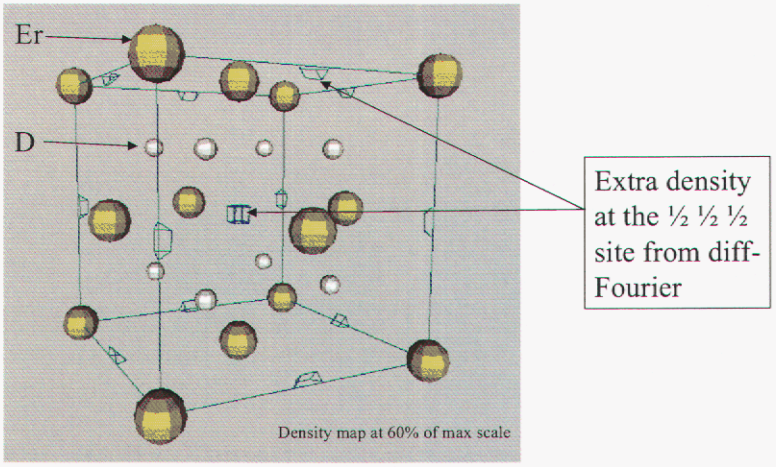

Figure 2. Refined ErD_2 structure with superimposed difference-Fourier map showing possible density on (½ ½ ½) site.

Contact: Mark Rodriguez, Materials Characterization Dept.
Phone: (505) 844-3583
Fax: (505) 844-9781
Email: marodri@sandia.gov

Spectral Texture Measurements with X-ray Diffraction

L. Brewer, M. Rodriguez, P. Kotula

Motivation: The degree of anisotropy in a polycrystalline material (texture) can have a significant effect on its mechanical, electrical, and optical properties. X-ray diffraction (XRD) and neutron diffraction characterization techniques are often used to measure the degree of texture in a material. Standard texture measurements require that the phases present are known and that no stress fields or instrumental misalignments will shift the peaks from their expected positions. This work explores the use of whole diffraction pattern collection followed by multivariate statistical analysis (MSA) to measure the texture from complete unknowns while accounting for sample stress and diffractometer misalignment.

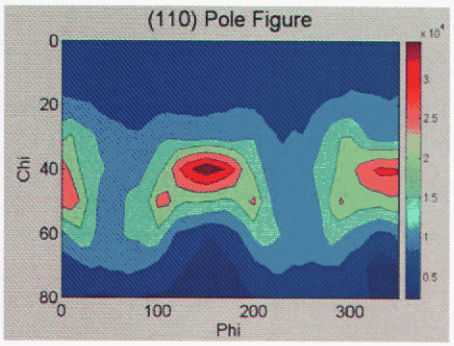

Figure 1. Traditional pole figures calculated by numerical integration of data within specified peak windows.

Accomplishment: Experimentally, this approach involves the acquisition of texture data in an atypical fashion. Traditionally, texture measurements are performed by setting the diffractometer to a single diffraction condition (θ-2θ) for a given reflection from a known phase in the material. The sample is then rotated in angular space (ϕ-in plane rotation, χ-out of plane rotation), and X-ray intensity is recorded as a function of the ϕ-χ coordinate. In the current approach, an entire θ-2θ pattern is recorded for each ϕ-χ value. This arrangement means that 1.) *a priori* knowledge of phases present is unnecessary, 2.) all reflections from a given phase are recorded in one measurement, and 3.) the measurement will account for shifts in 2θ due to stress or diffractometer misalignment.

Analytically, this approach makes use of the multivariate statistical analysis package, AXSIA, developed at Sandia National Laboratories. AXSIA has already been successfully applied for data from energy dispersive X-ray spectroscopy and time-of-flight SIMS measurements. The current work is the first application of these methods to data from diffraction experiments. AXSIA uses a number of multivariate techniques, including principal components analysis (PCA) and multivariate curve resolution (MCR), to generate a full description of the crystallographic variation contained within the data set.

To assess the applicability of these methods, XRD measurements were made on Mo foils. These measurements were made on a standard, Scintag powder

diffractometer with a 4-circle goniometer, using Cu-kα radiation. Data on the Mo foil was collected from 35-90° at 0.05° and 0.1sec/step ranging from 0-80° in χ and 0-350° in ϕ, both with 10° steps.

The traditional pole figures (Figure 1) compared well with the component pole figures (component maps in χ and ϕ) derived via MSA (Figure 2). Traditional pole figures (Figure 1) were calculated by integrating a window in 2θ about a given reflection ({110} or {200}). The component pole figures captured all of the major features of the pole figures while eliminating the artifactual intensity observed in the {200} pole figure. Figure 3 shows the spectral components that correspond to the component pole figures. This spectral information can be used in subsequent analysis of the stress distributions and in the identification and refinement of the crystal structures in the material.

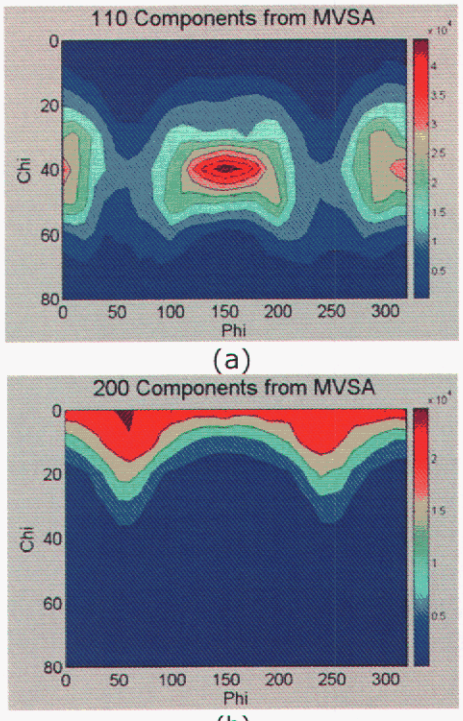

(a)

(b)

Figure 2. Component pole figures from MSA calculations.

Significance: These initial results demonstrate that whole diffraction pattern collection combined with multivariate statistical analysis techniques will allow for the collection and analysis of novel XRD and ND data sets. These sets can be collected from samples with unknown phases, textures, and stress states. Further development of these methods may allow for complete structural refinement of materials in highly textured films.

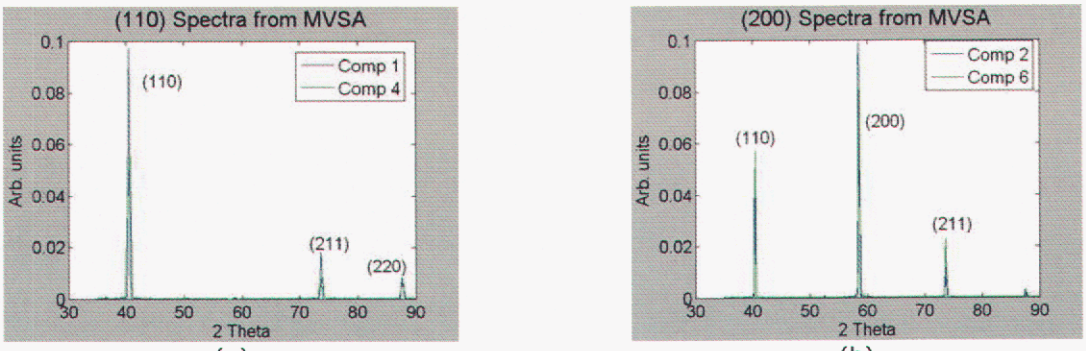

(a)

(b)

Figure 3. Component spectra corresponding to Figure 2.

Contact: Luke Brewer, Materials Characterization Dept.
Phone: (505) 284-2816
Fax: (505) 844-9781
Email: lnbrewe@sandia.gov

Exploiting Bias in Constrained Alternating Least Squares Factor Analysis

M. Keenan

Motivation: Factor analysis encompasses several multivariate statistical techniques that attempt to distill high-dimensional data into a limited number of components while retaining the essential information pertinent to an underlying model. In the context of spectral image analysis, the components represent the spectral characteristics and spatial distributions of the chemical species comprising the sample. Bias plays an important role in factor analysis and we often exploit it implicitly. Constraining abundances and spectra to be non-negative in alternating-least-squares-based multivariate curve resolution (MCR ALS), for instance, is simply a statement that we are biased toward factor solutions that are physically plausible. We are willing to accept a model that provides a poorer mathematical fit to the data in return for model that is easier to interpret in physical terms. In the typical case where component spectra overlap and individual pixels represent mixtures, a large range of factor solutions may exist that satisfy the basic constraints and fit the data equally well. The introduction of mathematical bias by applying constraints, in such cases, may select solutions that are less than optimal. Spectral peak shapes may be distorted, or physically discrete chemical phases may appear to be mixed. The need exists, then, for an algorithm that can offset the constraint induced bias to achieve relatively unique and physically realistic factors.

Accomplishment: Standard MCR-ALS employs classical least squares (CLS) in an iterative fashion to derive spectral pure components and abundance maps. While constraints may introduce only a slight amount of bias into the CLS results at each step, the bias becomes amplified when many iterations are performed. We have developed a family of new MCR ALS algorithms that incorporate biased regression estimators in the least squares procedures. These are patterned after total least squares and ridge regressions, and involve a user adjustable parameter to control the level of bias. The new algorithms can not only offset constraint-induced bias, but provide a general way to control contrast in the extracted pure components.

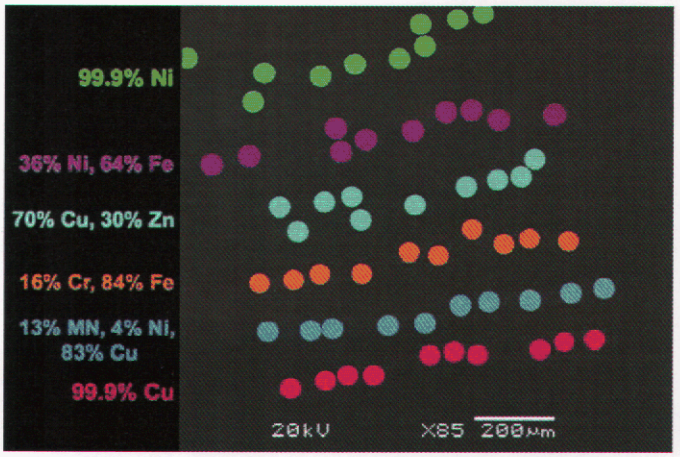

Figure 1. Composition key for an EDS sample in which 6 different alloy wires are embedded in an epoxy block.

The example shown in Figure 1 presents a simple case where contrast adjustment can be useful. The sample consists of 6 different alloy wires embedded in an epoxy block. The individual wires are composed from a palette of 6 elements and the

sample was imaged by energy dispersive x-ray analysis. We expect the wires in this sample to be described by 6 pure components, but the presumed nature of the components is not obvious. There are two equally valid ways of viewing the components, either as alloys or as pure elements. Depending on the particular analytical question, one or the other view might be preferable. The top panel in Figure 2 shows the results of standard unbiased MCR ALS. The components are essentially separated by element. The three wires containing copper are broken out in one component, the two containing iron in another component, etc. This view is one that has high spectral contrast and relatively low spatial contrast, e.g., three different sets of wires show appreciable abundance in the copper component. A biased MCR ALS analysis where the bias parameters have been selected to increase spatial contrast is shown in the lower panel of Figure 2. The wires are now clearly distinguished by alloy.

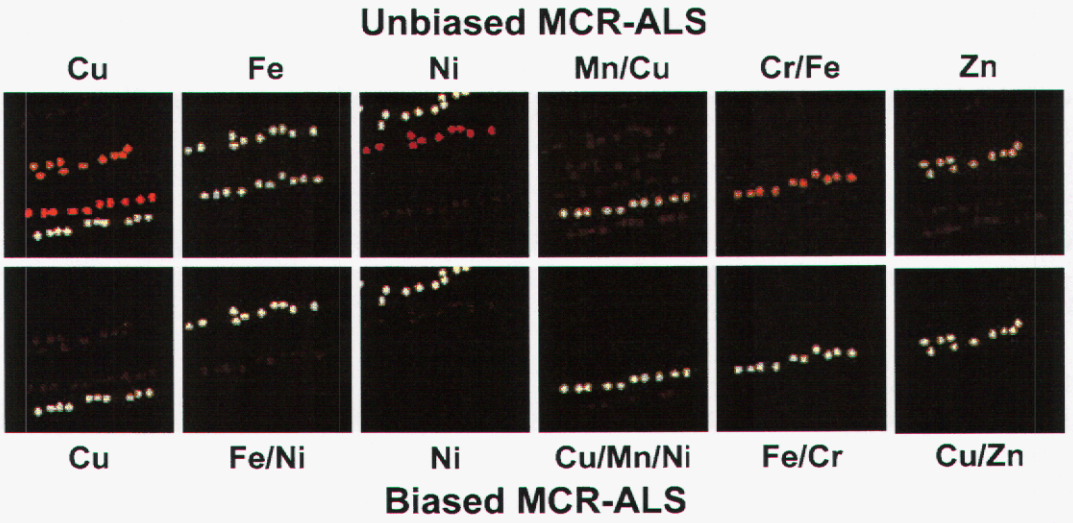

Figure 2. Comparison of the wires sample composition maps derived by standard unbiased MCR-ALS with those obtained using MCR-ALS biased to increase spatial contrast.

Significance: The significance of the new biased MCR-ALS approach is twofold. The algorithms can offset constraint-induced bias yielding more physically realistic components and clearer component separations. Additionally, the ability to introduce bias in a controlled manner increases the power of MCR-ALS as a data exploration tool. It enables the data to be understood from different perspectives and can provide additional insights into spectral data sets that are useful for analytical problem solving.

Contact: Michael R. Keenan, Materials Characterization Dept.
Phone: (505) 844-2190
Fax: (505) 844-2974
Email: mrkeena@sandia.gov

Infrared Depth Profiling Using Infrared Photoacoustic Spectroscopy

M.K. Alam, D. Rivera

Motivation: Stockpile stewardship demands that polymeric material processes be well defined and characterized. Towards that goal several innovative technologies have been applied to the analysis of polymeric materials, including NMR, Infrared and NMR Imaging, TOF/SIMS and others. While all these methods provide unique information useful towards the development and refinement of materials models, these methods require destruction of the sample that can affect the integrity of the information collected. Additionally, depth dependent information within a polymer system has been difficult to obtain, requiring sample destruction

One promising method of nondestructive polymer analysis is photoacoustic infrared spectroscopy. A photoacoustic (PA) detector in conjunction with a Fourier transform infrared (FT-IR) spectrometer provides a non-destructive technique that can greatly enhance the ease with which IR spectra are generated at various depths in the sample. Sampling depths from 10 to 100 microns can be easily obtained with PA FT-IR without slicing the sample. In addition, PA FT-IR has the potential for estimating the depth at which chemical changes occur. We have used the PAS technique to do infrared depth profiling on a number of different polymer systems, including aged and layered materials.

Accomplishment: Experimental verification and understanding of aging in polymers is of fundamental importance to those who deploy polymers in weapons and other systems where stability over long periods of time is critical. Infrared spectroscopy has long been utilized to understand and examine aging byproducts. Understanding how aging proceeds through a sample, is

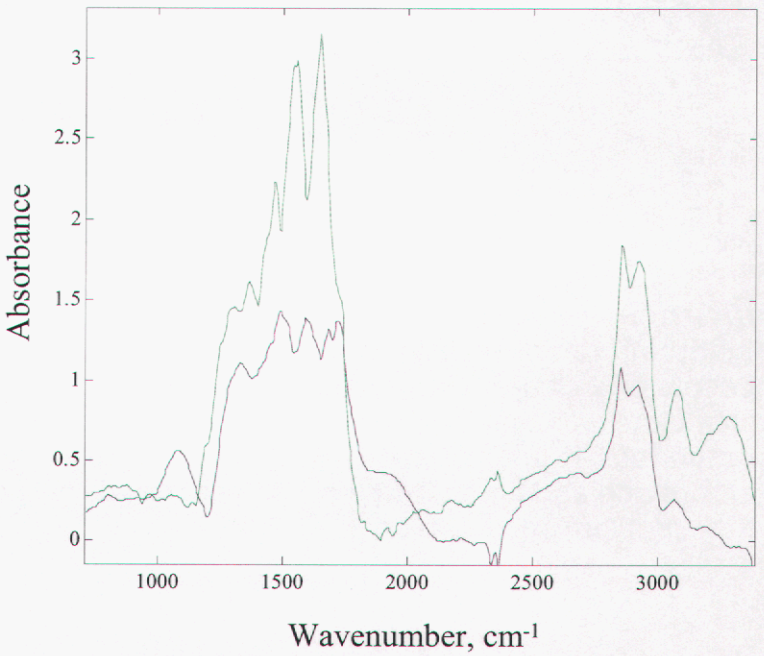

Figure 1 Spectra of aged (green) and unaged (blue) nylon cladding on intact wire sample.

difficult, requiring slices of the polymer to be obtained. Using PAS-FTIR, we have shown that aging in prepared polymer samples can be monitored as a function of depth without sacrificing the sample. (Rivera et. al., SAND2003-4151)

Recently, we examined the aging of wire cladding. Cladding can be very difficult to test due to its geometry. Many sampling methods require the conductor to be removed prior to analysis. Traditional infrared analysis of the polymer conductor required slicing the sample to thickness of 3 um or less in order to obtain transmission spectra, or reflectance spectra could be obtained, if the surface was not highly absorbing. These methods, however, do not provide a depth profile of the chemistry.

Using wires that were environmentally aged we are developing PAS methods to obtain infrared depth profiles from wire cladding. Shown in Figure 1 are spectra collected from aged wire as well as unaged wire samples. The cladding material was nylon. Significant in this work is that the conductor was intact during data collection and no sample preparation had been done other than to cut an appropriate length of wire from the sample spool.

Significance: We have shown that PAS-IR is an invaluable technique for the nondestructive evaluation of materials such as wire, heterogeneous solids, and foams. Using multivariate techniques, such as multivariate curve resolution (MCR), pure component spectra can be extracted from PAS data.

Contact: M. Kathleen Alam, Biochemical and Chemical Analysis Dept.
Phone: 845-9621
FAX: 844-2974
Email: mkalam@sandia.gov

Synchrotron Interface Science: X-ray Absorption and X-ray Photoelectron Spectroscopy

J. Lenhart, D. Fisher (NIST)

Motivation: Knowledge of interfacial phenomena is critical for reliable material design, particularly as interfaces become more prominent in components, and with the current trends towards device miniaturization. For example the interfacial properties of materials play a critical role in many weapon components including neutron generators, firing set applications, electronic devices, sensors, MEMS, etc. In order to understand these interfacial phenomena, measurement technology capable of assessing interfacial properties with high sensitivity, chemical specificity, and spatial resolution must be available.

Accomplishment: Sandia National Laboratories and the National Institute of Standards and Technology (NIST) have engaged in collaboration to build an advanced interface science beam-line at the National Synchrotron Light Source (NSLS) at Brookhaven National Laboratory. Both laboratories have committed capital funding and personnel resources to the new beam-line. In addition, Sandia has gained partnership in a currently available low energy Near Edge X-ray Absorption Fine Structure (NEXAFS) beam-line, which was utilized to study a variety of interfacial issues with polymers including the fracture surfaces of epoxy encapsulants, structure of monolayer anti-stiction materials utilized in MEMS devices, and the orientation and relaxation phenomena in thin polymer films.

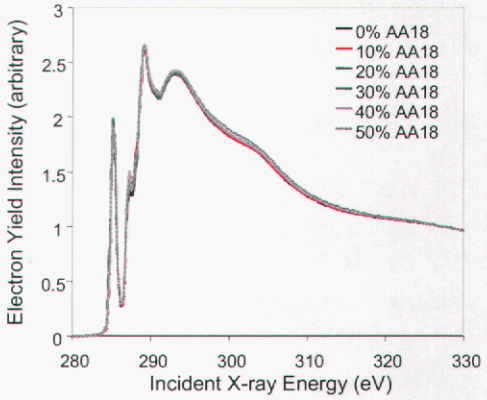

Figure 1. NEXAFS spectra of the fracture surfaces of epoxy encapsulants with various filler loadings. AA18 is an 18 micron aluminum oxide filler from Sumitomo.

The currently available low energy NEXAFS beam-line has an energy range of (200 to 1000) eV. With this energy range, the core level transitions in low Z elements (carbon, nitrogen, oxygen, and fluorine) can be explored. A second beam-line will be improved and rebuilt at the NSLS with high-energy NEXAFS and X-ray Photoelectron Spectroscopy (XPS) capability and an energy range of (1000 to 7000) eV. The synchrotron light source provides high intensity and variable energy incident radiation, which will enhance signal, peak resolution, and depth-profiling capabilities compared to standard laboratory instruments. For example, the brightness of the synchrotron source is 10^5 to 10^9 times that of a standard X-ray tube, allowing more monochromatic incident radiation and improved peak resolution as well as signal-to-noise. The higher energy of the new beam-line will also expand the accessible elemental range over the current low energy beam-line, providing the possibility for NEXAFS studies on a wider range of materials.

Low energy NEXAFS was successfully utilized to investigate the fracture behavior of filled epoxy resins. Figure 1 shows the carbon K-edge NEXAFS spectra of the

fracture surfaces for a series of epoxy encapsulants loaded with various volume percents of 18-micron aluminum oxide filler from Sumitomo. The peaks present in the NEXAFS spectra represent different types of carbon bonding. The carbon chemistry of the fracture surface is independent of the filler loading. The oxygen K-edge NEXAFS spectra (not shown) of the fracture surfaces exhibited an increasing signal associated with the aluminum oxide filler with increasing filler loading, indicating that the fracture occurs close to the filler surface rather than in the bulk resin. Since the fracture occurs near the filler-polymer interface, and the carbon edge NEXAFS spectra were independent of the filler loading, this indicates that the chemistry of the epoxy resin near the filler surface is the same as the bulk chemistry.

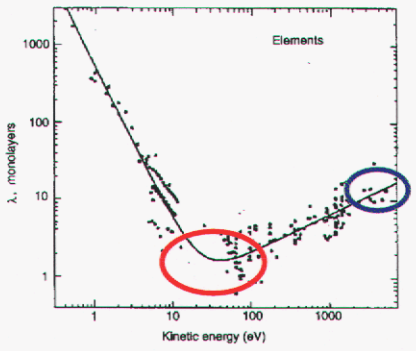

Figure 2. The "Universal Curve" describing electron attenuation depths in XPS as a function of the kinetic energy of the ejected electron.
Figure 2. The "Universal Curve" describing electron attenuation depths in XPS as a function of the kinetic energy of the ejected electron.

The variable low- to high-energy beamline that is currently under reconstruction will have an XPS imaging detector on the end-station. One important advantage of high-energy synchrotron based XPS is the tunability of the incident X-ray radiation. If the incident X-ray energy is varied, then the kinetic energy of the ejected electron also changes. This allows improved depth profiling capability over typical laboratory based XPS. Figure 2 shows the "universal curve" describing the effective attenuation depth of an electron as a function of the kinetic energy of the electron. Laboratory based XPS often operates near the minimum of the curve (red circle) where the attenuation length of the electron is only a few monolayers. This makes laboratory based XPS extremely surface sensitive, and contamination layers can interfere with analysis. With synchrotron based XPS, the energy can be tuned up the universal curve (blue circle) to escape depths near 10 monolayers. A larger portion of the signal will originate from below the contamination layer allowing studies of the desired underlying interfacial region. In addition, the energy can be tuned up and down the universal curve allowing effective depth profiling.

Significance: Synchrotron based interface science capabilities will allow enhanced materials analysis over typical laboratory based instruments. This technology will be utilized to develop a better understanding of interfacial materials phenomena allowing for improved materials design and improved stockpile surveillance.

Contact: Joseph L. Lenhart, Organic Materials Dept.
Phone: (505) 284-9209
Fax: (505) 844-9624
Email: jllenha@sandia.gov

The Analysis of Materials Processing Effects on Complex Surfaces Using ToF-SIMS Spectral Image Series Analysis

J. A. Ohlhausen, R. Kilgo, M. Keenan

Motivation: As parts are subjected to differing processing steps during manufacturing, the chemistry of the surface can change. Changes in surface chemistry can affect bonding, corrosion resistance and aging behavior. Measuring the effects of processing can be very difficult, especially when the surfaces of the parts of interest are heterogeneous in material type, contamination type and contamination coverage. In Time-of-Flight Secondary Ion Mass Spectrometry (ToF-SIMS), spectral signatures resulting from subtle chemical changes across the surface are complicated by the extreme differences in secondary ion yields caused by differing materials matrices from the same image area. As a result, comprehensive surface chemical analysis of these types of parts as a function of processing has been difficult to perform.

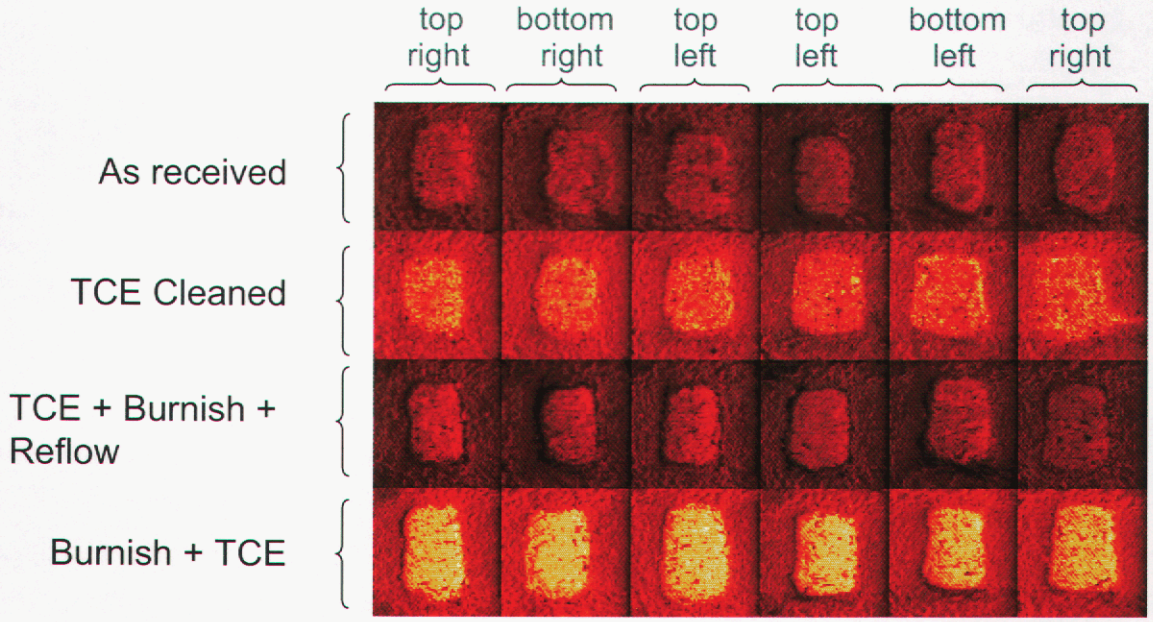

Figure 1: Analysis montage key. Rows denote different samples which had undergone unique processing conditions, while columns correspond to different areas of the sample surface.

Accomplishment: We have successfully applied multivariate analysis methods invented at Sandia National Laboratories to these systems to provide a comprehensive spatial chemical inventory of numerous heterogeneous ToF-SIMS spectral images at once. Figure 1 shows the location of each of the analysis areas used in this analysis. A total of 24 sites were analyzed, obtained from 4 different samples, 6 sites per sample. Once all individual site analyses were performed, the resulting spectral image 'data cubes' from each site were concatenated together to form a single large 'data cube'. Automated eXpert Spectral Image Analysis (AXSIA) was used to perform the multivariate analysis on this 'super' data set. The resulting component separation yielded 19 components consisting of concentration maps

(images) along with their characteristic spectral shapes (chemical fingerprints.) Several selected components are presented in Figure 2. From these and other components in the analysis, processing effects are determined.

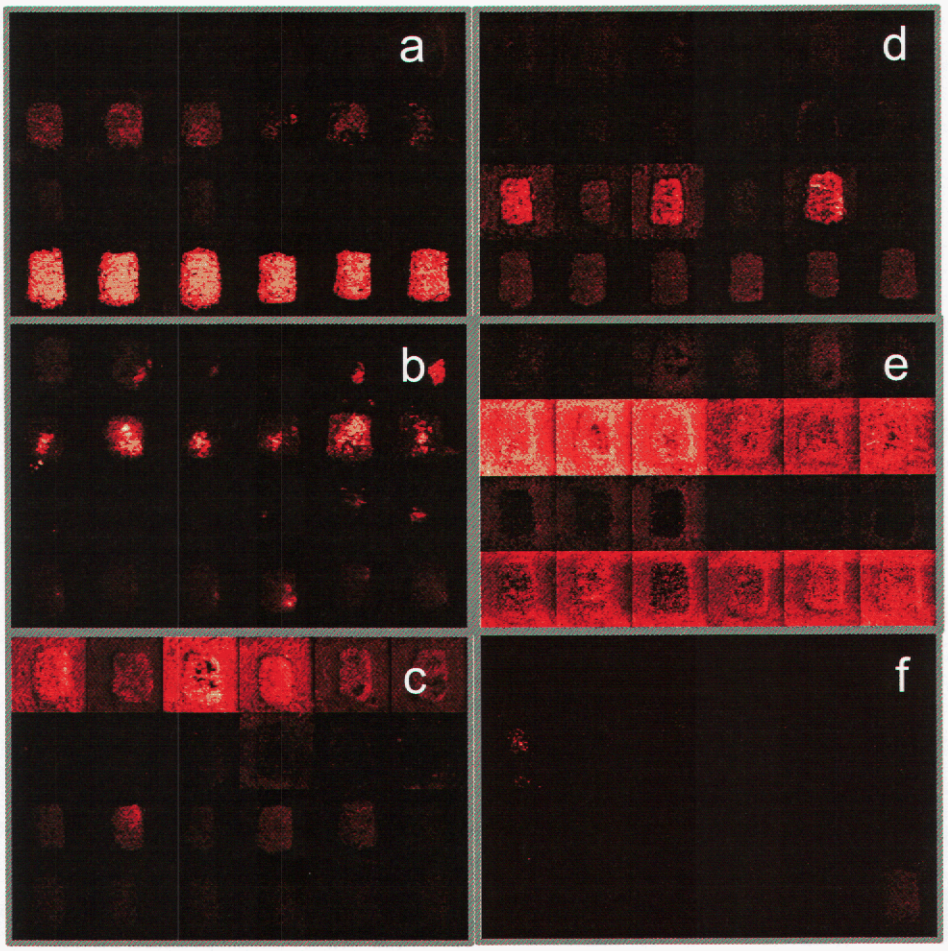

Figure 2: Select component results from the 19 that were solved: a) Solder contamination, b) Copper, c) Silicone, d) Burnishing eraser, e) Lead, f) Teflon particles.

Significance: This new method of ToF-SIMS analysis provides a direct comparison of multiple heterogeneous sites from multiple samples which were processed in different ways. Surface chemical changes resulting from processing variations are easily distinguished in an extremely complex data set. Without the aid of multivariate analysis, this type of analysis is extremely difficult to accomplish.

Contact: James A. Ohlhausen, Materials Characterization Dept.
Phone: (505) 845-9510
Fax: (505) 844-7425
Email: jaohlha@sandia.gov

The Application of Cryofocusing Offgas for Trace Level Detection in Weapon Components

T. T. Borek

Motivation: As materials in the Nuclear Weapons Stockpile age and are exposed to various stresses associated with storage, such as thermal cycling, corrosion, and radiation, a certain amount of decomposition of polymeric species may be expected. In an effort to determine what, if any, volatile species are present in some polymeric species from the stockpile, gentle heating combined with cryofocusing of organic species prior to separation by gas chromatography with detection and analysis by mass spectrometry (GC/MS) was performed. This analytical scheme can provide information on which materials are degrading and which materials are acting as 'sinks' for evolved organic species.

Cryofocusing gas samples is an environmental monitoring sampling technique that has been applied to the analysis of gas samples up to 2 liters in volume for trace organic contaminants. The cryofocusing inlet system can minimize interferences from carbon dioxide and water vapor, and concentrate organic species in the parts-per-billion to parts-per-trillion range. This technique is not selective; all species present in the sample are analyzed, as opposed to absorbent-based techniques that can be selective in the species retained for analysis. The use of calibration gases and internal standards verify that the entire inlet system is performing optimally.

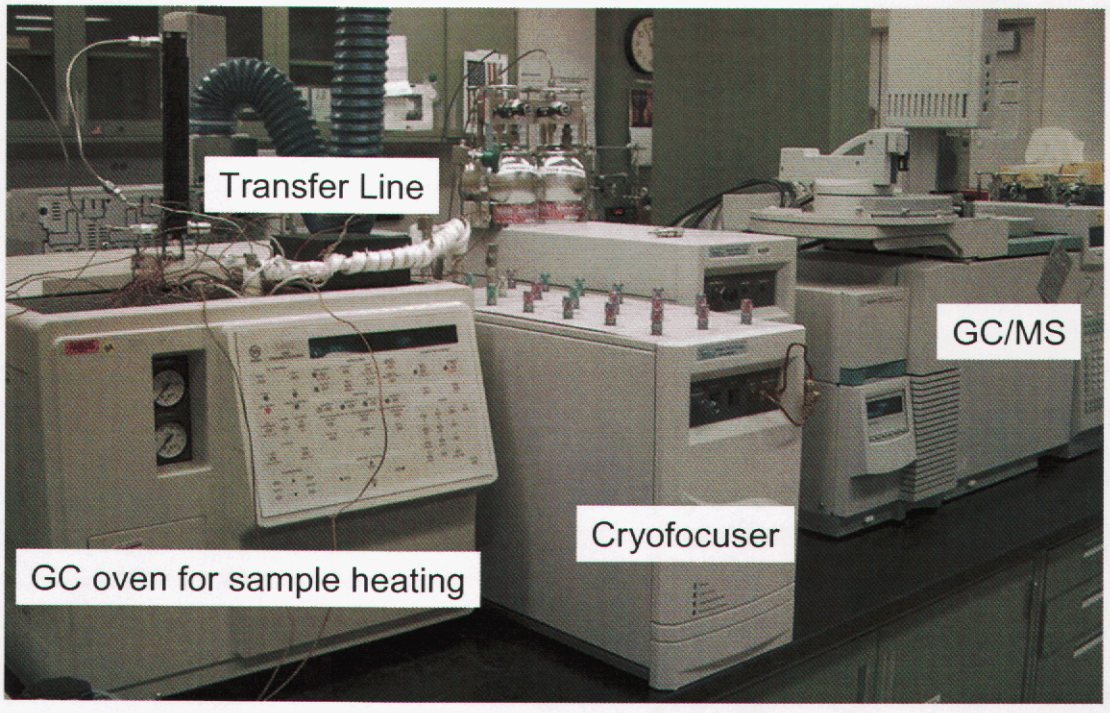

Figure 1. Cryofocusing inlet system coupled to gas chromatograph with mass spectrometry detection and analysis.

Accomplishment: Several polymeric materials from the Stockpile, including Sylgard and thermal barrier silicone, have been examined by gentle thermal treatment with cryofocusing/GC/MS analysis. Figure 1 shows the analytical apparatus. With heating to 70°C, many organic species were observed in both the field return specimens and materials that were subjected to accelerated aging.

Figure 2 shows the results of the analysis of a Sylgard from a B83 firing set. There are several species present in different concentrations. The major species present are organosiloxanes; from trimethylsilanol to large cyclic and linear siloxanes. Also present are some trace amounts of halogenated solvent. The analysis of specimens that were aged shows the same siloxane species at much lower concentrations.

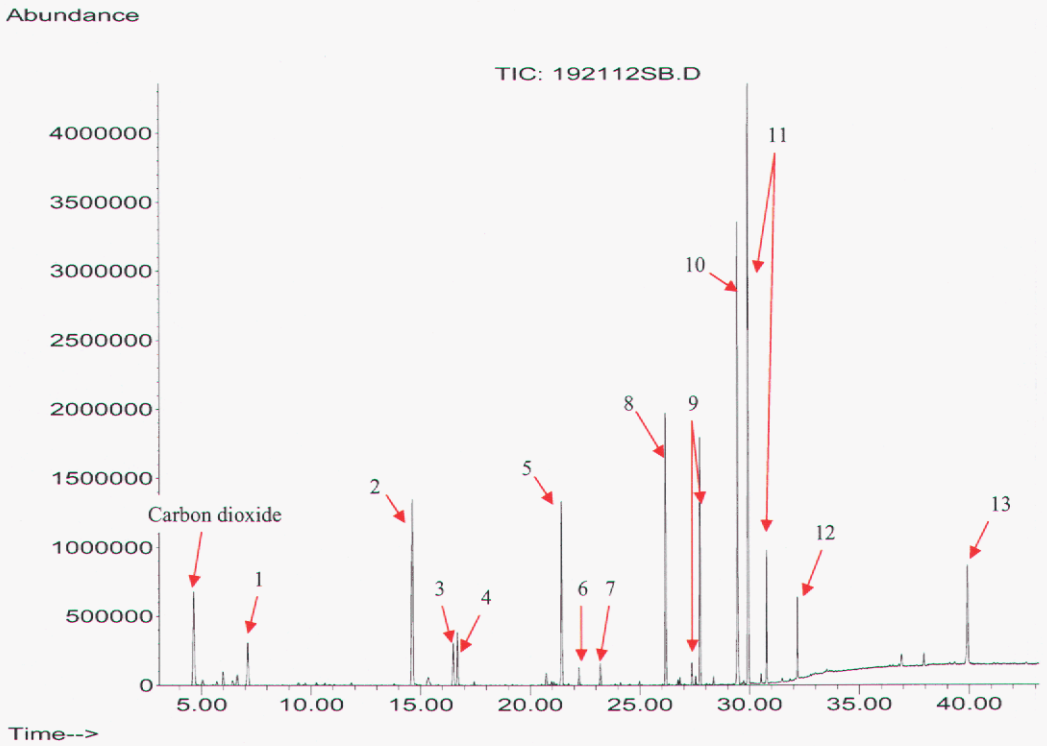

Figure 2. Total ion chromatogram of a Sylgard sample from a field return B83 firing set.

Significance: The ability to detect these species from field return samples can assist in determining potential sources of contamination and corrosion. The application of this technique can help with the decision processes for replacement materials to minimize sources of chemical contaminants and corrosive gases in a weapon atmosphere. Also, gentle heating is only one option for sample introduction; high temperature heating, photolysis, and other aging processes can be examined in real time using this technique.

Contact: Ted Borek, Materials Characterization Dept.
Phone: (505) 844-7758
Fax: (505) 844-2974
Email: ttborek@sandia.gov

Use of Silicon-Coated Germanium Attenuated Reflectance Plates for the Infrared Analysis of Organosilane Films

D. Tallant, D. Adams, M. Garcia, M. Kent, H. Yim

Motivation: Thin films of organosilanes promote adhesion, durability and corrosion resistance. They are also used as lubricants in microelectromechanical systems (MEMS) devices. We are interested in the binding chemistry and subsequent reactions under high humidity of thin films of these materials. Our initial studies have focused on 3-glycidoxypropyl-trimethoxysilane, or GPS, on silicon substrates. We required a surface (silicon oxide) representative of glass fibers or MEMS devices and a characterization technique sensitive enough to produce high quality spectra of the GPS multi-monolayer. Infrared spectroscopy using attenuated total reflectance (ATR-IR) has the sensitivity to detect monolayers of films. In this technique an IR beam is transmitted by internal reflectance down a plate of an IR transparent material. The plate is typically in the shape of a trapezoid or parallepiped. The IR beam samples material absorbed on the surface of the plate at each internal reflection (Figure 1), multiplying the absorption that would occur in a single pass in transmittance. ATR plates made of silicon would provide the desired surface chemistry, but they absorb strongly in the IR fingerprint region and limit IR spectra to frequencies >1500 cm^{-1}. A germanium ATR plate allows access to frequencies as low as 800 cm^{-1}. To simulate a silicon/silicon oxide surface while exploiting the broader mid-IR window of germanium, we evaporated a thin film of silicon on a germanium ATR plate and performed ATR-IR analyses on GPS films coated and cured on the silicon/germanium plate, and subsequently aged in high humidity.

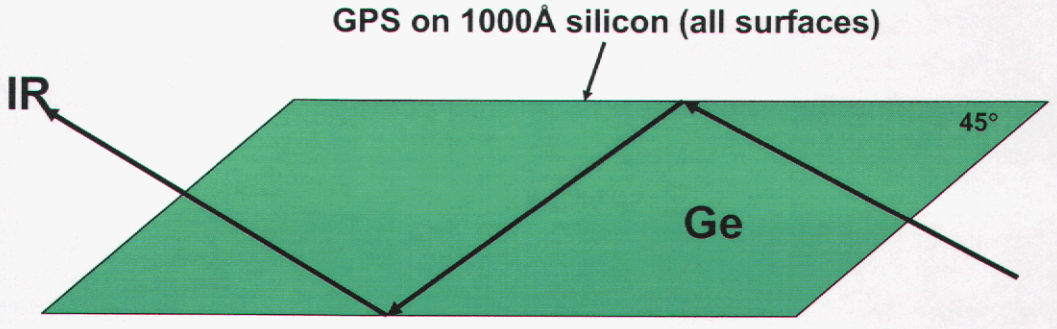

Figure 1. Schematic diagram of silicon–coated germanium attenuated total reflectance (ATR) plate for performing infrared spectroscopy on a GPS film applied to its surface

Accomplishment: Germanium ATR plates were UV-ozone cleaned and coated, by e-beam evaporation in vacuum, on all surfaces with 500 Å and 1000 Å of silicon. The 1000 Å-thick films proved to be more durable, surviving seven days at 80°C and 100% relative humidity. GPS films were dip-coated on the silicon/germanium plates, cured and aged under the conditions just noted. High quality IR spectra were obtained that revealed the chemical transformations occurring during bonding

to the silicon-coated surface (hydrolysis of methoxysilane bonds to form Si-O-Si bonds), curing (loss of –OH and increased Si-O-Si cross-linking) and aging. From the IR spectra obtained during aging we integrated bands characteristic of reacting functional groups in the GPS and bands characteristic of structural or "backbone" groups. Changes in the integrated intensities of these bands indicate reactions associated with the functional groups. Figure 2 plots these normalized integrated intensities versus the days aged at 80°C and 100% relative humidity. The integrated intensities of epoxy-ring-related bands decrease monotonically during aging, indicating epoxy-ring-opening reactions related to attack by water molecules. The intensities of alkane ($-CH_2-$) and ether ($-CH_2-O-CH_2-$) bands increase slightly because they are products of the epoxy-ring-opening reaction. The intensities of structural/backbone modes, $Si-CH_2-R$ and Si-O-Si, decrease as the GPS concentration on the surface of the ATR plate suffers a net loss due to hydrolysis of Si-O-Si bonding to the surface.

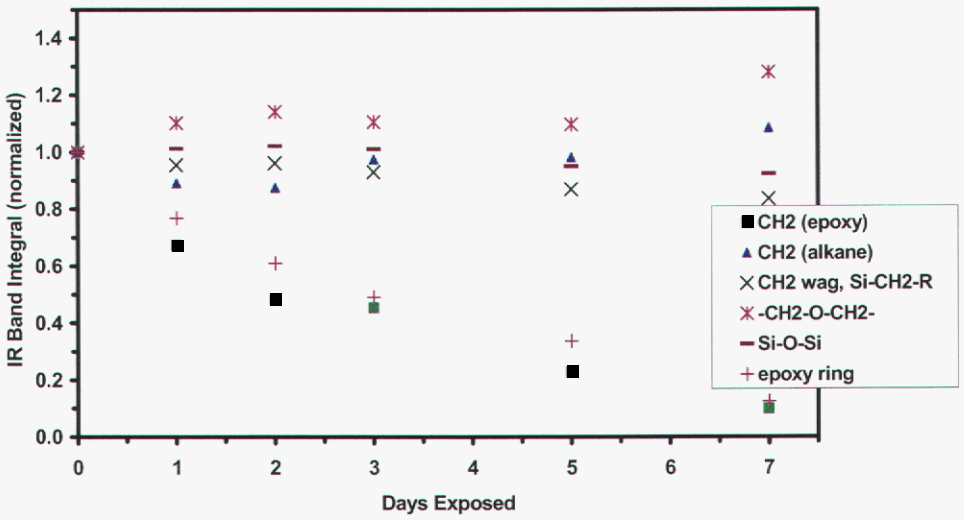

Figure 2. Integrated, normalized intensities of indicated GPS bands obtained by ATR-IR spectroscopy versus days aged at 80°C and 100% relative humidity

Significance: Silicon-coated germanium ATR plates provide surfaces characteristic of those encountered in device applications utilizing organosilanes while providing access to a wide IR window, including the "fingerprint" region. Combined with the sensitivity of ATR-IR spectroscopy for very thin films, they provide a means of identifying reactions affecting these films on "realistic" surfaces and, thus, aid in improving their adhesion, durability, corrosion resistance and lubricating properties.

Contact: David R. Tallant, Materials Characterization Dept.
Phone: (505) 844-3629
Fax: (505) 844-9781
Email: drtalla@sandia.gov

Corrosion-Assisted Degradation in Surface Micromachined Devices: a Directed Aging Approach to Explore Degradation Mechanisms

K. Zavadil

Motivation: The performance and reliability of microelectromechanical (MEMS) devices can be highly dependent on the control of the surface energetics in these structures. Examples of this sensitivity include the use of surface modifying chemistries to control stiction, to minimize friction and wear, and to preserve favorable electrical characteristics in MEMS devices. Silane modification of surfaces through formation of self assembled monolayers (SAMs) is one classic approach to controlling stiction in Si-based devices. The time-dependent efficacy of this modifying treatment has traditionally been evaluated by studying the impact of accelerated aging on device performance. Where performance degradation provides relevant system level information, the underlying chemical and physical mechanisms at the silane-Si interface that precede these changes often remain hidden and therefore this knowledge cannot be used in subsequent optimization of materials and device design.

An alternate approach to gaining knowledge of degradation mechanisms is to conduct aging experiments that target critical steps in most probable failure pathways. We describe this type of aging study as a directed approach. For a silane-terminated Si surface, a probable mechanism is the penetration of water to what is presumed to be a strong covalent siloxane bond produced by a condensation reaction (loss of a water molecule) between the original silane molecule and a surface silanol (SiOH) moiety. Excess water in the vicinity of this bond could drive the condensation reaction in reverse leading to displacement of the molecule, an observed phenomenon in select silane systems. A directed aging experiment to address the underlying role of surface bond disruption involves intentionally incorporating water at the silane-Si interface and exploring the consequences.

Accomplishment: A method has been developed for producing localized water penetration to the silane–Si interface using an atomic force microscope (AFM) with a conductive cantilever under a controlled atmosphere. The topographic image of Figure 1 shows the result of scanning a platinum-coated tip over two 1x1 μm^2 +10 V (left area) or -10 V (right area) substrate-to-tip bias potential at 35% RH.

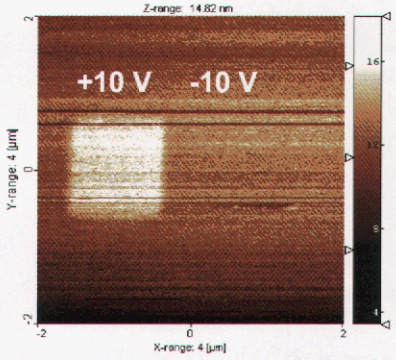

Figure 1: Topographic AFM image of two field- modified 1x1 μm^2 regions showing that water can penetrate to the silane-Si interface leading to anodization.

Approximately 3 nm of new oxide has grown as a result of electric field driven transport of water to the silane–Si interface followed by hydroxyl transport through the existing oxide on the Si

surface. The overall process taking place is the well known anodic oxidation of the Si substrate. The new element of this accomplishment is that lower fields can be used for water penetration prior to the onset of detectable anodization and that novel compositional and mechanical probes can be used to study the local impact of these types of directed changes. A demonstration of this latter aspect is given in Figure 2. A comparably scanned region of a Si substrate shows (Fig. 2a) that the area subjected to field modification at +6 V exhibits a lower coefficient of friction due to chemical changes. These compositional changes can be characterized using secondary ion mass spectrometry. The resulting color representation of composition is shown in Fig. 2b where a distinct 20x20 μm^2 region characterized by contaminant hydrocarbon penetration (from the probe tip) into the silane monolayer is evident. This coupling of directed modification, local force measurements sensitive to topography and chemical environment, and subsequent compositional analysis provides a powerful hybrid approach to the study of degradation mechanisms at length scales relevant to MEMS devices.the probe tip) into the FOTAS monolayer is evident. This coupling of directed modification, local force measurements sensitive to topography and chemical environment, and subsequent compositional analysis provides a powerful hybrid approach to the study of degradation mechanisms at length scales relevant to MEMS devices.

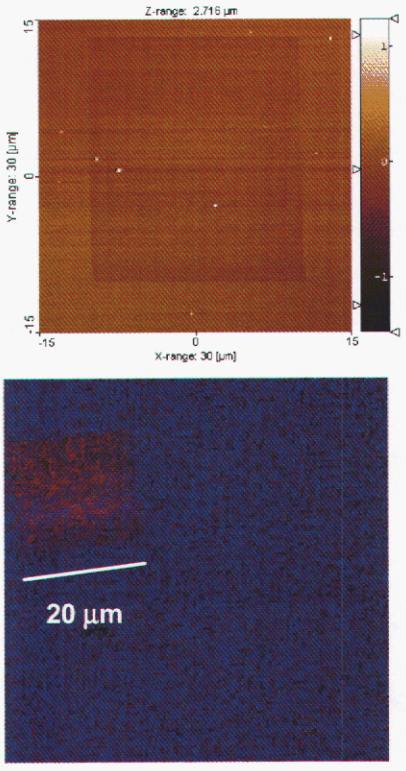

Figure 2: Lateral force (a) and secondary ion image (b) of a field-modified silane SAM on Si showing that the field creates a decrease in friction coefficient and a corresponding compositional change. (SIMS courtesy of J.A. Ohlhausen, Sandia)

Significance: Quantifying device reliability as a function of time and environment requires a knowledge of potential degradation mechanisms for input into aging models. Classic accelerated aging studies show that larger scale processes like silane displacement can occur under certain conditions and that device performance can degrade. This work attempts to develop the tools and understanding necessary to provide a description of most probable degradation mechanisms to the point of generating critical parameter input, like silane displacement kinetics, for these aging models.

Contact: Kevin R. Zavadil, Corrosion & Surface Sciences Dept.
Phone: (505) 845-8442
Fax: (505) 844-4816
Email: krzavad@sandia.gov

Modeling LIGA Microstructures: Atomic-Scale Deposition with Physically-Derived Inputs

C. Battaile, J. Hoyt

Motivation: Sandia maintains a substantial effort in designing, creating, testing, and validating LIGA-fabricated components for weapons systems and other applications. The fundamental physics underlying LIGA electrodeposition technologies are neither straightforward nor completely understood. If more was known about LIGA deposition at the nanoscale, Sandia's LIGA design and fabrication capabilities could benefit greatly. The goal of this work is to develop a physically-based simulation of LIGA metal deposition. Although the process of thin film deposition, and especially of electrodeposition, can be exceedingly complex, our goal is to incorporate as much realism as possible into a deposition simulation that can operate on scales that are relevant to experiments. To that end, we have developed a Kinetic FCC Lattice Monte Carlo simulation of the deposition of Ni onto Cu, and have partially parameterized it with data from atomistic calculation of Ni-Cu and Ni-Ni bond energies. This report outlines the procedures used and highlights some of the results obtained to date.Text in Verdana 11pt

Accomplishment: We use the Kinetic Lattice Monte Carlo method (KLMC) [1] to simulate, on the atomic scale, the deposition of Ni onto a Cu substrate. This approach relies on the rates of deposition and diffusion of Ni atoms onto Cu and Ni surfaces. In order to derive physically meaningful parameters for these diffusion rates, we employ atomistic calculations of the energies of Ni clusters on (100) Cu. By examining the energies of clusters in various configurations, as shown in Table 1 and Fig 1, we can extract the energies of Ni-Cu and Ni-Ni bonds. These energies govern the atom-by-atom deposition and diffusion of Ni. In addition, we incorporate a phenomenological model for the codeposition of a grain-refining agent. This agent serves only to modify the orientation (i.e., grain membership) of the atoms that deposit near it.

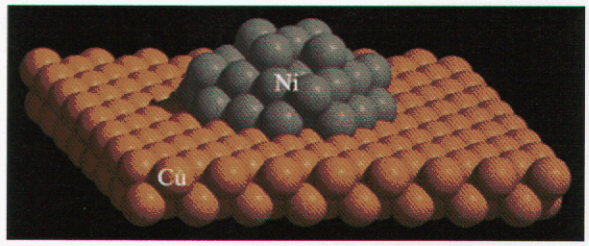

Figure 1. An example of a Ni cluster (grey) on a (100) Cu substrate (brown).

Cluster Size [# atoms]	B_{NiCu} [# bonds]	$B_{NiNi(Cu)}$ [# bonds]	$B_{NiNi(Ni)}$ [# bonds]	E_{EAM} [eV]	E_{fit} [eV]	Error [%]
1	4	0	0	-3.220	-3.221	-0.04
2	8	1	0	-7.240	-6.955	3.93
5	20	4	0	-18.45	-18.16	1.59
9	36	12	0	-35.35	-35.14	0.58
13	52	16	0	-50.13	-50.08	0.10
13*	36	12	20	-52.10	-51.52	1.12
21	84	32	0	-83.74	-84.05	-0.37
48	192	79	0	-193.3	-195.1	-0.94
48*	176	73	20	-194.1	-195.5	-0.77

Table 1. Cluster energy data used in the calculation of interatomic bond energies. B denotes bond count; E denotes bond energy; and the subscripts, NiCu, NiNi(Cu), and NiNi(Ni) denote bonds between Ni and Cu atoms, bonds between Ni atoms that both lie on the substrate, and bonds between all other types of Ni atoms, respectively.

Figure 2 contains microstructures from simulation of the deposition of Ni onto (100) Cu, both with and without the codeposition of the modeled grain refiner. Images of microstructures from experiments [2] are shown for comparison. Qualitatively, the agreement is quite good, although it is clear that the simulations predict a very small grain size because the simulated deposition rate was much higher than in the experiments. (This can be easily rectified, while retaining the grain morphology, once the diffusion frequency is obtained from the atomistic calculations.)

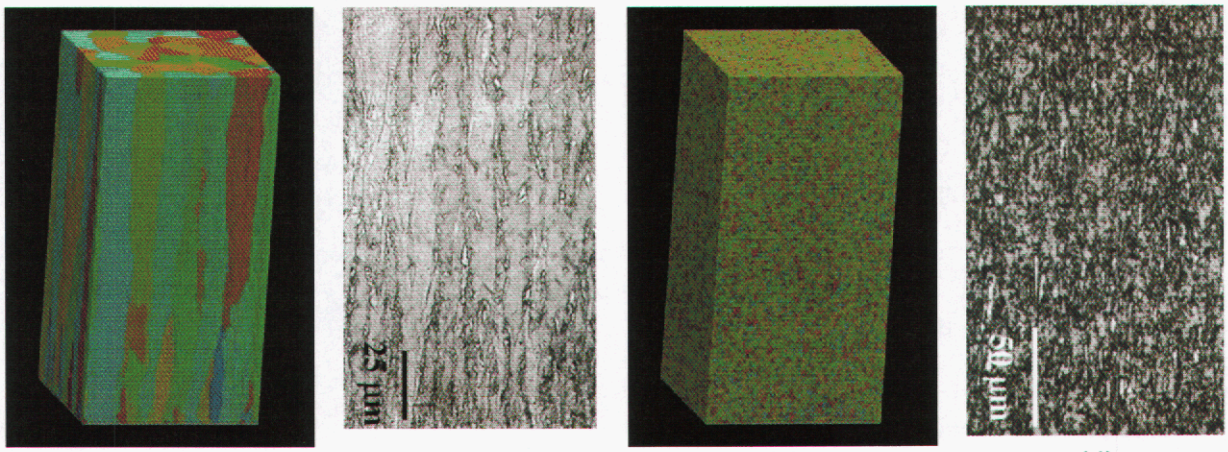

(a) (b) (c) (d)

Figure 2. Microstructures of electrodeposited Ni from a) a simulation without grain refinement, b) an optical micrograph [2] from a Ni sulfamate bath chemistry, c) a simulation with grain refinement, and d) an optical micrograph [2] from a Watts bath chemistry. The simulation domains contain 128 X 128 X 256 FCC unit cells and are approximately 45nm X 45nm X 90nm in size.

Significance: The formation of the microstructure of a thin film depends on the complex and collective behavior of the fundamental nanoscale processes. In the present example, these processes are represented by Ni deposition and diffusion. The KLMC method provides a framework for simulating thin film deposition and microstructure formation in a physically meaningful way, and on time and length scales that are relevant to experiments. Our results demonstrate good qualitative agreement with experimental observations, and continued development of our simulation strategy will produce a simulation tool with sufficient realism to provide insight and guidance to process design and development in a variety of thin film applications

References:

[1] C.C. Battaile and D.J. Srolovitz, *Ann. Rev. Mat. Res.* **32** (2002) 297-319.
[2] T.E. Buchheit, D.A. LaVan, J.R. Michael, T.R. Christenson, and S.D. Leith, *Met. Trans. A* **33** (2002) 539-554.

Contact: Corbett Battaile, Computational Materials & Molecular Sciences Dept.
Phone: (505) 844-7039
Fax: (505) 844-9781
Email: ccbatta@sandia.gov

Nanoliter MEMS Package Gas Sampling to Determine Hermeticity

S. Thornberg, J. Hochrein, T. Padilla, I. Abraham

Motivation: Maintaining the integrity of the internal atmosphere of a hermetic device is essential for long-term component reliability because it is within this environment that many of the internal materials age. As the size of microelectrical-mechanical system (MEMS) packages decrease with miniaturization, characterization of the internal atmosphere becomes increasingly difficult. Typical transistor metal cans and large MEMS devices have an internal volume of tenths of a *milli*liter or more. The atmosphere in these devices has been analyzed routinely for years using conventional gas-sampling technologies. However, many existing MEMS devices have much smaller internal volumes (e.g., 3 *micro*liters with package outside dimensions at ~1 x 2 x 5 mm) and effective gas-sampling methods have been successfully developed and implemented for these volumes. Recently, a need to sample the newest generation of incredibly small MEMS packages having 30 *nano*liters internal void volume (Figure 1) surfaced from a commercial MEMS manufacturer. The high-reliability and severe environment requirements for these devices necessitate that the manufacturer produce hermetic devices.

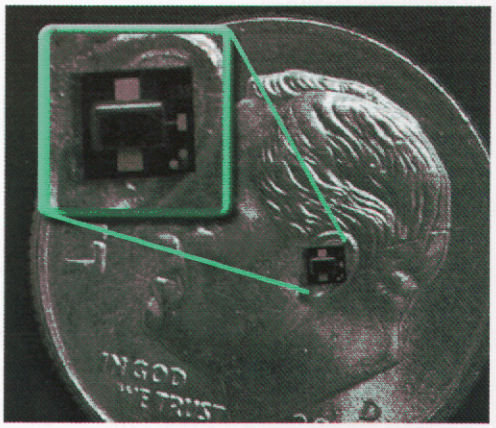

Figure 1. Picture of the 30-nanoliter internal volume MEMS device.

Accomplishment: Gas sampling of hermetic packages typically involves manifold preparation, the careful release of the gases by a physical compromise of the package, and finally determining gas composition with a residual gas analyzer (RGA). Each of these operations was adapted and improved for the *nano*liter MEMS packages. The small volume MEMS packages are now placed in a custom manifold, which is helium leak tested, and then evacuated overnight. The gases inside the package are released by breaking and then analyzed many times by introducing very small gas pulses into the RGA. Several 30-nanoliter MEMS packages have now been sampled successfully and results showed the intended internal gas atmosphere of nitrogen was properly sealed inside most of the packages. However, significant oxygen (> 10%) was detected in some packages, indicating a possible poor seal. Typical data obtained from this type of measurement are shown in Figure 2. In the figure, four pulses of nitrogen gas from the manifold at a pressure of 3 x 10^{-3} Torr were introduced into the RGA. The raw data are presented with no filtering or averaging, which shows a signal-to-noise ratio of approximately 10. The integrated signal (thick "stair-step" line) shows the consistent output obtained from the pulsed technique for introducing gas into the RGA. The key component that permitted this improvement was the incorporation of a picoliter pulse valve into the gas manifold. The integration of multiple pulses reduces the inherent noise of the

RGA when measuring small gas quantities. Several parameters (e.g., pulse duration, RGA gain, vacuum throttle valve) can be adjusted to increase the signal-to-noise ratio even more.

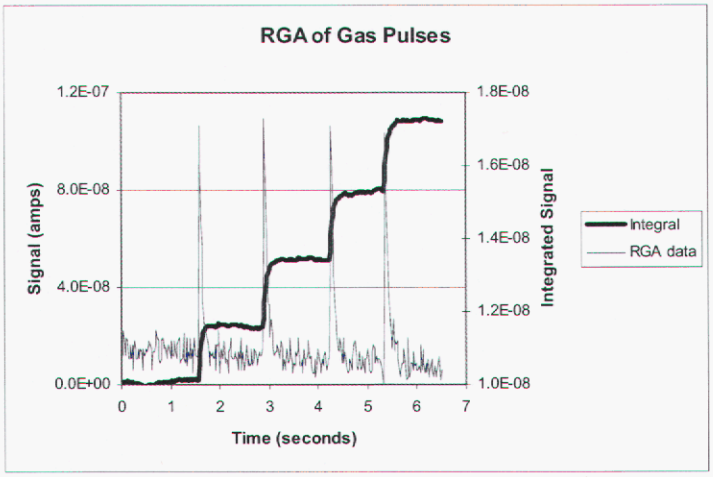

Figure 2. Plot of four pulses of gas monitoring the mass-28 signal (nitrogen/carbon monoxide) in the RGA.

Several other benefits are realized by using the picoliter pulse valve. The first benefit is that the relative amount of gas consumed from the MEMS package is minimized. This enables many analyses of the same device over many minutes to hours, the only limitation being the magnitude of manifold outgassing and leakage. Second, the ability to perform multiple pulses provides the opportunity to collect a statistically significant number of data points. Due to the stable pulse heights, traditional statistical-based analytical techniques are easily applied to the data. Third, the sample size introduced into the RGA can be adjusted so the RGA signal can be optimized to maximize the signal (without going off scale) for various samples. MEMS packages come in many sizes and have a variety of internal pressures and gas types. Consequently, one rigid set of analytical conditions are not optimum for all packages.

Significance: A technique for sampling the internal gas atmosphere in extremely small MEMS packages was developed and successfully demonstrated. The technique represents a radical improvement from previous methods because not only were these MEMS packages sampled, but also the gas from each package was analyzed dozens of times over the course of about 20 minutes. Numerous improvements in the gas-handling manifold (e.g., volume reduction, incorporation of solid state pressure sensor, novel sampling valve) enabled this sampling of 30-nanoliter internal volume packages. This milestone in microanalyses makes possible the measurement of internal gas compositions of extremely small packages, which will enable better assessment of device hermeticity. Additionally, lessons learned from this work increase the fidelity of measurements made on larger packages by reducing outgassing, increasing RGA signals, and enabling multiple analyses for better statistical confidence.

Contact: Steven M. Thornberg, Materials Reliability Dept.
Phone: (505) 844-8710
Fax: (505) 844-7910
Email: smthorn@sandia.gov

New Insights Into Friction from EBSD Analysis of Subsurfaces

J. Michael, S. Prasad

Motivation: Many systems that are important to Sandia National Laboratories core mission contain moving mechanical assemblies (e.g. Stronglinks, sliding electrical contacts, and in the future MEMS) that are subject to friction and wear. Most of these moving parts have surface coatings to combat friction and wear. A clear understanding of subsurface dynamic microstructural changes is needed for predicting the reliability of moving mechanical systems, across all length scales. The study of sub-surface microstructural changes accompanying wear or sliding contact is very difficult. However, the recent developments in the use of focused ion beam (FIB) tools for preparing samples and electron backscatter diffraction (EBSD) for the quantitative characterization of microtexture has finally allowed detailed studies of small wear scars possible. Currently, electrodeposited Ni has been selected as an important structural material for MEMS devices that require more robust physical properties when compared to polycrystalline silicon. In previous studies we have shown that it is possible to visualize the amount of sub-surface deformation that accompanies wear in highly textured electrodeposited Ni. Interpretation of these results directly in terms of the effect of sample texture on deformation was difficult. In order to produce wear scars in a more easily understood geometry we have produced wear scars in single crystals of Ni. This approach should yield new insights into the effect of microstructure and sample crystallography on friction and debris generation.

Accomplishment: The goal is to understand the relationship between friction and microstructure in MEMS devices. We will report on our fundamental studies of sliding wear on Ni single crystals. Wear tracks were produced at low loads in specific crystallographic directions on Ni single crystals. These tracks were cross-sectioned using FIB and then analyzed by EBSD to determine the degree of sub-surface damage as a function of the crystallographic direction. Our primary goal was to gain a fundamental understanding of the relationships between deformation and friction in ductile metals. Figure 1 shows the measured coefficients of friction on Ni single crystals for the crystallographic directions shown. Note the significant differences in the coefficients of friction as we change the crystal direction; among all the combinations we tested, the COF in the <211> direction was the lowest. Figure 2 shows orientation maps of the wear scars

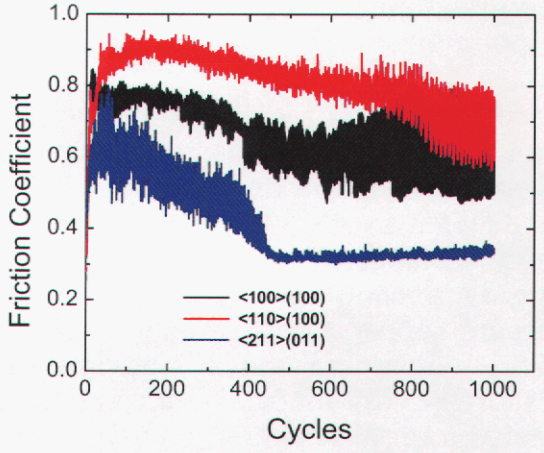

Figure 1. Measured coefficients of friction for Ni single crystals as a function of orientation and number of cycles. <211>/(011) signifies sliding in the <211> direction on a (011) single crystal normal.

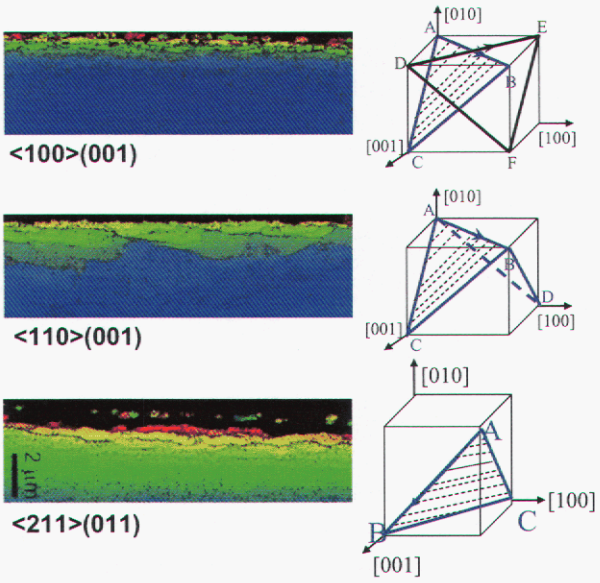

Figure 2. Orientation maps and associated unit cell representations of active slip systems for sliding contact.

obtained using EBSD mapping along with the representation of the unit cells with the operating slip planes indicated. From this data we can begin to understand the relationships between texture and friction. For the <100>/(001) wear scars (the wear direction was (100) and the surface normal was (001)) the friction coefficient is low. In this orientation we see that we have two slip systems operating which results in many dislocation interactions leading to increased work hardening. The work hardened surface is then more resistant to further deformation, thus exhibiting a decreased coefficient of friction. The <110>/(001) wear scars result in two slip systems that intersect along a slip direction resulting in weak dislocation interaction and a smaller amount of work hardening, leading to an increased coefficient of friction. The <211>/(011) wear scars show a different behavior. Here we have only one operating slip system which leads to a very low amount of work hardening. We can see from the EBSD maps that the deformation occurs much deeper in to the sample than in the previous two cases leading one to conclude that the friction would be highest in this orientation. However, Figure 1 shows that the <211>/(011) orientation has the lowest coefficient of friction. We believe that due to the low amount of work hardening in this sample that there is a large amount of dynamic recrystallization that occurs. The dynamic recrystallization results in grains that roll (sort of like ball bearings) which reduces the coefficient of friction. This conclusion is supported by the fine grained region that has developed in the <211>/(011) sample that is not seen in the other wear scars.

Significance: These studies have resulted in a better understanding of the role of sub-surface plastic deformation in the measured friction coefficients. Orientations with strong slip system interactions have higher amounts of work hardening resulting in less sub-surface deformation. However, in orientations with very weak or no slip system interactions, there is high amounts of deformation which results in dynamic recrystallization of the surface which lowers the friction coefficient.

Contact: Joe Michael, Materials Characterization Dept.
Phone: (505) 844-9115
Fax: (505) 844-2974
Email: jrmicha@sandia.gov

PLZT Thin Film High Energy Storage Capacitors for Integrated Microsystems

B. Tuttle, D. Williams, J. Wheeler, T. Headley

Motivation: Next generation surety systems require compact, highly integrated microsystems to improve device functionality, miniaturization, and performance. Capacitors are by far the largest components in these systems; thus, the greatest increase in volumetric subsystem efficiency can be gained by reducing capacitor size. In the last three years, dramatic developments in dielectric science have been reported that can enable 2 to 10 times reduction in capacitor size compared to state-of-the-art (SOA), commercial capacitors. Future generation DOE DP pulse discharge systems will require capacitors with high energy densities that can operate at voltages ranging from 50 volts to 100 volts and are integrable with Si CMOS and MEMS technologies. Novel materials process developments are needed to enable robust, volumetrically efficient capacitors for integrated, miniaturized DOE DP and DOE OAAT subsystems.

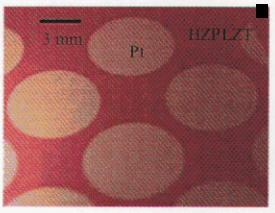

Figure 1. Batch processing of multiple 0.9 μF PLZT capacitors on Si Wafer

Accomplishment: SNL scientists have developed chemical solution deposition process capabilities leading to single layer high Zr content PLZT (lead lanthanum zirconium titanate) films with the largest reported energy densities for PZT based thin film dielectrics to date. An array of fully functional 6 mm diameter PLZT 12/70/30 thin film capacitors deposited on a Si wafer is shown in Figure 1. Because the larger the stored electrical energy density, the smaller the capacitor size, our SNL PLZT thin film capacitor technology is of great interest for miniaturized, next generation DOE DP pulse discharge applications.

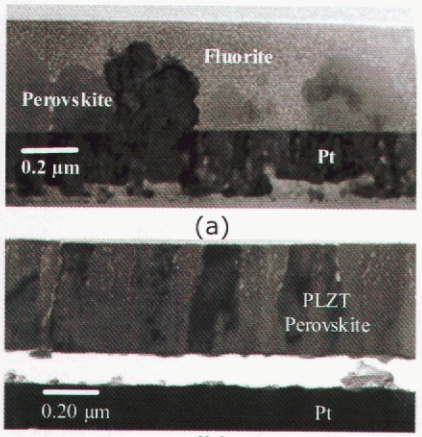

Figure 2. (A) Low dielectric constant (K = 180) PLZT film with Fluorite phase and (B) single phase perovskite film with high dielectric constant (K = 1200) PLZT film.

A significant challenge was to develop process technologies to control the Pb stoichiometry for high PbO activity, high surface area, high Zr content (>70 mol% Zr) PLZT films. Satisfactory control of Pb stoichiometry led to single phase perovskite, high Zr content PLZT films. PLZT films processed using standard processing techniques were not single phase perovskite, as shown by the cross-sectional TEM micrograph in Figure 2(A). The non single phase perovskite film had a dielectric constant of 180 compared to a dielectric constant of 1200 for the single phase perovskite (Figure 2(B)) PLZT film. This high dielectric constant, single phase perovskite film was fabricated using modified process techniques recently developed by SNL scientists. Dilution of the dielectric constant in multiphase films, as shown in Figure 2A, is due to the presence of the fluorite phase which has a relatively low dielectric constant of 50.

Our studies to optimize phase assemblage and to enhance energy density considered seven different process parameters and determined that pyrolysis temperature and use of PbO overcoat layers were especially significant in obtaining single phase perovskite layers that provided the highest energy density films. Transmission electron microscopy analyses were essential in the determination of process-property relationships. TEM analyses indicated that for all films with dielectric constants less than 1000, the fluorite phase was present. Single phase, K = 1200, PLZT film capacitors were fabricated that exhibited breakdown strengths in excess of 1.4 MV/cm and an energy density of 20 J/cm^3. For comparison, the energy densities of conventional state of the art $BaTiO_3$ ceramic chip capacitors are in the 1 to 2 J/cm^3 range.

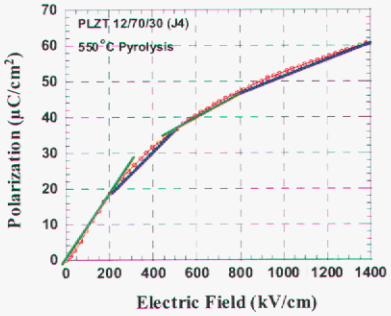

Figure 3: First quadrant polarization versus electric field characteristic with four segment linear approximation for PLZT 12/70/30 thin film.

PLZT film energy densities were calculated from dielectric hysteresis characteristics for fields that were roughly 90% of the breakdown field level (Figure 3). These measurements provide a metric for short term DC or pulse applications. Energy density (E_D) was calculated using two different methods, for which the difference in calculated E_D values was less than 3 percent. The first method used linear dielectric constant approximations for different segments of the first quadrant polarization versus field curves. The integral quantity $E_D = \int PdE = \frac{1}{2} \varepsilon E^2$ was used to calculate the energy density corresponding to each segment. For the second method, the first quadrant electric field versus polarization characteristic was integrated. A dielectric hysteresis characteristic and a four segment linear approximation of the polarization versus electric field characteristic is shown in Figure 3 for a single phase perovskite PLZT 12/70/30 film for a 1.4 MV/cm applied field. The calculated energy density for large area (6 mm diameter) PLZT 12/70/30 film capacitors for the 1.4 MV/cm field was 20 J/cm^3. This is the highest reported energy density for a PZT based thin film capacitor.

Significance: Sandia's increase in capacitor energy storage density of an order of magnitude over conventional state of the art ceramic chip capacitors is significant. SNL engineers and managers have stated that a technology that would decrease the volume of capacitors by 25% would be implemented immediately into specific Sandia subsystems. Our PLZT thin film dielectric capacitors would reduce capacitor size by a factor of ten compared to state of the art $BaTiO_3$ chip capacitors. Further, Sandia's PLZT thin film technology is directly integrable with Si with all processing being performed directly on chip. An important future effort for Sandia scientists will be to develop a viable multilayer PLZT thin film capacitor technology.

Contact: Bruce Tuttle, Microsystem Materials & Mechanical Behavior Dept.
Phone: (505) 845-8026
Fax: (505) 844-9781
Email: batuttl@sandia.gov

Precision Conformal Printing of Materials on Non-Planar Surfaces via Robocasting and/or Micro-Aerosol Deposition

J. Cesarano III, J. Stuecker, D. Sankel, P. Calvert, A. Tappan

Motivation: Freeform Fabrication is the near-net-shape processing of materials by sequentially stacking thin layers in a "2 ½ -dimensional" methodology. Techniques for free-form fabrication with plastics, metals, and ceramics are quite advanced and include stereolithography, fused deposition modeling, LENS, robocasting, etc. Currently, these techniques are limited to building components on a flat planar subsurface. The motivation for this work is to advance the capabilities of the robocasting platform to include conformal precision deposition on non-planar substrates and/or existing components. The technology should also include a versatile material delivery system with deposition methods utilizing extrusion through a small orifice, ink-jet print heads, or micro-aerosol spray heads.

Accomplishment: A manufacturing tool, called robocasting, has been in continuous development at Sandia National Laboratories since 1996. Robocasting is a solid freeform fabrication technique based on robotically controlled layer-wise extrusion of colloidal slurries, pastes, or inks. Extremely complicated structures may be built that contain several materials and internal hidden features. Because the deposition orifice may be less than 50 microns, the robocaster may also be used as a precision printing apparatus. Some of the materials already demonstrated include ceramics, metals, electronic inks and functionally graded composites. A schematic of the robocasting process is shown in Figure 1.

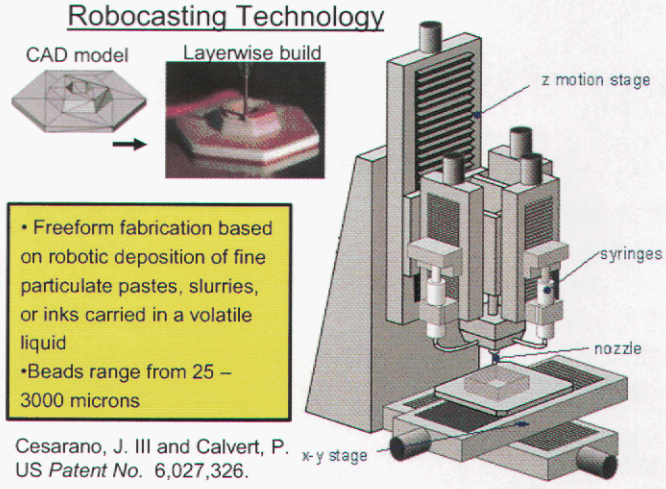

Figure 1. A schematic of the robocasting process.

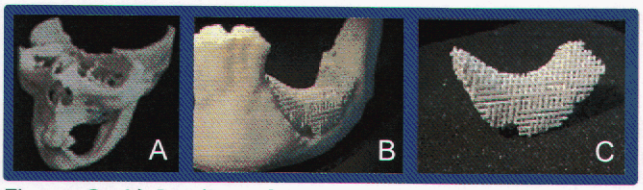

Figure 2. A) Replica of a patient's skull showing the deterioration of the mandible (i.e., jawbone). B) The customized scaffold (including a clearance groove for a nerve) fits nicely into the damaged mandible. C) View of scaffold showing the porous structure that promotes the in-growth of natural bone.

Manipulation of the colloidal interparticle forces provides a means to control the rheology of the slurries. As such, chemical modifiers can be used to induce a tailored yield stress into the slurries and create a paste-like consistency. These pastes can be used to directly fabricate self-supporting lattice structures with out the aid of a support material. The "layer by layer" robocasting process

provides the means to build these porous lattices. It's difficult to imagine how traditional manufacturing techniques could be used to build such a structure. Porous robocasted lattices show tremendous commercial potential as advanced catalyst supports and customized bio-medical bone implants. An example of a customized porous lattice machined into a scaffold that fits into a damaged mandible is shown in Figure 2. The scaffolds are made out of hydroxyapatite and designed to be strong enough to support loads experienced by natural bones while simultaneously promoting the in-growth of natural bone until healing is complete. Prof. Russ Jamison at the University of Illinois is completing animal studies.

Recent mechanical developments to the robocasting platform are the incorporation of *in situ* laser profilometry and deposition heads that deliver droplets of slurries and inks. It is now possible to build structures or print patterns conformally on non-planar substrates. The data from the profilometer provides a topography map the can be used to instruct the robocaster to build on the topography. Figure 3 shows (1) a laser measuring the topography of an alumina dome, (2) a traditional syringe-based extrusion head, and (3) a micro-aerosol deposition head. Also shown are examples of an antennae pattern drawn on a dome and precision deposition of columns of ink-jet-printed inks.

Significance: The Robocasting technique has evolved into a versatile manufacturing tool that enables free-form fabrication of three-dimensional components and/or precise conformal printing. Robocasting technology has become the basis for the development of three-dimensional lattice structures for advanced catalyst supports and customized fabrication of bone implants (see Figure 2). The new capability of conformal printing allows application of antennae and electronic structures on other components and opens the possibility for repairing or modifying components. Additionally, robocasting may be able to play a role in defense applications, remote battlefield manufacturing, and manufacturing/repair in space. With this tool designers may have unforeseen versatility to build components with unique structure and functionality.

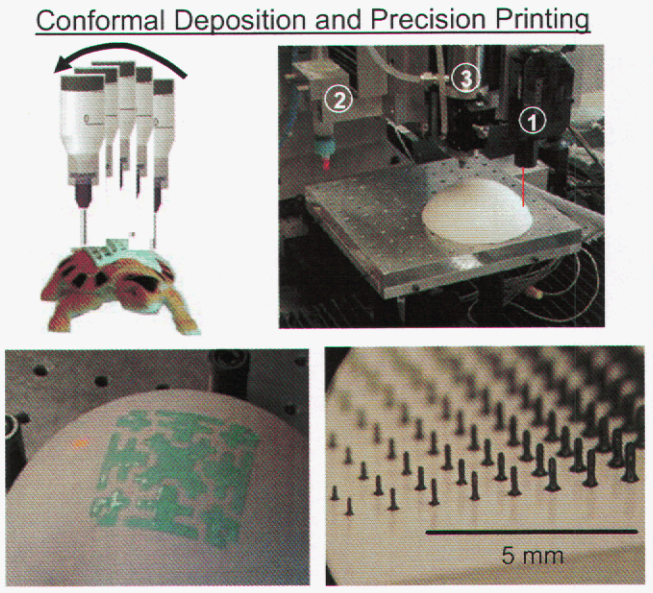

Figure 3. A schematic and photos showing conformal robocasting and precision deposition.

Contact: Joe Cesarano, Ceramic Processing & Inorganic Materials Dept.
Phone: (505) 272-7624
Fax: (505) 272-7336
Email: jcesara@sandia.gov

Science-Based Understanding and Control of Ceramic Sintering Using the Master Sintering Curve

K. Ewsuk, M. Reiterer, C. DiAntonio

Motivation: Defects such as microstructure heterogeneities and distortions in component size and shape after sintering are typical indications of processing problems. Controlled sintering and predictable sintering behavior are required to reproducibly manufacture reliable ceramics. Historically, the processing of complex materials and multiple materials systems has been poorly understood, making it difficult or impossible to predict and reproducibly control densification and microstructure development during sintering. Traditional, empirical engineering approaches do not provide the critical understanding required to efficiently optimize and control materials and processes to meet advanced design, performance, and reliability needs for complex and specialty systems.

We are developing and applying science-based understanding, in combination with practical engineering expertise, to better understand and control ceramic sintering. The objectives of this work are to develop fundamental characterization and modeling science and technology: 1) to predict and control densification and microstructure development during sintering; and 2) to identify the critical factors that influence microstructure development and densification. To achieve this end, we have compiled a tool kit that consists of three validated sintering models that are firmly founded in fundamental sintering theory, including: 1) Sandia's JAS3D continuum finite element (FE) linear viscous sintering model to predict densification and shape change; 2) the Riedel-Svoboda (R-S) microstructure-based sintering model to predict densification and grain growth; and 3) Johnson's master sintering curve (MSC) theory to predict and control densification.

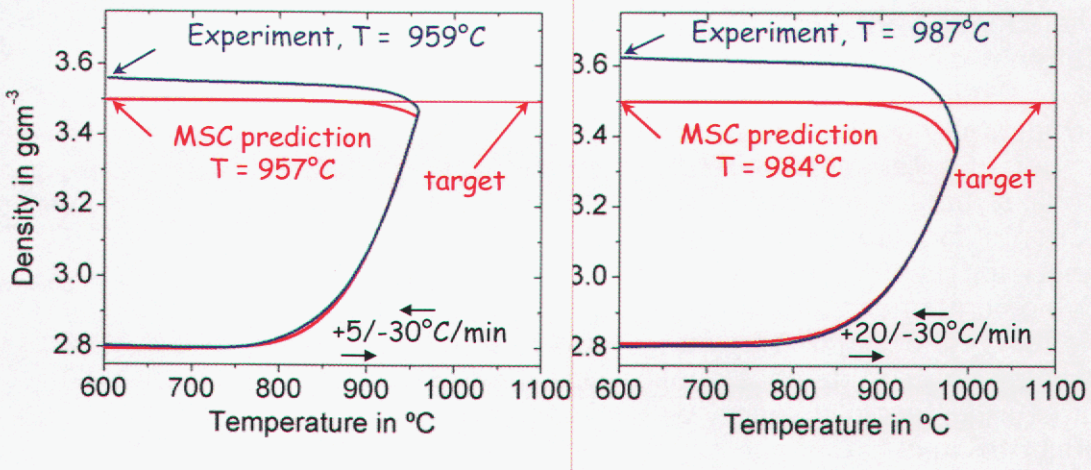

Figure 1. The measured and predicted density with temperature in a ZnO varistor body during sintering at: a) 5°C/min; and b) 20°C/min showing excellent agreement during heating. A peak temperature 2-3°C higher than targeted results in a significantly higher density than predicted after cooling at 30°C/min.

Accomplishment: All three sintering models have been tested and validated by comparison to experimental results and accepted sintering theory. Furthermore, all three sintering models have successfully been applied to better understand, control, and optimize the sintering process, as demonstrated for MSC theory in Figure 1. The MSC accurately predicts the density-temperature trajectory for a ZnO varistor body during the heating stage of the sintering process, and also demonstrates how experimental deviations from the prescribed (i.e., model) time-temperature profile result in significant changes in the final sintered density. Because the properties of a varistor are determined by the sintered microstructure, a change in sintered density can impact the performance and reliability of the sintered body. MSC-based predictions show that the sensitivity of the varistor body to variations in sintered density decrease significantly when a slower heating rate is used during sintering. A heating rate of 20°C/min produces a deviation of ~ 0.1g/cc in sintered density, while a heating rate of 5°C/min produces a deviation of ~0.05 g/cc. MSC theory also has been used to design time-temperature profiles to reliably achieve a targeted sintered density to within <1%. Preliminary results in Figure 2 indicate that different varistor bodies processed to the same density using different time-temperature profiles have the same microstructure and properties (i.e., the regulating voltage). In contrast, varistor bodies processed to different microstructures and densities have different properties.

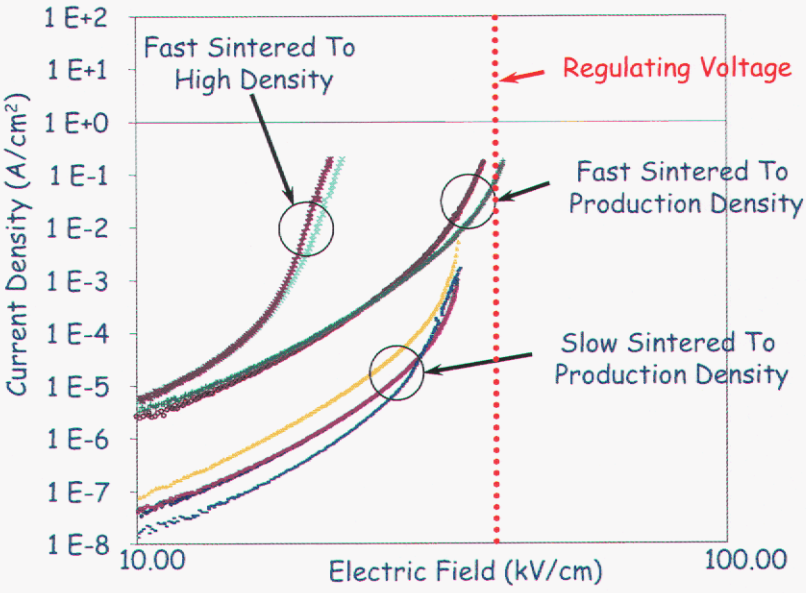

Figure 2. Varistor current density as a function of applied electric field. ZnO varistor bodies sintered to the same (production) density using different sintering profiles exhibit the same regulating voltage.

Significance: Science-based understanding of ceramic sintering is being used to better understand and control the materials and processing required to reproducibly manufacture high performance and high reliability advanced ceramic components.

Contact: Kevin Ewsuk, Ceramic Processing & Inorganic Materials Dept.
Phone: (505) 272-7620
Fax: (505) 272-7304
Email: kgewsuk@sandia.gov

Cold Spray – A Maturing Technology

R. Neiser, A. Hall

Motivation: In performing its mission, Sandia is in constant need of metal, ceramic, and composite materials that have unique compositions, microstructures, and properties. Spray processing of materials is one of the most versatile techniques available for tailor-making materials that meet Sandia's demanding requirements. Cold spray processing is a relatively new technology that provides a unique opportunity to prepare metals with bulk-like electrical and mechanical properties. This process has the unusual quality that it results in minimal oxide inclusion at interparticle boundaries in the sprayed coating. In addition cold spray offers important advantages in the thicknesses that can be attained and in the geometry of the spray plume. Cold spray technology has matured from its inception in the late 1980's in the Former Soviet Union into a commercially reliable tool that is finding its way into industrial applications worldwide. One of the more interesting opportunities for cold spray processing is in the near-net-shape fabrication of parts in air at room temperature. The work presented here demonstrates that a modest thermal treatment, when applied to cold-sprayed aluminum, can produce materials with bulk-like mechanical properties.

Accomplishment: In the cold spray process, finely divided metal particles are accelerated in an inert gas jet to velocities in excess of 500 m/s. If accelerated to velocities above a material-dependent critical velocity, the particles will bond to the substrate and form a dense, well-adhered deposit. This ability to fabricate deposits of low oxide content in air at near-room-temperature conditions is very attractive for many applications. In its as-sprayed state, cold sprayed metals tend to be brittle because interparticle bonding tends to be incomplete and because the particles are heavily cold worked during the deposition process.

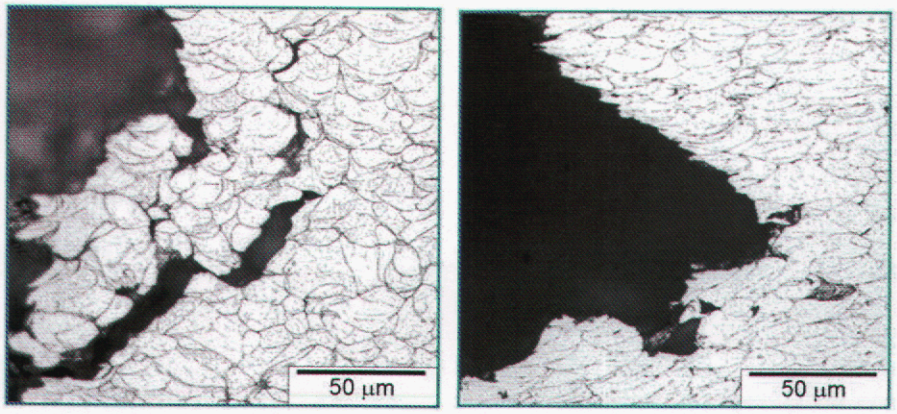

Figure 1. Metallographic cross sections taken from the fracture surface of as-deposited (left) and annealed (right) specimens of cold-sprayed aluminum. Note the brittle, interparticle nature of the fracture in the as-sprayed material and the elongation of grains and tearing evident in the annealed specimen.

Samples were fabricated using a commercially available gas-atomized aluminum powder with a volumetric mean particle size of 12 microns. Using helium as the accelerating gas, the Al particles exited the nozzle of the cold spray device at an average centerline velocity of 1100 m/s.

Tensile bars were machined from the thick deposits that were laid down. Some of these were tested in their as-sprayed condition while others were annealed at 300°C for 22 hours and then pulled. Dramatic differences in the behavior of the two materials were observed, as can be seen in Figures 1 and 2. In the as-sprayed state, the aluminum exhibited less than 1% elongation to failure while in the annealed state it increased to more than 10%. For comparison, the strain to failure of the benchmark wrought 1100 aluminum (H14 condition) is 9%. The ultimate tensile strength of the annealed cold-sprayed material (14-17 ksi or 96-117 MPa) was essentially the same as that of wrought 1100 Al in the H14 condition (16 ksi or 110 MPa), while the Young's modulus was slightly lower (8.3×10^6 psi or 57 GPa vs. 10.1×10^6 psi or 69 GPa).

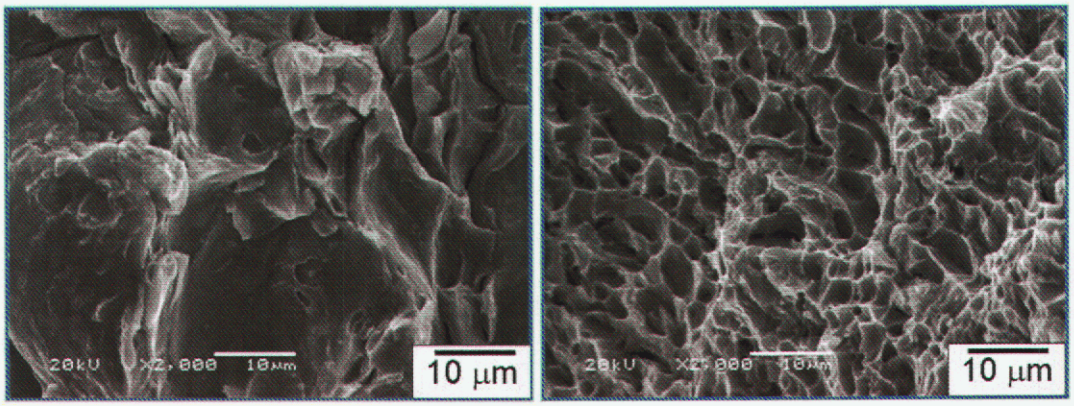

Figure 2. SEM images taken from the fracture surface of as-sprayed (left) and annealed (right) aluminum deposits. The interparticle nature of the fracture can be seen at left. At right, microvoid coalescence, typical of torn ductile metal is apparent.

Significance: In the as-sprayed state, cold sprayed materials typically exhibit minimal ductility. The annealing treatment provided to the cold-sprayed aluminum examined in this study greatly increased the ductility and resulted in bulk-like properties. Typically it is not possible to achieve such dramatic improvements in the bulk mechanical properties of sprayed materials by annealing them. This result is very encouraging and may open up new applications for cold-sprayed materials.

Contact: Aaron Hall, Joining & Coating Dept.
Phone: (505) 284-6964
Fax: (505) 844-6611
Email: achall@sandia.gov

Modeling the Microstructure of Flame-Sprayed Coatings

E. Webb III, C. Battaile

Motivation: Flame-sprayed coatings are created via high-energy deposition of molten particles onto a substrate in a process somewhat akin to ink jet printing. The significant difference is that an entire surface (or component) is coated with the deposition material and, since the material being deposited is typically a metal or oxide, flame-spray is a high temperature process. This combination of high energy and temperature results in lamellar morphologies consisting of a fairly random stack of individual 'splats' along with a relatively high degree of porosity. This microstructure imparts excellent mechanical and electromagnetic shielding properties to flame-sprayed coatings, making them ideal candidates for protection of critical stockpile components. This is borne out by their use in current devices as well as by the coating community's desire to extend flame-spray to further applications.

Developing process/microstructure relations for this complex process is challenging such that process experiments have been limited in their success. In addition, microstructure/performance relations are lacking. Mechanical shock experiments on coatings with carefully characterized microstructures are expensive and data interpretation is not straightforward. Thus, a modeling component is crucial for elucidating the relations between process, microstructure, and properties and has the potential to improve performance for current applications while at the same time opening the door for future applications.

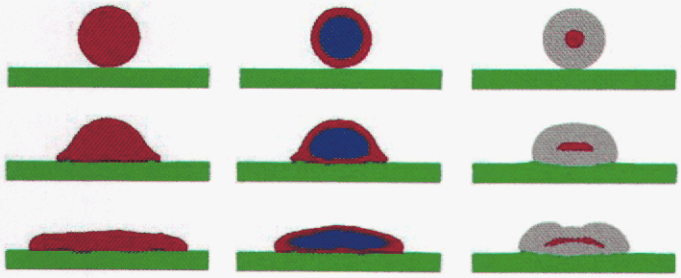

Figure 1. Snapshots from simulations of single droplet splat events under (a) ideal conditions, (b) conditions where the drop is only partially molten on its exterior, and (c) conditions where a solid skin (e.g. oxide layer) has formed on the droplet.

Accomplishment: The goal is to use atomic-scale simulations of splat events to provide highly detailed information for developing the parameters of a larger length scale model that generates complete coating microstructures. Model microstructures would then be incorporated into existing Sandia continuum response codes to test their performance. A critical first step in this is to demonstrate that varying process conditions can be captured in the atomic-scale simulations. Figure 1 shows the results of molecular dynamics simulations of single splat events for varying process conditions. In Figure1 (a), the ideal case is shown where the deposition material is completely molten. Figure 1(b) shows the same conditions as far as impact velocity and incident angle; however, in this case the deposition material is only partially melted to mimic the effect of lowering torch energy. Figure 1(c) shows splat impact for the case where a solid 'skin' has formed on an otherwise molten particle; this models the effect of a more oxidizing

environment. It is obvious from Figure 1 that the varying process conditions modeled have resulted in different splat morphology. Ongoing work is examining the differences in structures of coatings deposited under these varying conditions.

A larger length scale model has been used to generate a simulated flame-spray coating, shown in Figure 2(a). While this version of the coating generation model is relatively simplistic, results from more detailed atomic-scale simulations will be used to advance the capabilities of the coating model to address varying process conditions. Figure 2(b) shows a snapshot from a high strain rate mechanical loading simulation conducted on the model coating microstructure.

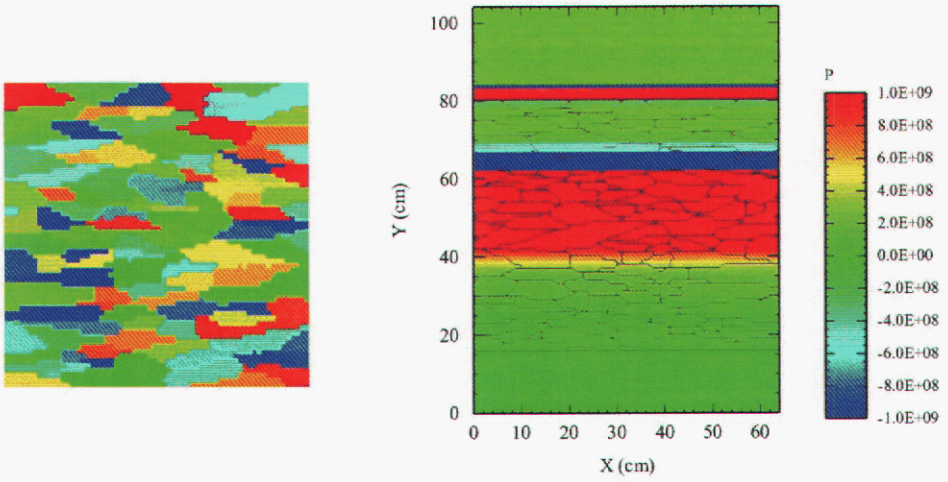

(a) (b)

Figure 2. (a) Example microstructure generated via the coating build-up model. (b) Snapshot from a high strain rate mechanical loading simulation conducted on the model coating structure.

Significance: The capability to go from highly detailed splat simulations to a realistic flame-spray coating microstructure and then to incorporate that structure into existing continuum codes for testing mechanical response has been demonstrated. This permits us to extend these capabilities to address the effect of varying process conditions on resultant microstructure and, in turn, performance. Our hope is to use these techniques to assist in process design as well as interpretation of data from performance experiments. The long-term goal is more robust performance of flame-sprayed coatings and a more deterministic set of methods for achieving this.

Contact: Edmund Webb III, Computational Materials & Molecular Sciences Dept.
Phone: (505) 284-6517
Fax: (505) 844-9781
Email: ebwebb@sandia.gov

Solid Lubricant Coatings by Atomic Layer Deposition

T. Scharf, S. Prasad, M. Dugger, T. Mayer

Motivation: Tungsten disulphide (WS_2) and molybdenum disulfide (MoS_2), which belong to the family of transition metal dichalcogenides, are well known for their solid lubricating behavior. Thin films of MoS_2 and WS_2 exhibit extremely low coefficient of friction (COF ~ 0.02 to 0.05) in dry environments, and are typically applied by sputter deposition, pulsed laser ablation, evaporation or chemical vapor deposition, which are essentially either line-of-sight or high temperature processes. With these techniques it is difficult to coat surfaces shadowed from the target, or uniformly coat sidewalls of three-dimensional or high aspect ratio structures. For applications such as micromechanical (MEMS) devices, where dimensions and separation tolerances are small, and aspect ratios are large, these traditional deposition techniques are inadequate. Atomic layer deposition (ALD) is a chemical vapor deposition technique that could overcome many of these problems by using sequential introduction of gaseous precursors and selective surface chemistry to achieve controlled growth at lower temperatures, but the chemistry needed to grow transition metal dichalcogenide films by ALD is not known.

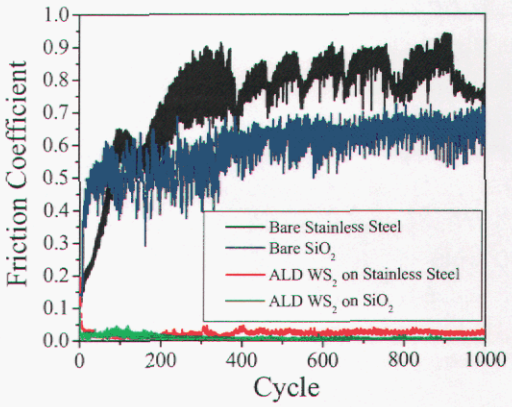

Figure 1. Friction behavior of ALD WS_2 films on SiO_2 and steel substrates. The steady state coefficients of both SiO_2 (μ=0.6) and steel (μ =0.8) are reduced to 0.008 and 0.02 as a result of ALD WS_2 coatings, respectively.

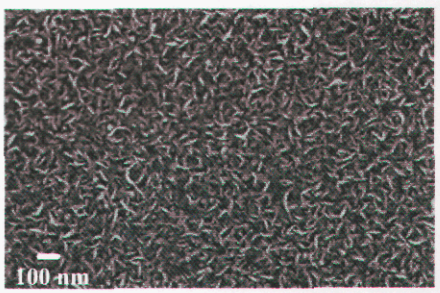

Figure 2. An SEM image of ALD WS2 film showing curved basal planes orientated perpendicular to substrate.

Accomplishment: We have developed an ALD process for the synthesis of tungsten disulphide (WS_2) solid lubricant thin films by using WF_6 and H_2S gas precursors in a viscous flow reactor at 300°C. A new catalytic route was established to promote nucleation and growth of WS_2 films on Si (or SiO_2) and stainless steel surfaces, which are the substrates used in MEMS and rolling element bearings (REB) applications, respectively. *In situ* quartz crystal microbalance (QCM) measurements showed that WS_2 did not grow on bare substrates, and thus needed a nucleating agent. We discovered that a ~3 nm layer of Zn grown by ALD served as a catalyst and facilitated the growth of ALD WS_2. This catalytic action of Zn in WS_2 growth appears to be critical for the ALD process. Raman spectra and X-ray

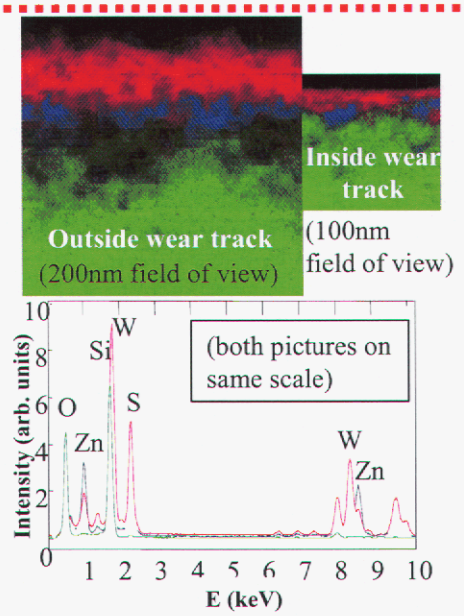

Figure 3. Cross-sectional TEM/X-ray spectral image maps of ALD WS_2 film inside and outside the wear track with corresponding elemental X-ray peaks of constituents present (green=SiO_2, blue=Zn, and red=WS_2).

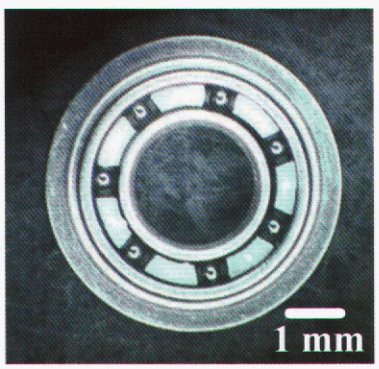

Figure 4. Optical micrograph of a fully assembled rolling element bearing (REB) coated with conformal ALD WS_2.

diffraction measurements confirmed that the WS_2 films were indeed crystalline with hexagonal (002) texture. This is typical of transition metal dichalcogenides, which exhibit easy shear basal planes necessary for low friction and wear. The films exhibited extremely low COF (0.008 - hitherto unreported for WS_2 films - to 0.02) under both low (0.6 GPa) and high (1.5 GPa) contact stresses, as seen in Fig. 1. Figure 2 shows an SEM image of a ~30 nm thick WS_2 film on SiO_2. Curved basal planes, orientated perpendicular to substrate, are seen, also typical of metal dichalcogenide film growth. In addition, X-ray spectral imaging maps were taken from a TEM image of a FIB section of the same WS2 film inside and outside the wear track (Figure 3). Some film material was removed inside the wear track as a result of material being transferred to the rubbing counterface, which is a necessary mechanism during interfacial sliding to achieve low friction and wear. This transfer film protects the underlying native film, thus providing a long wear life. Figure 4 shows a fully assembled REB coated with a conformal, ~30 nm thick ALD WS_2 film. The ALD process can uniformly coat the whole assembly, while current sputter deposition techniques can only coat the individual bearing elements.

Significance: The development of ALD solid lubricant films is expected to enable the application of low friction and low wear films to moving mechanical assemblies such as MEMS structures and REB devices with buried interfaces. The catalytic route to synthesis of these materials is a new development, which may facilitate the growth of many other metal containing films, where nucleation is impeded due to low reactivity of metal precursors.

Contact: Somuri V. Prasad, Microsystem Materials & Mechanical Behavior Dept.
Phone: (505) 844-6966
Fax: (505) 844-4816
Email: svprasa@sandia.gov

Analysis of Porosity Formation in Laser Welds

S. Viswanathan, J. Norris, R. Roach

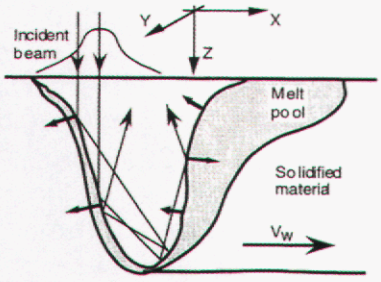

Figure 1. Schematic illustration of keyhole geometry[1] showing the path and reflections of the laser beam and fluid flow directions (velocity vectors). Vw indicates the travel direction of the laser beam.

Motivation: Current nuclear weapon component production and refurbishment requires extensive use of laser welding. Porosity in the fusion zone is a major defect that affects weld quality. Lasers can be focused to a very small spot (<1 mm), giving rise to high power densities of around 10^6 W/cm^2. As the laser beam strikes the workpiece, it quickly evaporates the substrate, and the recoil produced by the rapidly vaporizing substrate creates a "keyhole" surrounded by molten metal. The dynamics of the rapidly vaporizing substrate interacting with the complex fluid flow in the keyhole leads to instabilities and fluctuations of the keyhole geometry. The formation of root porosity in continuous wave laser welding is assumed to be due to the collapse of the liquid around the keyhole. The goal of this work was to systematically study porosity formation during laser welding, and use a combination of experiment and modeling to understand the mechanisms that control porosity formation, and use this understanding to develop welding procedures that result in defect-free welds. Figure 1[1] provides an illustration of the keyhole geometry, laser beam path, and flow patterns in a laser weld. Figure 2a shows a longitudinal view of root porosity along a weld, while Figure 2b shows a cross-sectional view through a pore.

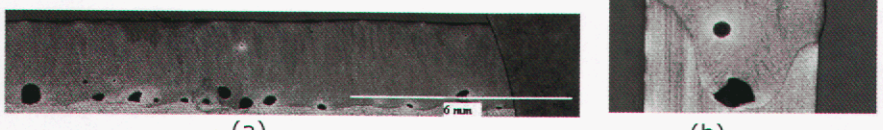

(a) (b)

Figure 2. Optical micrographs of typical root porosity in a laser weld, showing a) longitudinal cross-section, and b) vertical cross-section.

Accomplishment: An experimental plan was developed to investigate process sensitivities, phenomena and mechanisms in conjunction with diagnostic tools such as high-speed photography to capture pool dynamics. The effect of process parameters such laser power, welding speed, and gas shielding, on the level and location of porosity, was studied. Both optical metallography and microfocused x-ray radiography were used to image pores. A model of the laser welding process is being developed using the Sandia transient fluid mechanics code GOMA to further understanding of the details of the physical phenomena and mechanisms.

Key results of the experimental investigation[2] are shown in Figures 3 a and b. At high welding speeds, the porosity changed from root porosity to sporadic porosity which was smaller in size and lower in percent volume (Figure 3a). The extent and frequency of root porosity was also shown to be directly related to penetration depth (Figure 3b). Since welding speed has an inverse relation to penetration depth, it is clear that the depth of the keyhole has an important effect on the

presence of root porosity. This confirms the generally accepted notion that the formation of root porosity is related to the collapse of the keyhole. It was also shown that reduced cover gas flow reduces pore formation in the weld pool, and that welding in air nearly eliminates porosity. While this presents an interesting avenue for further study, it does not provide a solution as reducing or eliminating the cover gas creates a new set of problems such as oxidized (dirty) welds, increased spatter, and unknown effects on mechanical properties. Figure 4 shows preliminary results from the welding model that is being developed using GOMA. The model is currently able to capture the effect of the vapor recoil and the free surface dynamics. Further refinement to capture keyhole formation and collapse is ongoing.

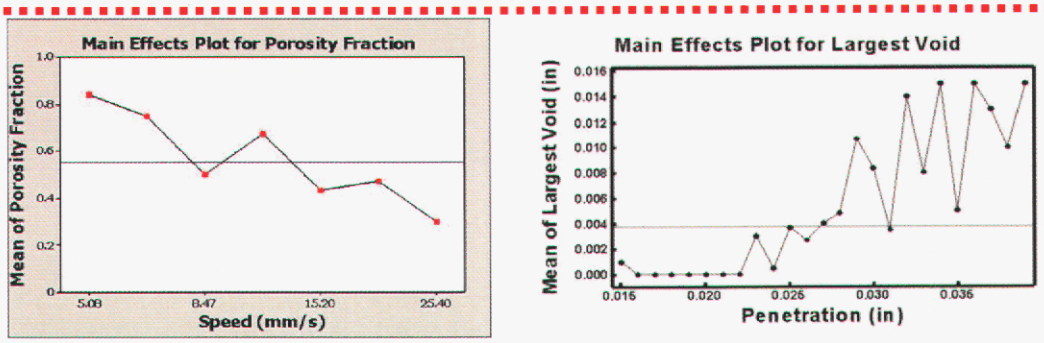

(a) (b)

Figure 3. Plots[2] showing the effect of welding parameters on porosity, in particular a) welding speed, and b) penetration depth.

Significance: Porosity in the fusion zone of laser welds is a major defect that affects weld quality. Based on systematic experimental studies of laser welds, the extent and frequency of root porosity was quantified. The results confirmed the current hypothesis that the formation of root porosity is related to the collapse of the keyhole. Preliminary results from a laser welding model indicate that the model captures the key physics of the process, and could be developed into a useful analytical and process development tool. The experimental data and model set the stage for further analysis and the development of welding procedures that result in defect-free welds.

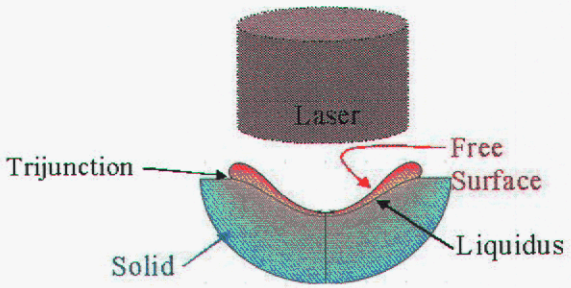

Figure 4. Preliminary results from the GOMA laser welding model showing the formation of a keyhole.

References:
1. R. Fabbro and K. Chouf, High Power Lasers in Manufacturing, Ed. X. Chen, T. Fujioka, and A. Matsunawa, Proceedings of SPIE Col 3888 (2000), p 104-112.
2. J. T. Norris, F. M. Hooper, and J. Samayoa, Unpublished Results.

Contact: Srinath Viswanathan, Joining and Coating Dept.
Phone: (505) 284-8497
Fax: (505) 845-9659
Email: srinath@sandia.gov

Application of Fundamental Materials Science and Processing to Enable Active Metal Brazing Technology

F.M. Hosking, J. Stephens, R. Loehman

Motivation: There are numerous high reliability applications were ceramic materials are joined to metal components. Active brazing alloys (ABA's) have been developed to directly fabricate these ceramic--metal braze joints. The primary technological benefit is to eliminate the costly and time consuming ceramic metallization, firing and inspection steps that are necessary when using conventional filler metal brazing techniques. Active metal brazing can substantially simplify the production process and enhance hardware reliability. The critical issue for ceramic brazing with ABA's is understanding the fundamental principles and mechanisms that control the ceramic-braze interfacial reactions, microstructures, and braze joint properties. Fundamental materials science is needed to assure and qualify the technology for use in manufacturing hermetic, high strength seals and feedthroughs. Research at Sandia has focused on developing the fundamental analytical and experimental tools to predict and correlate properties and braze joint performance to materials and processing conditions.

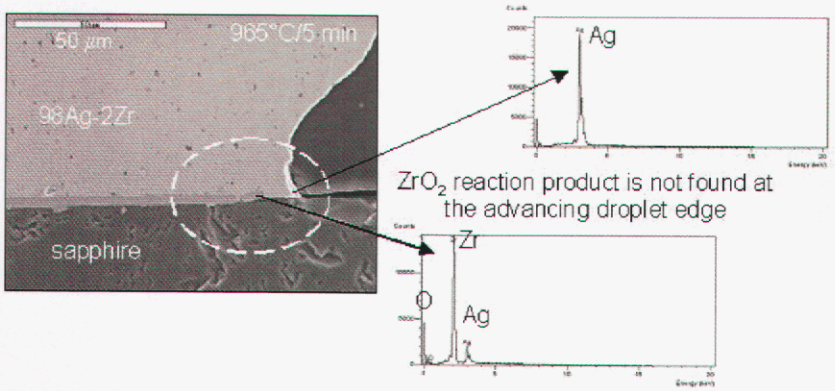

Figure 1. Leading edge of 98Ag-2Zr (wt. %) active filler metal on sapphire with no evidence of zirconia reaction product near the braze-sapphire free surface. Note energy dispersive spectroscopy (EDS) differences between the two interface regions.

Accomplishment: Different dilute additions of "active" elements (V, Ti, Zr, and Hf) to conventional Au and Ag-based filler metals were studied. The degree of brazing reactivity and wetting on alumina ceramic was found to increase with increasing thermodynamic oxide reactant stability. Base metal dissolution and potential "scavenging" or depletion of the active element by these complex brazing reactions can limit the formation of a continuous, hermetic reaction layer between the ceramic and braze. The issue of brazing atmosphere can also effect braze flow behavior and structural voids within the braze. Experimental results have revealed the first evidence of the lag in development of the oxide reaction product at the leading edge of the advancing liquid braze (see Figure 1). Understanding this spreading mechanism will be critical in controlling and optimizing interfacial adhesion and related braze joint properties.

Interfacial relationships between the analytical and experimental data for ABA-brazed polycrystalline alumina reveal that the resulting mechanical properties are

very sensitive to the reaction product type, its morphology and actual braze fill or coverage. The effect of entrapped braze voids and porosity on flexure strengths for the Ag-Zr and Ag-Hf filler metals is particularly critical (see Figure 2 for the 98Ag-2Zr and 96.6Ag-3.4Hf ABA's). As joint porosity increased, strength values intuitively and experimentally decreased. Improving braze flow behavior and fill, therefore, reduces or eliminates these potentially detrimental internal defects and increases braze joint hermeticity and strength. Brazing under vacuum or partial pressure conditions (i.e., creating a pressure differential at the liquid braze free surface) provides the effective means to prevent unwanted leak paths and enhance joint performance and reliability.

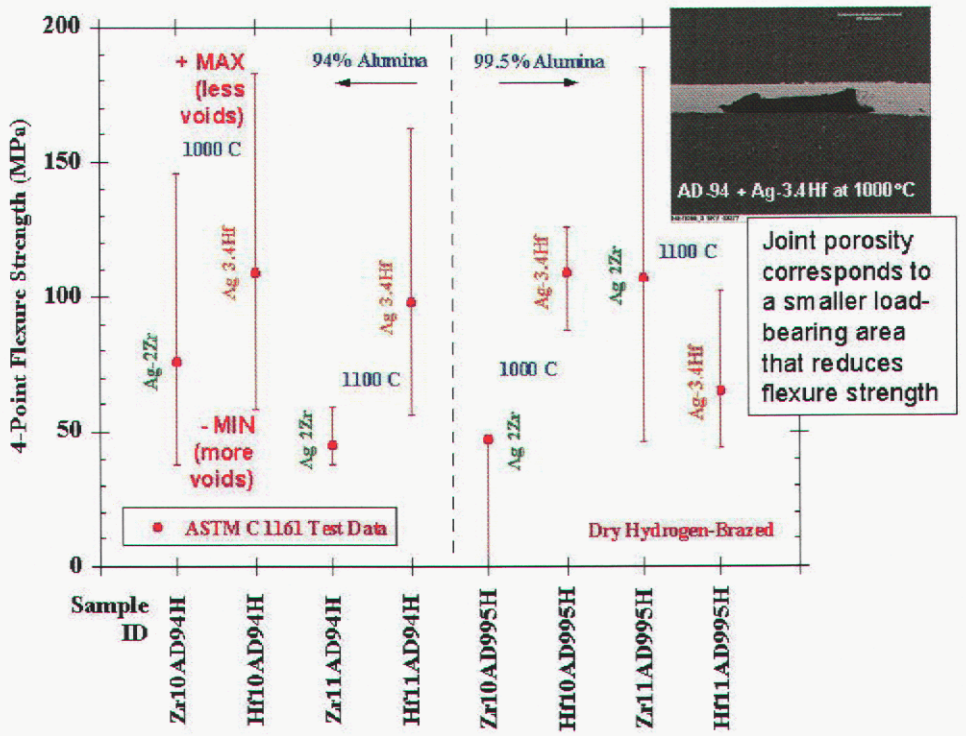

Figure 2. Internal voids contribute to highly variable flexure strengths for Ag-Zr and Ag-Hf brazed alumina four-point bend test specimens (error bars represent maximum and minimum values around average strengths).

Significance: Sandia's ABA research is internationally recognized for its technical achievements and contributions to the understanding and advancement of the fundamental science and technology of ceramic-metal brazing. The interdisciplinary research approach provides the fundamental understanding for enabling a critical joining technology, establishing the foundation to investigate other ceramic-metal interfacial reaction systems, and providing new research opportunities.

Contact: F. Michael Hosking, Joining & Coating Dept.
Phone: (505) 845-8401
FAX: (505) 844-4816
Email: fmhoski@sandia.gov

Development and Application of Silver-Zirconium and Silver-Hafnium Active Braze Alloys

J. Stephens, F. M. Hosking, C. Walker, F. Yost

Motivation: Various Sandia components used for high reliability applications would like to use active metal braze alloys for hermetic Kovar™/alumina ceramic braze joints. However, the main commercial Ag-Cu-Ti active braze alloy (Cusil ABA) produces mediocre yields for this type of braze joint, due to "scavenging" of the Ti active element by Fe, Ni and Co that has dissolved into the braze joint during braze processing. The scavenging reactions cause reduced Ti at the ceramic interface, resulting in poor hermetic yields. Active filler metals with greater thermodynamic tendency to wet the alumina ceramic were deemed desirable. Finally, a desire to simplify the number of piece parts used in brazed assemblies led to the need for active filler metals with a greater tendency to creep and stress relax during cooldown from the brazing temperature – in order to help minimize residual stresses in the brazed metal/ceramic assemblies.

Accomplishment: The goal was to develop an active filler metal for Kovar/alumina ceramic braze joints that was not subject to the "scavenging" reactions suffered by the Ag-Cu-Ti alloy, combined with the important attribute of low elevated temperature mechanical strength. This filler metal would have improved ability to minimize residual stresses in the brazed metal/ceramic assembly. Two compositions (in wt.%) were developed: (a) 98Ag-2Zr, and (b) 96.6Ag-3.4Hf.

These active filler metals are evaluated using ASTM F19 ceramic tensile button samples, as shown in Figure 1. Note first that the hermetic yields for both 98Ag-2Zr and 96.6Ag-3.4Hf filler metals are substantially better than the yields obtained with the Cusil ABA filler metal. Second, the average strength of the Cusil ABA buttons is less than half that of the other two filler metals. Many of the tensile button samples brazed with 98Ag-2Zr or 96.6Ag-3.4Hf filler metals underwent bulk ceramic fracture, a significant distance away from the braze joint.

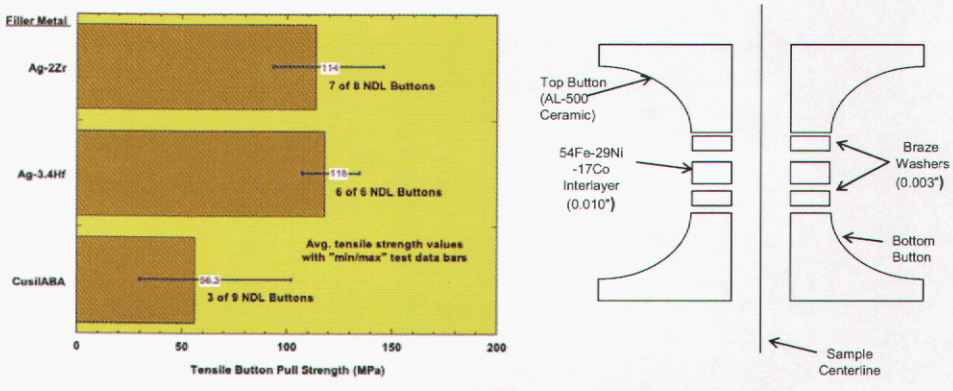

Figure 1. A sketch of the tensile button sample material stackup, combined with a summary bar chart of the results obtained with tensile buttons samples brazed with filler metals 98Ag-2Zr, 96.6Ag-3.4Hf, and Cusil ABA. All buttons used 0.003 inch braze performs, a 0.010 inch thick Kovar interlayer, and air fired WESGO AL-500 grade ceramic. "NDL" means no detectable leak, verified by a helium leak check apparatus with sensitivity of at least 1E-9 atm-cc/sec.

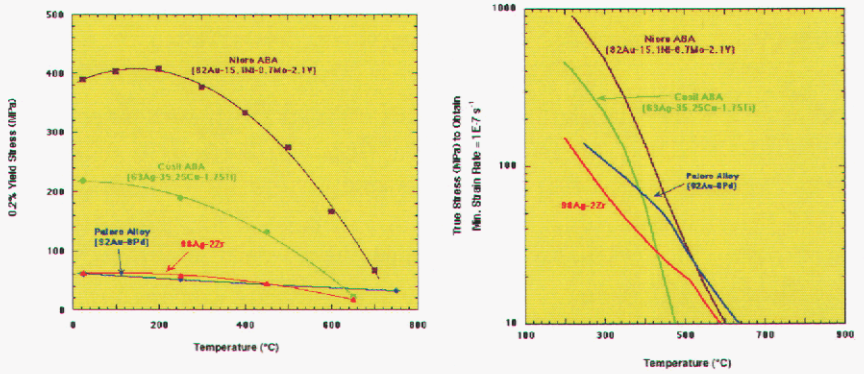

Figure 2. (A) Yield stress as a function of temperature for 4 different filler metals. (B) Stress required for a minimum strain rate of 1E-7 s^{-1}, calculated from minimum creep rate correlations. The large increase in this stress value at lower temperatures is consistent with the creep deformation phenomenon known as "power law breakdown."

These observations indicate that excellent strength is obtained at the braze/ceramic interface for both filler metals.

The success of the 98Ag-2Zr and 96.6Ag-3.4Hf alloys in reducing residual stresses in metal/ceramic braze joints can be illustrated in generic form by comparing their elevated temperature properties to those of other active filler metals. (Due to their similar microstructures, the 96.6Ag-3.4Hf metal is assumed to have mechanical properties identical to that of the 98Ag-2Zr alloy.) Figure 2A shows a comparison of 0.2% yield stress as a function of temperature for 98Ag-2Zr and three other filler metals. The yield strength of both Nioro ABA and Cusil ABA are significantly higher than those of either 98Ag-2Zr or the Paloro alloy. In fact, the high strengths of the 2 former filler metals suggest that they can be used only in braze joint geometries where somewhat high residual stresses can be tolerated. We also compare the stress required to obtain a minimum (creep) strain rate of 1E-7 s^{-1}. This is plotted in Figure 2B. The ranking of these four alloys at 250-300°C is identical to the ranking one could obtain from the yield stress data in Figure 2A. Thermal mismatch strains in Kovar/alumina ceramic braze joints peak at ~400°C, which fortunately is in the regime where creep kinetics are still reasonable for filler metals such as 98Ag-2Zr and Paloro.

Significance: The development of these active filler metals has been critical for the realization of advanced component subassembly designs with reduced parts and no backup rings. In large part, the requirements for filler metals used for metal/ceramic brazing are fundamentally different than those used for metal to metal braze joints. This is due to the need for braze alloys with relatively easy creep and stress relaxation properties to avoid inducing residual stress levels in the ceramic that could lead to cracking and loss of hermeticity.

* Kovar is a registered tradename of Carpenter Technology Corporation, Reading, PA

Contact: John J. Stephens, Materials Reliability Dept.
Phone: (505) 845-9209
Fax: (505) 844-4816
Email: jjsteph@sandia.gov

New Approaches to Microjoining

G. Knorovsky, C. Robino, J. Michael, E. Holm

Motivation: Sandia is committed to MESA (Microsystems and Engineering Sciences Applications) to provide microsystem-based components for the enduring stockpile. Such microsystems may include emerging technologies like LIGA (ultra-precision electroforming), MEMS (micro-electro-mechanical systems), photonics, microfluidics, and microelectronics. Integration of multiple technologies into complete systems poses challenging problems to reliably align, join, and co-package disparate materials (metals, poly/single crystal Si, compound semiconductors, polymers). The mm-to-cm size scales of contemporary weapon components are expected to shrink by orders of magnitude, rendering current fabrication methods marginal at best. Laser welding, the current process-of-choice for welding small parts, is restricted by the ability to focus light to a small spot. The focal spot of typical small component laser welders is about 200 μm diameter, though special effort can reduce this by about an order of magnitude. Clearly, this will not be suitable for joining features smaller than the beam. As the surface-to-volume ratio becomes larger, a more fundamental problem is that it becomes progressively harder to melt without increasing the laser beam intensity to values which normally result in drilling. Thus, we are investigating joining processes characterized by flexibility with respect to material, suitable visualization capability, and small size capability. A key issue is surface tension, which increasingly affects the behavior of molten material at smaller size scales. The processes under study are: 1) micro-beam laser welding, 2) micro-electron beam welding, and 3) focused particle beam deposition joining.

Accomplishment: The transition from melting to drilling as the focal spot become smaller is a concern for both laser and e-beam processes. Experimental work with finely-focused laser beams showed that it is possible to obtain very small fusion zones (<50 μm diameter) without drilling (see Figure 1). Improved models also verified that surface tension effects are crucial to understanding the melting-drilling transition. Further, the model suggested that pulse lengths shorter than the usual few ms would help avoid drilling. Work with a Q-switched laser (~100 ns pulses,) verified that we could obtain very small fusion zones. Another concern with laser processing is that it is increasingly difficult to see small parts with conventional laser optics due to decreasing depth of focus at higher magnification.

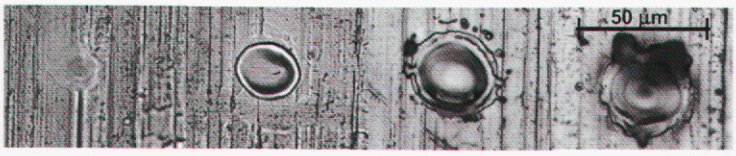

Figure 1: Laser-produced molten zones made with increasing beam energy: a) to b) shows conduction-to-keyhole transition (34 to 48 mJ); c) to d) shows keyhole-to-drilled transition (70 to 110 mJ). All results are for 5ms pulses with 40 μm focused beam diameter.

The scanning electron microscope (SEM), with a beam that can be focused to a few nanometers diameter, is inherently an ideal visualization tool, with both high magnification and good depth of focus. A standard SEM can be converted into a micro-electron beam

welder re-adjusting the focusing lens current and removing an aperture to increase the beam current from a few nA to approximately 10 mA. This provides sufficient energy to melt small specimens. SEM beam-melted specimens are shown in Figure 2. By rastering the beam over a selected area, the average intensity can be carefully controlled, which allows fine control of the magnitude of melting, as evidenced by the weld vs. rivet geometries shown in Figure 2c. The minimum SEM effective beam size is given by the interaction volume of the electrons with the material. At several tens of kV, this volume is ~1 μm^3. It may be possible to melt even smaller volumes by suitably adjusting acceleration voltage and beam current.

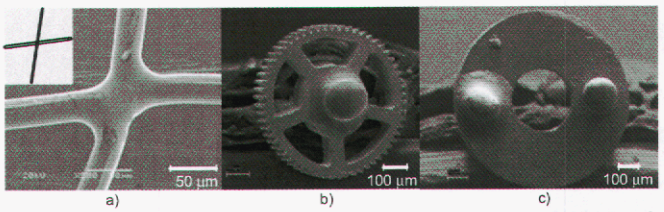

Figure 2: Examples of welds accomplished in an SEM: a) Tophet C crosswire weld; b) LIGA Ni gear to steel shaft, c) LIGA Ni shaft as weld and as rivet, demonstrating that the degree of melting can be varied by energy control.

In focused particle beam deposition joining, an ion or electron beam "cracks" an organo-metallic gas, which has been adsorbed upon the surface where deposition is desired. This process relies upon atomic-level adhesion of activated molecules to provide "filler material" to form a joint without melting. Hence, the melting-to-drilling issue noted earlier is not a concern. Indeed, it has been demonstrated that material can be successfully deposited on the scale of a few hundred nm. Beam energy is low, so imaging capabilities are excellent. Typical joints are shown in Figure 3. While this process is very suitable for submicron features, it is relatively slow, so it does not scale up well to larger features. In addition to the process speed concern, the deposits are somewhat brittle, because the cracked molecule deposits hydrocarbon as well as metal, and in the case of the ion beam process (which is faster than the electron beam variant), the ions (typically Ga) are also present at a significant level in the deposited material.

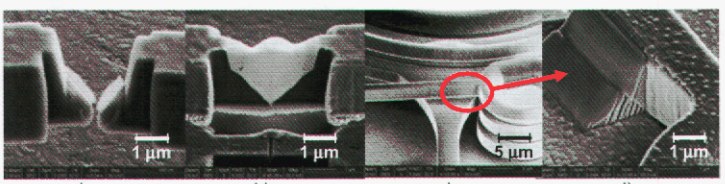

Figure 3: Shows two types of joints before and after focused particle beam deposition joining: a and b, beveled butt joint; c and d, lap joint (note that d is rotated ~90° clockwise relative to c).

Significance: Several processes are being investigated to provide joining capabilities anticipated to be needed for MESA-inspired microsystems at size scales below present capabilities. Feasibility has been shown for micro-beam laser joining, micro-electron beam welding (in conventional SEM systems) and focused particle beam deposition joining. Process and joint characterization activities are ongoing.

Contact: Gerald Knorovsky, Joining & Coating Dept.
Phone: (505) 844-1129
FAX: (505) 845-9659
Email: gaknoro@sandia.gov

Reliable Seals for Solid Oxide Fuel Cells (SOFC)

R. Loehman, M. Brochu, R. Tandon, T. Garino, B. Gauntt

Motivation: Lack of reliable sealing techniques has been identified as one of the most significant barriers to commercializing planar solid oxide fuel cells. Development of reliable methods for sealing solid oxide fuel cell stacks presents the most challenging set of performance criteria in the entire field of ceramic joining. For SOFC applications, the requirements on the sealing method include: 1) adhesion of the sealing material to fuel cell components from room temperature to as high as 1000°C, 2) provide a leak-tight seal at the SOFC operating temperature, 3) ability to maintain a seal while accommodating strains from SOFC components with different CTEs, 4) lack of adverse reaction between the sealing material(s) and the fuel cell components, 5) chemical and physical stability of the sealant at temperatures up to 1000°C in oxidizing and reducing atmospheres, 6) thermal shock tolerance, and 7) electrically insulating for some SOFC designs.

All of the above properties must be maintained for SOFC operating lifetimes of up to 40,000 hours. Under DOE sponsorship this project is developing an approach to sealing SOFCs that can be tailored to the specific requirements of industrial teams participating in the DOE/SECA program. In our judgment relief of thermal expansion mismatch stresses will require SOFC seals to incorporate either a ductile metal or a high viscosity glass that can relieve stresses through viscous creep. Other design and operational constraints on SOFCs, which frequently are in opposition, severely restrict the options for seal materials. Based on our prior experience in ceramic joining and on results obtained so far on this project, we believe we have greatest design flexibility using ceramic filled glasses and metal filled glass composites

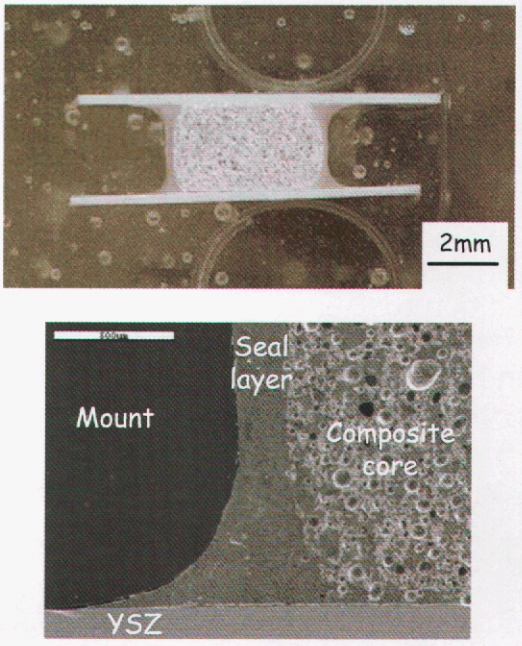

Figure 1: Micrographs of a seal to YSZ that comprises a composite layer with 70 vol% YSZ powder and 30 vol% of one of our sealing glasses bonded with a thin layer of the same glass. The composite CTE has been adjusted to 10.2 x 10–6/°C. The seal adheres tightly to the YSZ and survived multiple thermal cycles up to 850°C

Accomplishment: We can control properties such as glass transition temperature and thermal expansion coefficient by varying the compositions, amounts, and microstructures of the different phases. The choices are guided by thermochemical and composite microstructural models that allow us to target specific seal properties for a given design. We developed and tested over 30 glass compositions with different glass

transition temperatures and expansion coefficients. We used those glasses to make glass-ceramic powder composites by varying glass and additive compositions and volume fraction of powder additive and demonstrated that we can vary CTE in a controlled manner. We sealed a variety of composites to yttria-stabilized zirconia (YSZ) electrolytes and demonstrated good adhesion and mechanical strength. Thermal cycling tests showed these composite seals are resistant to damage from thermal cycling. Seal tests at 800-850°C for up to 200 hours showed adhesion is maintained. Figure 1 shows several micrographs of a seal to YSZ that comprises a composite layer with 70 vol% YSZ powder and 30 vol% of one of our sealing glasses bonded with a thin layer of the same glass. The composite CTE has been adjusted to 10.2 x 10−6/°C. The seal adheres tightly to the YSZ and survived multiple thermal cycles up to 850°C. Availability of manufacturing processes is always an issue in materials joining. Figure 2 illustrates some experiments that show that glass-ceramic composite seals can be formed using preforms that are tapecast using techniques common to microelectronic packaging. The green (unfired) tape can be cut to the shape required for the bond area and stacked so that the whole assembly is sealed and otherwise processed in a co-fire operation.

Type of cast	Additive / vol%	Vol% Solid
Pure glass	N/A	65%
Glass-ceramic composite	14a / 30vol%	65%
Glass-metal composite	Ni / 30vol%	65%

Typical volume% solid of common tape cast is around 55-65%

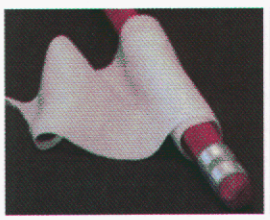

Figure 2: Glass-ceramic composite seals can be formed using preforms that are tapecast using techniques common to microelectronic packaging. The green (unfired) tape can be cut to the shape required for the bond area and stacked so that the whole assembly is sealed and otherwise processed in a co-fire operation.

Significance: We have demonstrated the potential of the glass-powder composite approach for sealing SOFCs. We have shown that we can independently vary compositions and microstructures to achieve desired seal properties and that those properties can be targeted to seal different SOFC materials. We have demonstrated a number of techniques for applying the seals that would be practical in a manufacturing setting.

Contact: Ron Loehman, Ceramic Processing & Inorganic Materials Dept.
Phone: (505) 272-7601
Fax: (505) 272-7304
Email: loehman@sandia.gov

Dynamic, Model-Based Electroslag Remelting Process Control

D. Melgaard, G. Shelmidine

Motivation: The electroslag remelting (ESR) process is used extensively to produce clean, fully dense ingots of high quality steel and nickel based superalloys with applications throughout the aerospace industry. Due to the critical nature of these applications, the quality standards for these materials are becoming more stringent. Adequate control requires minimizing the deviations in two coupled parameters, melting rate and immersion depth. These parameters impact the solidification structure, homogeneity and surface quality. Present day controllers treat them independently, resulting in greater variability in the process and poorer quality material. More importantly because of the inherent noise in the process, these controllers are highly damped, making them particularly inept at handling excursions from steady state.

Accomplishment: During ESR, a metal electrode is melted by immersing it into a molten slag bath which has been resistively heated above the melting temperature of the metal. The electrode melts, coalescing into droplets which eventually fall through the slag and collect in a molten metal pools below the slag in a water cooled mold. As shown in Figure 1, our model-based control combines the results of a physical model of the ESR with feedback from the measurements taken during melting. Kalman filtering techniques are employed, which use the uncertainty of the model and measurements to weight the combination optimally. This combination results in the estimation of ten state variables that are used to identify the instantaneous and simultaneous depth and melt rate. Control is achieved by applying appropriate time constants for the system response to set the control signal gains to correct the deviations from the set points. In addition, we developed a technique for identifying the immersion depth. For high surface quality, the depth should be approximately 5mm, which is difficult since the electrode tips often have variations of that magnitude. Since no method has been identified to measure the depth, other controllers infer that constant voltage variance implies a constant depth with no knowledge of the actual depth. By identifying unique patterns in the electrical signals during melting, we

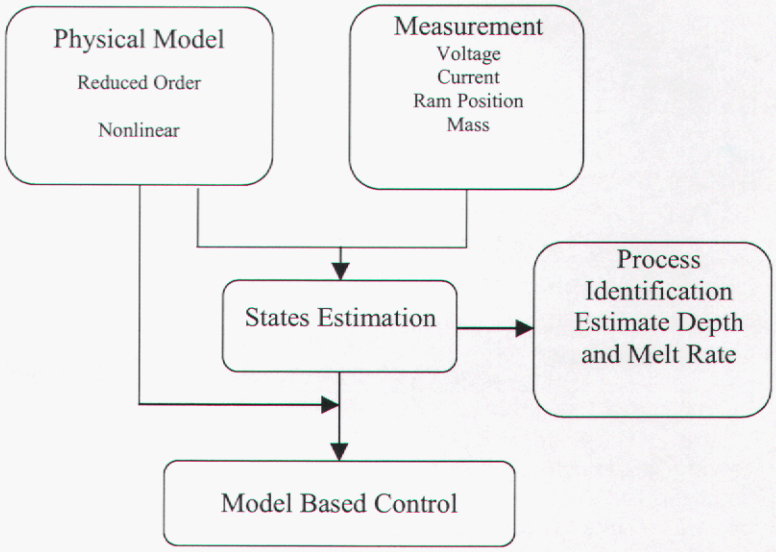

Figure 1. Schematic of Model Based Control

were able to determine the true depth and thereby decrease the variation in the process. The new controller has been extensively tested on a laboratory scale furnace here at Sandia and at a number of industrial sites. The melting rates have been significantly improved and a marked improvement in surface quality has been observed. The success has been even more striking during process upsets. An example of this is given in Figure 2. It shows the melt rates for the present-day and the model-based controllers while going through a crack in an electrode. Not only was the deviation greater with the other controller, but control was restored back to the original level much more quickly with the new controller.

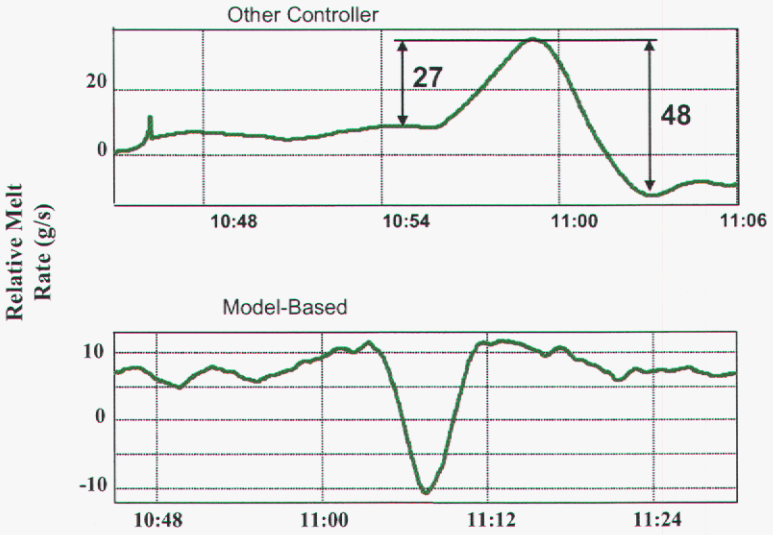

Figure 2: Comparison of melting rate control between present-day controller on top and the model based controller on the bottom.

Significance: This technique of combining a model of a process with measurements for feedback has been successfully applied in a number of applications and will no doubt be successfully utilized on other processes in the future. The new controller has been demonstrated to operate at a more consistent immersion depth, resulting in improved surface quality of ESR ingots and with a more uniform melting rate. Since perturbations or transients in the process may initiate solidification defects, the homogeneity of the grain structure in the resulting ingots will be improved as well. The controller shows promise in meeting the higher standards for materials for the future.

Contact: David Melgaard, Biomolecular & Chemical Analysis Dept.
Phone: (505) 844-1022
Fax: (505) 294-3020
Email: dmelga@sandia.gov

Furnace Air Leak Monitoring to Reduce Ingot Defects in Vacuum Arc Remelting of Titanium

J. Van Den Avyle, R. Williamson

Motivation: The goal of this project is to improve the quality of titanium alloys used in critical rotating components of aircraft engines through enhancements in melting technology and diagnostics. The objective is to prevent or remove melt related defects. Currently, advanced titanium melt processing utilizes a combination of either the electron beam cold hearth melting (EBCHM) or the plasma arc hearth melting (PAM) process plus vacuum arc remelting (VAR). All rotating-grade titanium alloy product utilizes VAR as a final remelting process. One concern with the final VAR melt step is that furnace air leaks could lead to formation of titanium nitride or oxide on hot solid titanium surfaces within the furnace. Due to their elevated melting temperatures, these compounds may not dissolve if they fall into the molten titanium, resulting in "hard alpha" defects. A possible location for this gas-metal reaction is the solid "crown" material deposited within a few inches above the molten titanium pool on top of the growing ingot. The crown is made up of metal droplet splatter from the arc as well as condensed metal vapor, and can be enriched in higher vapor pressure alloy constituents, such as aluminum (Figure 1).

Total furnace atmosphere pressures are currently monitored throughout the VAR melts using standard vacuum gauges. Previous work in this project has shown that small leaks may not be detected using the standard gauges, but can be detected with high sensitivity using a residual gas analyzer (RGA).

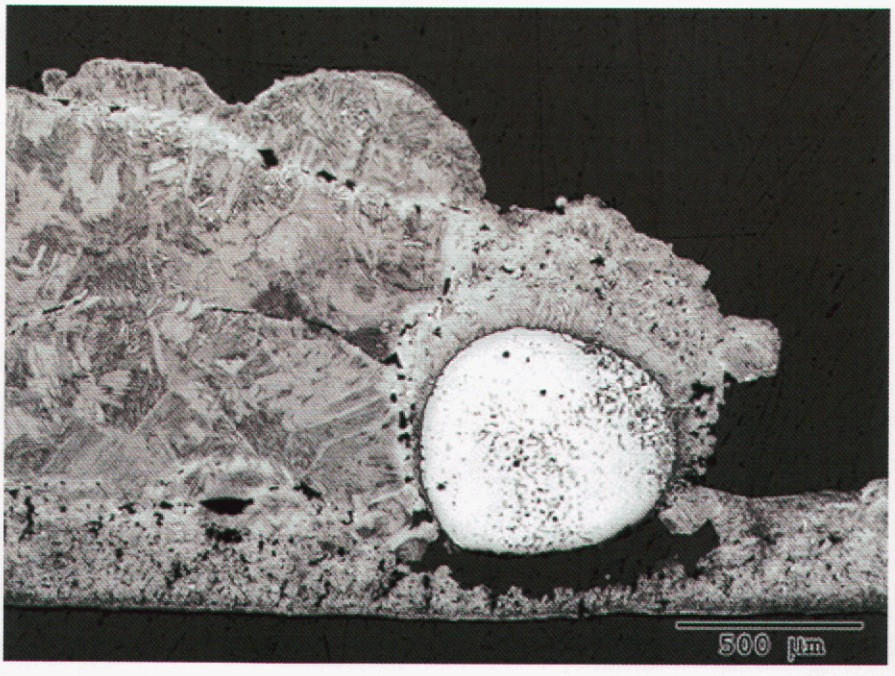

Figure 1. SEM image of cross-section of titanium VAR crown material exposed to an air leak of 230 sccm in the Sandia furnace.

Accomplishment: Four short laboratory VAR experiments were run at Sandia to assess the levels of furnace atmosphere oxygen and nitrogen sufficient to cause significant reaction with exposed crown material to produce hard alpha. Air leak rates selected for these experiments bracketed RGA furnace atmosphere measurements taken during a full-scale industrial trial with calibrated leaks. Samples of the contaminated ingot crown were chemically and metallographically analyzed for evidence of hard alpha material. Mounted and polished cross-sections of crown material samples were evaluated by electron microprobe and SEM, looking for localized areas of high nitrogen or oxygen content resulting from the air leaks. No high local concentrations were found. LECO bulk chemical analysis indicated that the higher air leak rates did cause elevated average oxygen and nitrogen adsorption by the crown material, at concentrations sufficient for alpha phase survival in the ingot.

A major goal has been to install an RGA monitoring system on an industrial titanium VAR furnace and use it to monitor furnace gas atmospheres during a large number of production melts. These measurements provide data on typical levels of oxygen, nitrogen, and water vapor from melt to melt, evidence of non-typical air or water leaks, and provide needed industrial experience with use of RGA monitoring. A new RGA software interface has been developed and tested at Sandia; it provides continuous collection and storage of furnace gas partial pressure data in an industrial environment. The system was installed on a final melt VAR furnace at Timet Corporation, Henderson, NV and has collected around-the-clock data for over 4 months.

The RGA system continuously logs and displays output from two vacuum gauges as well as furnace gas partial pressures, opening and saving new data files at a selected interval (currently every 24 hr). This arrangement allows the RGA to operate totally independent from the furnace and does not require staff to start and stop data logging with each melt.

Significance: Development of advanced furnace diagnostic techniques provides new tools for improved process control. They help reduce melt-to-melt variability and give indications of process upsets that can cause defects or lower alloy quality. Long-term industrial testing of the RGA furnace atmosphere monitor has shown that high resolution measurements can be collected in a demanding industrial environment. This diagnostic tool can be used by Sandia's industrial partners in the Specialty Metals Processing Consortium to improve their process controls and the quality of ingots and castings.

Contact: J. A. Van Den Avyle, Materials Characterization Dept.
Phone: (505) 284-8499
Fax: (505) 844-2974
E-mail: javande@sandia.gov

Elimination of Flammable, RCRA, and ODC Solvents for Wipe Application

E. Lopez

Motivation: Due to worker safety and flammability concerns, efforts have been made within the nuclear weapons complex of the National Nuclear Security Administration (NNSA) of the Department of Energy (DOE) to replace Resource Conservation and Recovery Act (RCRA) regulated solvents (i.e., flammable, toxic, corrosive, and reactive) and ozone-depleting chemicals (ODC) with environmentally responsible alternatives. Historically, these solvents have been used for cleaning hardware during routine maintenance operations. The primary goal is to systematically reduce flammable solvents (principally isopropyl alcohol) used in proximity to and in nuclear assembly/disassembly operations consistent with a risk-cost benefit assessment of solvent and combustible material elimination, minimization or substitution. Candidate cleaning solutions being evaluated as replacements for isopropyl alcohol (IPA) include a neat hydrofluoroether (HFE) and a HFE/IPA azeotrope. Cleaning efficacy, materials compatibility (including cleaner corrosivity), drying times, flammability, ES&H requirements and accelerated aging behavior are among the criteria used to screen candidate solvents.

Accomplishment: Cleaning results indicate that the neat HFE is not as effective as IPA for removing representative contaminants (silicone grease, Krytox grease, dust sebum emulsion-simulated fingerprint), whereas the HFE azeotrope appears to be roughly equivalent to IPA in cleaning performance. These conclusions were based on the results from several analytical methods including a contact angle/goniometer, MESERAN (Measurement and Evaluation of Surfaces by Evaporative Rate ANalysis), which measures organic contamination down to nanogram/cm^2 levels, and x-ray photoelectron spectroscopy. MESERAN test results for the removal of Krytox grease from 2024 aluminum are depicted in Figure 1. The results indicate an average slope value of 2690 after cleaning with IPA, which corresponds to an average equivalent contamination level of 38 ng/cm^2. When cleaned with the HFE solvent, a contamination level of 5743 ng/cm^2 was obtained, and a contamination level of 45 ng/cm^2 was obtained after cleaning with the HFE

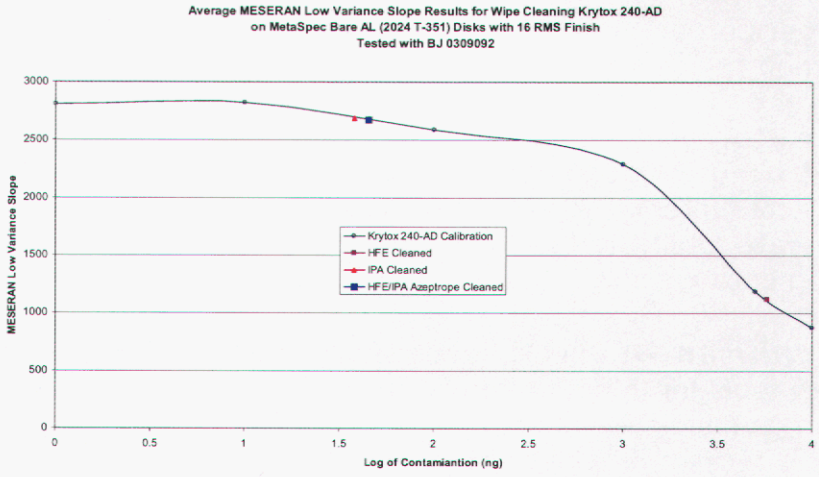

Figure 1 - MESERAN Test Results – Krytox A-D on Bare Al 2024

azeotrope. The same general cleaning trends were observed for the removal of silicone grease and dust sebum emulsion.

Compatibility between solvents and metal alloys was assessed with the Sandwich Corrosion Test per ASTM F1110-90, and the Immersion Corrosion Test per ASTM F483-98. No significant materials compatibility issues were identified for either of the candidate cleaners (Figure 2). Other results indicated no deleterious effects to polymeric materials immersed in either the IPA or the HFE solvent: high explosives compatibility using differential scanning calorimetry and chemical reactivity tests showed no reactions with either the IPA or HFE to the various explosives. Similarly, no cure inhibition reactions were noted for HFE on any of the adhesives or potting compounds. An 8 hour time weighted average (TWA) for HFE is well below the detection limit for wiping applications. Therefore, the exposure of personnel to HFE vapors during any wiping or rubbing application is not anticipated to be a worker safety issue. A formal ES&H determination is needed to confirm this finding. Long-term experiments are currently in progress.

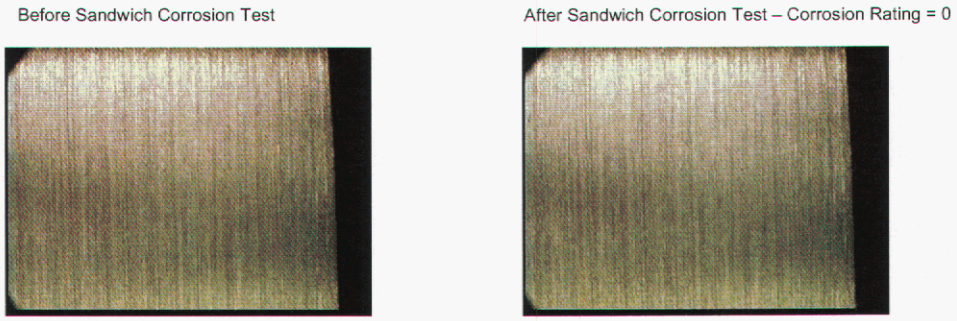

Figure 2 – Sandwich Corrosion Test Bare 7075 Aluminum – HFE Exposure

Significance: The cost benefits to all programs at BWXT Pantex Plant from removing a flammable solvent, such as isopropyl alcohol, would include (1) the savings of significant process time if the requirements for task exhaust, bonding and dry times were lifted due to the use of nonflammable solvents, (2) other operational efficiencies, such as the use of facilities that are not currently available for weapons work due to the absence of task exhaust, could be optimized if the requirement was removed, (3) waste disposal costs could be reduced for both the NNSA/BWXT Pantex Plant and the DoD since the waste generated has the potential of being categorized as non-hazardous or mixed, and most importantly (4) safety would be greatly enhanced, i.e., the elimination of flammable solvents would remove the fuel component necessary to support a fire.

Contact: Eddie Lopez, Corrosion and Electrochemical Sciences Dept.
Phone: (505) 845-9181
Fax: (505) 844-9624
Email: eplopez@sandia.gov

Liquid-Solid Transition in Molten Tin under Dynamic Compression

S. Foiles, J. Davis

Motivation: The dynamic behavior of materials under extreme conditions is of general interest to the stockpile stewardship program. Due to the higher density of most solids relative to their liquid, the application of high pressure can drive the freezing of liquids by moving the system into the solid portion of the phase diagram. This phenomenon has received very little experimental study especially in the molten metals. In order to achieve the needed pressures, it had been necessary to perform shock experiments. However, the heating along the shock Hugoniot keeps the system in the molten state. Recently, Sandia's pulsed power efforts have developed the capability to use the Z-machine to perform isentropic compressions of materials by ramping the pressure waves so as to avoid the creation of a shock front. Since the temperature rise on the isentrope is much less than on the Hugoniot, it is now possible to experimentally study the dynamic freezing of molten metals under compression. The first experiments are being performed with tin. A computational study of the properties of molten under high pressure is being pursued to provide equation of state information needed for the analysis of the experiment. In addition, the kinetics of the simulation process are being computed to compare with the time scales of the experiments.

Accomplishment: The equilibrium properties of molten tin as a function of temperature and pressure have been computed using ab initio molecular dynamics. In these calculations, the energy and forces are determined from density functional theory calculations of the electronic structure and classical molecular dynamics is used to determine the thermodynamic averages. These calculations provide information about the equation of state as well as the internal structure in the liquid. The reliability of the calculations has been assessed by comparison of the results obtained for zero pressure with known experimental thermodynamic and structural in formation. In Figure 1, the computed structure factor for molten tin near its zero pressure melting point is compared to experimental result from x-ray scattering. The excellent agreement provides confidence in the predictive reliability of the calculations.

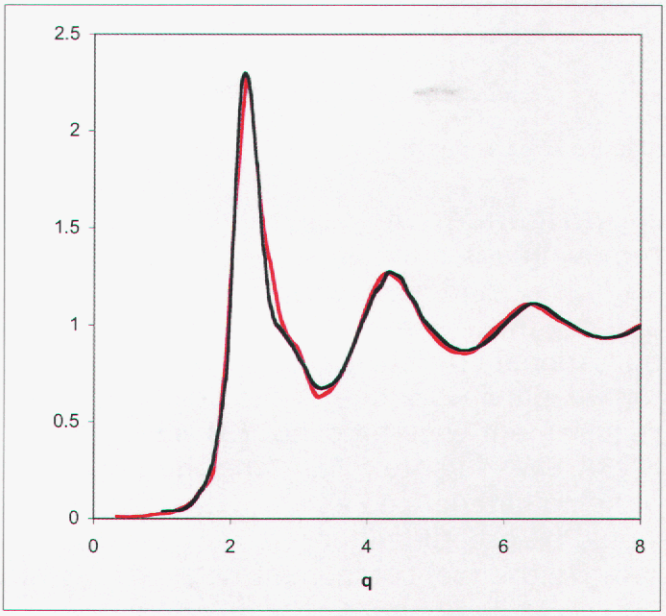

Figure 1. Comparison of the static structure factor of molten tin computed by ab initio molecular dynamics (red) with x-ray scattering experiments (black).

The *ab initio* molecular dynamics are too computationally intensive to study the kinetics of solidification. Therefore a novel interatomic potential for molten tin has been developed which combines approaches for metallic and semiconductor systems. This is required since the bonding in tin is borderline between these two materials classes as can be seen by noting that the element above it in the periodic table is the semiconductor germanium and the element below it is the fcc metal, lead. Comparing the liquid structure factors calculated for the temperatures and pressures of interest with those obtained from the *ab initio* molecular dynamics validates the quality of this new potential. These potentials are being used with molecular dynamics to study the kinetics of the solidification process at high pressures. Figure 2 shows initial and final states of such a simulation at 5 GPa and 650 K. The rate of advance of the solid phase (red) into the liquid phase (green) has been determined for a range of temperature and pressures relative to the coexistence curve.

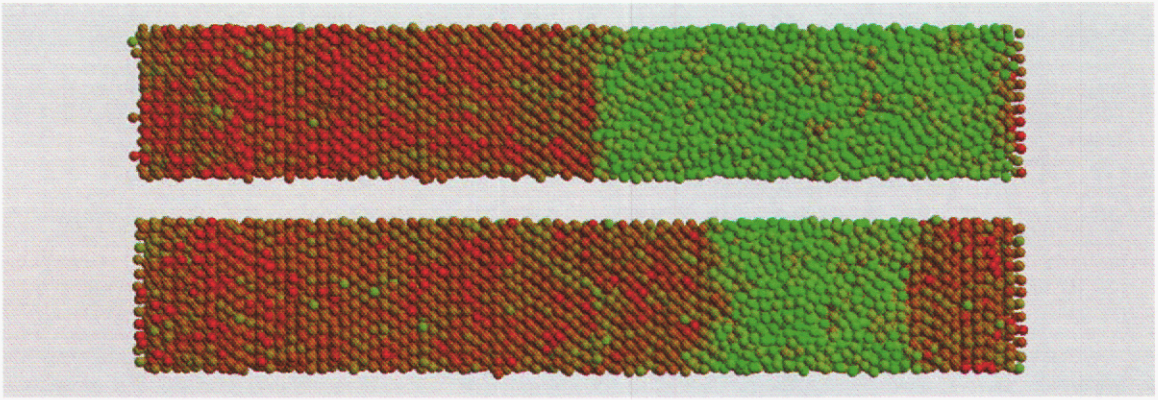

Figure 2. Snapshots of molecular dynamics simulations of the kinetics of solidification of molten Tin. The coloring reflects a measure of local liquid (green) or solid (red) structure.

Significance: Computational modeling is being used to complement a novel experimental capability to enhance the understanding of phase transitions under extreme conditions. The increased ability to use Sandia's Z-machine in conjunction with computational materials modeling to understand the dynamic behavior of materials under extreme conditions is a vital capability for the stockpile stewardship program. Further, the study of the role of pressure on solidification kinetics complements the study of the role of temperature in traditional applications of solidification. Finally, the work demonstrates the ability of current *ab initio* modeling techniques to reliably predict quantities such as equation of state in cases where experiment is difficult or impractical.

Contact: Stephen Foiles, Computational Materials & Molecular Sciences Dept.
Phone: (505) 844-7064
Fax: (505) 844-9781
Email: foiles@sandia.gov

Modeling, Simulation, and Characterization of Earth Penetrator Steels

D. Susan, S. Viswanathan, B. Boyce

Motivation: The current earth-penetrator (EP) programs at Sandia are employing the largest, heaviest-wall forged cases ever produced for these applications. One difficulty in fabricating large variable-section penetrators is that the heat treatments of the alloys must address a key difference: heating and cooling rates are significantly slower than those associated with the small samples used to develop heat treatment schedules. The coupling of phase transformation models and heat flow models will allow tracking of the microstructure in these large parts during heat treatment. The goals of this research are: 1) to develop a phase transformation model for HP9-4-20 steel, 2) to develop the input data set (phase transformation kinetics, microstructures, and properties) using well-controlled lab thermal environments, and 3) to perform high strain rate property testing representative of penetration events. The model results will be validated on laboratory specimens and full-scale penetrators.

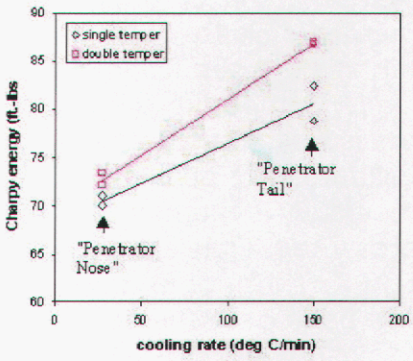

FIG. 1. Effects of quench rate and temper treatment on Charpy impact energy of HP9-4-20.

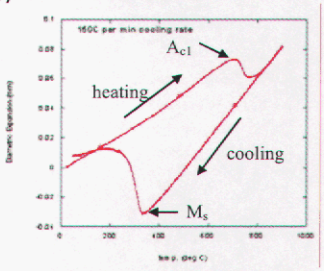

FIG. 2. Dilatometry curve for HP9-4-20 showing approx. transformation temperatures

Accomplishment: Laboratory thermal cycling was used to simulate heat treatment of the nose and tail regions of a large Penetrator (i.e. thick and thin sections). Figure 1 shows the effect of quench rate from austenite on Charpy impact energy of HP9-4-20 steel. The results indicate an improvement in Charpy impact toughness at higher quench rates and also show the beneficial effect of double tempering on Charpy impact toughness. Preliminary dilatometry experiments were also performed to determine the phase transformation temperatures for forged HP9-4-20 steel. The data obtained from dilatometry (Fig. 2) include the temperature at which transformation to austenite occurs on heating (A_{c1}) as well as the temperature of the austenite decomposition to martensite or bainite on cooling (M_s or B_s).

Evaluation of mechanical properties (yield strength, work hardening, ductility, etc.) of high-strength, high-toughness steels is relatively straight-forward at quasi-static rates up to ~20 s^{-1}. At rates of ~1000 s^{-1} and above, split Hopkinson bar techniques provide a method for characterizing mechanical behavior. However, rates in the vicinity of ~100-300 s^{-1} are the most relevant, and very difficult to obtain. In this project, we have been developing the capability to evaluate penetrator materials in this 100-300 s^{-1} sub-Hopkinson regime (Fig. 3). A short load-train with minimal grip mass, a 2" slack slot and a 0.25" rubber damping pad reduced the inertial noise of

the load to <10% of the overall signal. This is a dramatic improvement over what has often been reported in the literature.

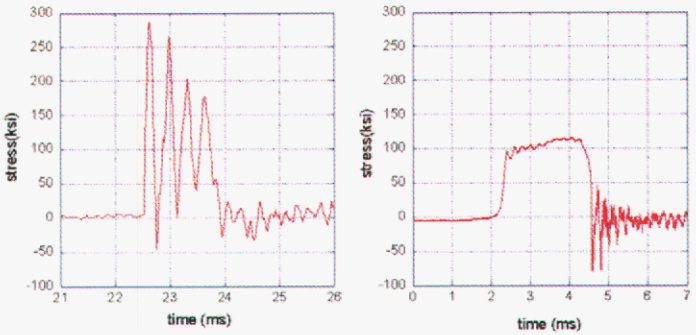

FIG. 3. (a) Stress-time profile of tensile test of 304 SS at strain rate of 300 s^{-1}. Inertial noise overwhelms the load-cell of a high-rate test frame. (b) Stress-time plot after identifying a suitable "pulse-shaping" configuration.

After studying and evaluating capabilities, DANTE was selected as the modeling platform because it provided the greatest flexibility and had the most advanced stress and microstructure models. It couples the thermal and mechanical response of the material with the evolution of microstructure (volume fraction of martensite, bainite, pearlite, etc.). The effect of volume changes due to phase change on residual stresses and distortion are also taken into account. Results from the DANTE/ABAQUS model for HP9-4-20 are shown in Figure 4. The model was 2D-axisymmetric and the mesh consisted of 1032 four-sided elements. The results indicate that the part was over 90% martensite after quenching (Fig. 4, legend). Figure 4 also shows the distortion obtained in the part. The actual distortion is quite small; for illustration, distortions were magnified 200 times.

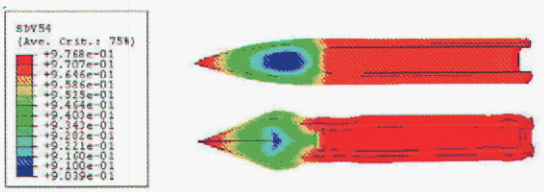

FIG. 4. Results from the DANTE/ABAQUS model using HP9-4-20 TTT and dilatometry data from the literature. The legend refers to the final martensite fraction at the end of the quench. The upper image indicates the final shape, while in the lower image distortions were magnified 200 times.

Significance:

Through lab thermal treatments and property testing, a beneficial effect of double tempering on toughness was shown, with only a slight decrease in strength for this alloy. Dilatometry experiments were performed to determine the phase transformation temperatures for HP9-4-20 EP steel as a function of cooling rate. The lab data will provide high fidelity inputs for modeling. The commercial codes DANTE and ABAQUS were used to model heat treatments of a sub-scale HP9-4-20 steel penetrator using data from the literature. The model included the thermal and stress response as well as phase evolution during heat treatment. In addition, a Sandia capability to evaluate mechanical properties of penetrator materials in the 100-300 s^{-1} sub-Hopkinson regime is being developed. This technique, combined with a high-rate strain measurement technique (under development in FY05) can now be used to compare mechanical properties of penetrator alloys at representative strain rates.

Contact: Donald F. Susan, Materials Reliability Dept.
Phone: (505) 284-4951
Fax: (505) 844-2974
Email: dfsusan@sandia.gov

Using Sintering Conditions to Control the Mechanical Properties of Sintered, Micro-Molded 316L Stainless Steel

T. Garino, B. Boyce, D. Zschiesche, D. Schmale

Motivation: Components for μ-systems are currently produced by either silicon μ-machining techniques or by the LIGA process. Silicon μ-machining, although ideal for many applications, can only produce microstructures a few μm thick and is limited to silicon and a few other materials. The LIGA process can fabricate high-aspect ratio thick parts out of metals that can be electroplated but requires expensive x-ray lithography, is slow and cannot produce ceramics and more complex metals such as rare-earth transition-metal magnets (NdFeB) or stainless steels. Therefore, μ-molding has been developed to complement these techniques for certain applications. In micro-molding, a fine powder is mixed with a binder and then introduced into a mold that can be injection molded from a LIGA-made master. Parts are subsequently removed from the mold and heated to pyrolize the binder and then to sinter the powder to produce a dense part with a high degree of dimensional tolerance.

Accomplishment: Typical stainless steel powders used in powder metallurgy have particles that are >15 μm in size. These powders are too coarse to be of use in micro-molding where features <50 μm in size need to be reproduced. Therefore, we have investigated two fine 316L stainless steel powders, a custom-made nano-powder made by Argonide Corp. and a micro-powder that has recently become commercially available from Atmix Corp. Using these powders, tensile specimens that were micro-molded and then sintered in 3% hydrogen for 1 hr at various temperatures. We then determined the mechanical properties of these specimens using a special miniature test tensile test system. The results for the Atmix powder, which had an initial average particle size of ~3 μm, are shown in Fig. 1. Sintering at 1075°C produced low strength and very low ductility due to the fact that the material was still quite porous, as shown in the micrograph in the figure. Sintering at 1150° to 1175°C produced ultimate tensile

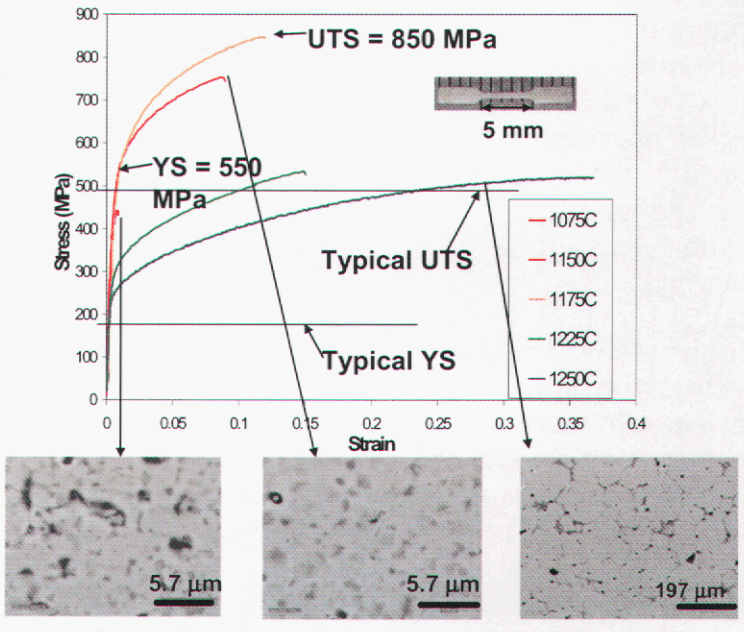

Figure 1. The stress-strain curves for micro-molded Atmix 316L stainless steel sintered in 3% hydrogen for 1 hr at several different temperatures with micrographs showing the different microstructures produced.

strengths (UTS) as high as 850 MPa, much greater than that of conventional material (~500 MPa) with reasonable ductility (~12% elongation at failure). The yield stress (YS) was also higher than the conventional material, 550 MPa vs. 175 MPa. In this case, the porosity was low and the grains were still quite small. Sintering at higher temperatures produced grain growth, which increased the ductility but lowered the strength to close to that of the conventional material. The results for the Argonide powder that had an average particle size of ~100 nm are given in Fig. 2. Even though it was possible to achieve higher YS and UTS (650 and 875 MPa, respectively, at 1200°C), all these samples had low ductility.

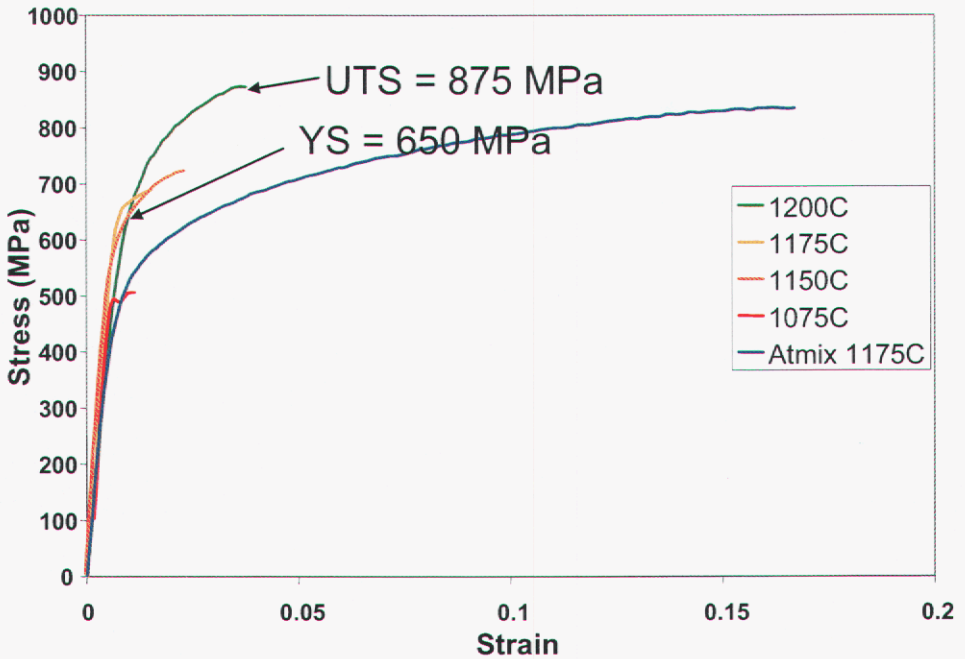

Figure 2. The stress-strain curves for micro-molded Argonide 316L stainless steel sintered in 3% hydrogen for 1 hr at several different temperatures. For comparison, the curve for the Atmix powder sintered at 1175°C is also shown.

Significance: These results demonstrate not only that stainless steel components for microsystems produced by sintering micro-molded parts have excellent mechanical properties, but more importantly that those properties can be easily varied depending on the requirements for a specific application, from high YS and UTS with low to moderate ductility, to values of YS, UTS and elongation similar to conventionally processed material.

Contact: Terry Garino, Microsystem Materials & Mechanical Behavior Dept.
Phone: (505) 845-8762
Fax: (505) 844-9781
Email: tjgarin@sandia.gov

Advanced Monolith Structures for Catalyst Applications

J. Stuecker, R. Ferrizz, J. Miller. J. Cesarano

Motivation: Monolithic catalytic reactors, widely utilized for environmental applications (automotive and stationary emissions control), are currently being considered for a variety of additional applications. Monoliths offer several advantages over traditional packed bed systems; perhaps the most significant of these is offering a high surface/volume ratio (similar to that of very small particles) with little resistance to flow (low pressure drop). Many of the potential new applications require very high gas flow rates (with space velocities up to 10^6 hr^{-1}). However, an inherent weakness of most monoliths is the potential for bulk gas-solid mass transfer limitations under high flow conditions. An additional limitation is that most monoliths are not applicable to highly endothermic or exothermic reactions where radial heat transfer is critical.

We are utilizing a novel direct ceramic fabrication technique (robocasting) to produce 3-dimensional ceramic monoliths, e.g. meshes with controlled porosity in all dimensions but no line-of-sight pathways. Compared to the traditional 2-dimensional "honeycomb" structured extrudates, our 3-dimensional structures promote higher mass transfer rates to catalytic surfaces while maintaining high surface to volume ratios, predictable permeability, and low pressure drop. Radial heat transfer is also likely to be enhanced. Robocasting allows for great flexibility in materials, possibly alleviating problems related to thermal shock and chemical degradation.

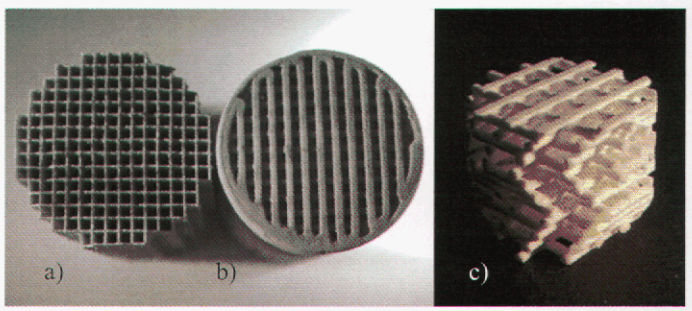

Figure 1. a) 75% porous honeycomb, b) 45% porous robocast FCC, c) 74% porous robocast modified FCC monoliths

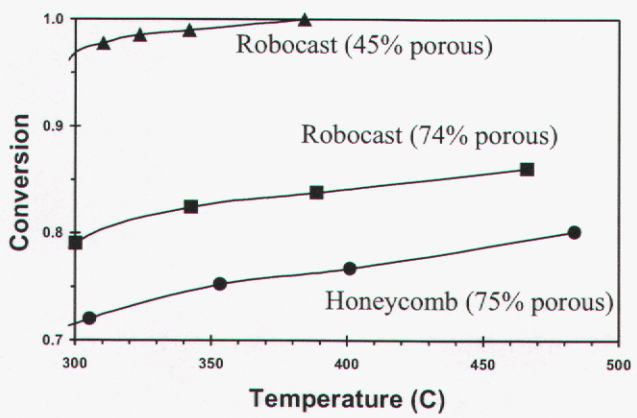

Figure 2. CO conversion (750,0000 hr^{-1}) over Robocast FCC and honeycomb monoliths

Accomplishment: Using CO oxidation over Pt as a probe reaction, it has been shown that robocast monoliths with an "FCC-like" geometry of alternating rods (for which there are no direct line-of-sight pathways) exhibit superior mass transfer properties relative to traditional honeycomb monoliths (Figure 1 a,b).

Robocast and honeycomb samples with identical dimensions, geometric surface areas, and catalyst loadings were both subjected to a high flow rate of 13,000 sccm (~750,000 hr^{-1}) of 1% CO in air. At 350 °C, it is evident from conversion vs. temperature plots that both samples are clearly in the mass-transfer-limited kinetic regime. CO conversion over the robocast sample was 99%, while it was only 75% over the honeycomb sample as seen in Figure 2. This corresponds roughly to a 3-fold increase in the Sherwood Number (a measure of convective mass transfer).

The reported gain in mass transfer was made at the expense of a significant increase in pressure drop. However much of this increase is due to the relatively small bulk porosity of the FCC sample (45%). A robocast sample that more closely matches the bulk porosity (74%), pressure drop, and surface area of the honeycomb monolith was tested and is shown in Figure 1c. This sample exhibits enhanced mass transfer properties (88% conversion at 350 °C) and no line-of-sight pathways.

Enhanced heat transfer (and mixing) is also more prevalent in robocast monoliths as shown by computational fluid dynamics modeling in Figure 3 (a,b) where two regions of gas (hot and cold) are kept separate up until the entrance of the monoliths. The cross-section views in Figure 3 (c,d) shows the enhanced mixing effect of the robocast monolith.

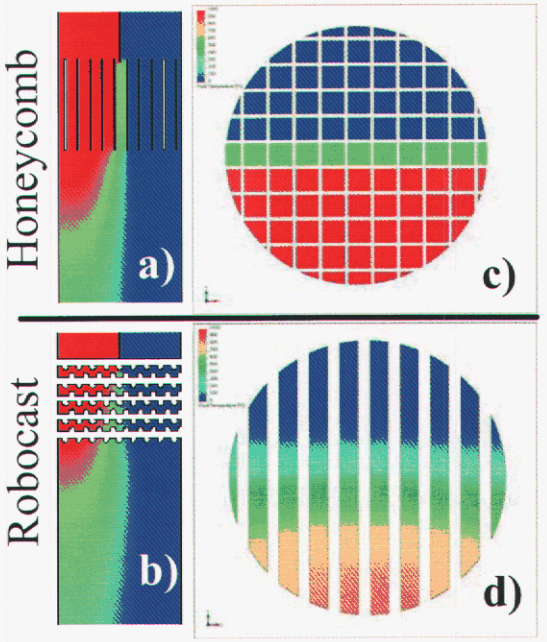

Figure 3. CFD model showing heat transfer/mixing through a) honeycomb and b) robocast monolith. Cross-sections respectively are c) and d).

Significance: The superior properties exhibited by robocast monoliths could potentially reduce the amount of precious metals needed for reactions (enhanced mass transfer), preserve the catalyst by preventing thermal runaways (enhanced heat transfer), and prevent harmful reaction byproducts by enhancing selectivity.

Contact: James E. Miller, Ceramic Processing & Inorganic Materials Dept.
Phone: (505) 272-7626
Fax: (505) 272-7336
Email: jemille@sandia.gov

Automotive Lean-Burn NOx Catalysis

E. Coker, D. Peña, S. Hammache, J. Miller

Motivation: Lean-burn (LB) engines have been identified by U.S. automakers as the next major technological step in combustion engine design and fuel economy. By using more air during combustion, LB engines, both gasoline- and diesel-fuelled, yield better mileage and produce less carbon monoxide and unburned hydrocarbon pollutants than conventional stoichiometric gasoline engines. However, destruction of NO_x pollutants, produced by all engines, is more difficult in a LB engine due to the excess oxygen present in the exhaust stream, rendering traditional catalytic converters ineffective. For LB engines to become commercially viable, novel catalyst technologies for exhaust treatment are needed. Two principal technological solutions are under development for reducing NO_x emissions in LB engine exhausts: Selective Catalytic Reduction (SCR) where a gaseous reductant reduces NO_x to N_2 in a continuous fashion, and NO_x Storage-Reduction (NSR) where NO_x is chemically stored and periodically reduced to N_2 by hydrocarbons in the exhaust. The SCR program, sponsored by the DOE Office of Transportation Technologies (OTT).

Accomplishment: A) SCR. Our initial goal was to develop hydrous metal oxide (HMO)-based catalysts to mitigate NO_x emissions in LB engine exhaust. The flexibility of the HMO process chemistry allowed a wide variety of catalysts to be screened for activity in the SCR of NO_x via hydrocarbon reaction using materials in bulk powder form. Promising catalyst compositions were fabricated and tested on small-scale cordierite monoliths. The best catalyst systems were further evaluated by scaling up to a full developmental size (110 cubic inch) catalytic converter (Fig. 1).

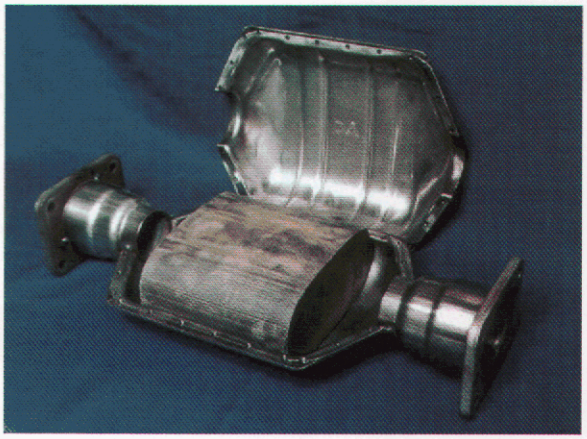

Figure 1. Sandia-fabricated full developmental size (110 cubic inch) catalytic converter in take-apart can assembly.

With the new EPA Tier II emission standards being phased in, we are now addressing new and potentially more efficient NO_x reduction options for LB exhaust, in particular the SCR of NO_x by urea (or NH_3), which has been shown to provide excellent NO_x reduction in stationary sources. To transition urea-SCR to mobile sources, several key parameters are under investigation, including the influence of space-velocity, exhaust composition, presence of residual hydrocarbons, temperature, and durability to sulfur poisoning and high-temperature excursions (Fig. 2). Furthermore, catalyst formulations free from vanadium (used in stationary sources) are targeted for environmental reasons. We are also engaged in determining the mechanism of the SCR of NO_x over different catalyst materials with various reductants, and are conducting mixed catalyst and support studies designed to optimize LB NO_x SCR catalysts.

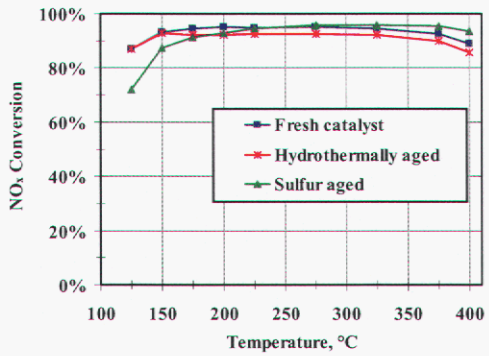

Figure 2. Sandia-developed NH_3-SCR catalyst shows high durability to hydrothermal aging (5% steam, 16 hours, 600°C) and sulfur poisoning (20 ppm SO_2, 24 hours, 350°C).

B) NSR. Since conventional NSR catalysts are intolerant of sulfur in the exhaust stream, our aim has been to develop catalysts which demonstrate enhanced tolerance to sulfur, which enters the exhaust stream burning of fuel and lubricant. It has been found that addition of copper to a traditional NSR catalyst formulation reduces deactivation by sulfur. Table 1 summarizes the NO_x capacities of traditional and copper-modified NSR catalysts both before and after accelerated sulfur aging. Although the copper-modified catalyst has a lower initial capacity for NO_x storage, this capacity is impacted only slightly compared to the traditional catalyst, whose NO_x capacity drops to below that of the copper-modified one after sulfur aging.

	NO_x storage capacity (μmol g^{-1})	
	Traditional (Pt/BaO-γAl_2O_3)	Copper-modified (Pt/Cu/BaO-γAl_2O_3)
Fresh catalyst	108	64
Sulfur-aged catalyst	54	56

Table 1. NO_x storage capacities of traditional and copper-modified NSR catalysts before and after accelerated sulfur aging (40 ppm SO_2, 12 hours, 380°C).

Significance: Lab-scale catalyst testing protocols reflecting the transient nature of automotive exhaust chemistry have been successfully developed and implemented. The catalyst formulations developed have brought catalytic LB NO_x removal technologies closer to acceptance by the EPA. Tests of developmental size hydrocarbon-SCR catalytic converters (Fig. 1) on a LB engine dynamometer showed NOx reduction activity rivaling a commercial benchmark catalytic converter. Total time from initial bulk screening to developmental size catalytic converter fabrication was less than 2 years.

Contact: Eric N. Coker, Ceramic Processing & Inorganic Materials Dept.
Phone: (505) 272-7593
Fax: (505) 272-7304
Email: encoker@sandia.gov

Nanoscale Design of Catalysts

E. Coker, W. Steen, J. Miller

Motivation: Hydrogen-powered fuel cell (H_2-FC) vehicles offer tremendous potential for economical transportation, with low environmental impact and which could reduce US dependence on imported oil. However there are several barriers to commercialization of such vehicles. One of these is the heavy reliance of current H_2-FCs on platinum as electrocatalysts for oxidation of hydrogen and reduction of oxygen. In order for H_2-FC vehicles to reach a widespread market, the quantity of platinum required per vehicle needs to be reduced. This project aims to reduce the platinum burden of H_2-FC catalysts through controlling platinum cluster size in the electrocatalyst using novel encapsulation-stabilization mechanisms. As cluster size decreases, the fraction of atoms in the cluster which are exposed to the gas phase increases, giving potential for greater catalytic activity per gram of platinum; most commercial electrocatalysts possess relatively large platinum clusters (e.g., 2.5 nm or above) in which at most ~ 50% of the Pt atoms are exposed on the surface of the cluster.

Accomplishment: We have developed methods to successfully prepare sub-nanometer platinum clusters in microporous stabilizing media (e.g., aluminosilicate zeolites), and have demonstrated the ability to control the size and size dispersion of the clusters through adjustment of platinum loading and processing parameters. Figure 1 shows a sample of zeolite X (faujasite structure) containing in-situ prepared Pt clusters below 1 nm in diameter. These clusters were prepared from a $(NH_3)_4Pt^{2+}$-exchanged sodium zeolite X by heating slowly in air to 350°C, and then cooling rapidly to room temperature. These clusters may be then rendered electrochemically addressable through in-situ generation of a conductive carbon matrix using infiltration-polymerization-carbonization methodologies to yield a Pt cluster-carbon-zeolite composite material. The Pt clusters in these materials exhibit strong resistance to sintering (where small clusters combine to make larger ones at elevated temperatures), a problem common for Pt catalysts. Upon removal of the zeolite by acid or base digestion, electrocatalysts (platinum-on-carbon) with performance at least as good as commercial benchmarks have been obtained. Figure 2 shows some preliminary electrochemical data for a series of samples prepared as described above, with the variable being the temperature used during

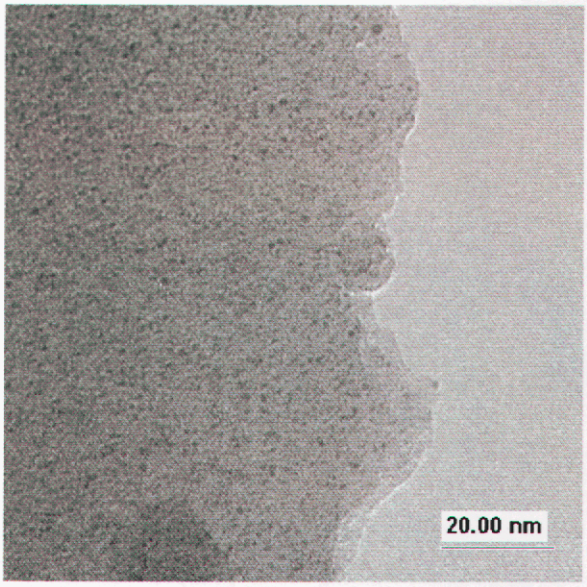

Figure 1. Sub-nanometer Pt clusters stabilized in zeolite X.

the carbonization step (conversion of polymer into conductive carbon under inert atmosphere). It can be seen that carbonization at ~ 800°C yields the most active catalyst (current density plots, Figure 2A); at lower temperatures the carbon is not sufficiently conductive, while at higher temperatures the catalyst begins to densify and some Pt sintering occurs. Analysis of the slopes of the current density plots at low potential allows estimation of the charge transfer resistance of the catalyst (i.e., how easy it is for an electron to move from a Pt cluster through the carbon to the electrode); Figure 2B confirms that at carbonization temperatures above 600°C, the charge transfer resistance is similar to that of a commercial material (straight line; Pt/XC-72 from E-Tek). Methods to further improve the electrochemical properties of these novel catalysts are being developed, and include use of different polymeric species to form the carbon matrix while minimizing the need for high-temperature treatment, use of conductive polymers in place of carbon, and the use of zeolites with varying nano-structures and pore sizes to broaden the size range within which the clusters may be tuned while maintaining good size control.

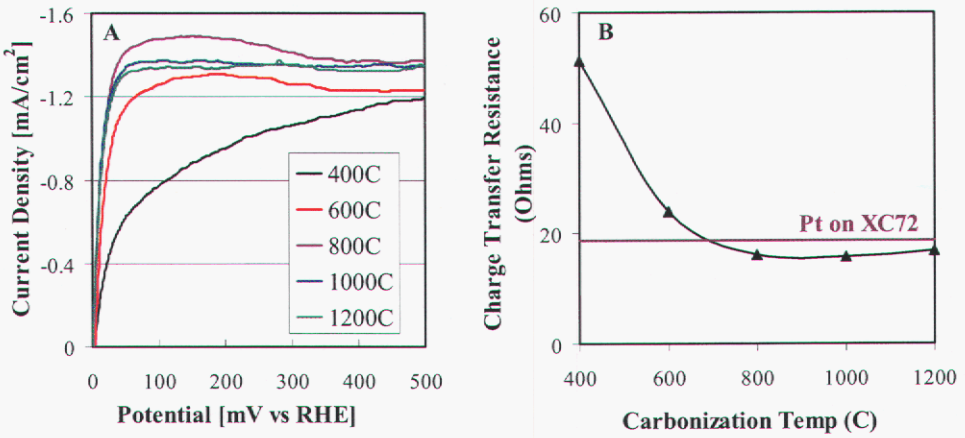

Figure 2. Rotating Disk Electrode analysis of Pt-carbon materials prepared using various carbonization temperatures. Current density plots (A), and charge transfer resistance versus carbonization temperature (B).

Significance: We have demonstrated unprecedented control over platinum cluster sizes in an electrocatalyst platform. Furthermore, the Pt clusters in these catalysts are more resistant to sintering than traditional electrocatalysts, and may offer enhancements in catalyst lifetime. As well as having potential to lead to catalysts requiring lower platinum loadings, these materials will be the subject of intense study in order to better understand the fundamental electrochemical properties of such small, supported clusters. This has not been possible to date due to the typically broad distribution of cluster sizes obtained through traditional electrocatalyst synthesis procedures.

Contact: Eric N. Coker, Ceramic Processing & Inorganic Materials Dept.
Phone: (505) 272-7593
Fax: (505) 272-7304
Email: encoker@sandia.gov

Development of Advanced Neutron Absorbing Alloys

C. V. Robino, J. R. Michael, J. J. Stephens

Motivation: Safe, long-term storage and disposal of U.S. Department of Energy-owned spent nuclear fuel (SNF) requires a long lasting material that will absorb emitted neutrons for nuclear criticality control. DOE's National Spent Nuclear Fuel Program (NSNFP) is developing a corrosion-resistant, nickel-chromium-molybdenum alloy containing gadolinium for criticality control in the DOE standardized SNF storage canister. These canisters will be disposed of in the waste packages at the Yucca Mountain Repository. Gadolinium is a potent neutron-absorbing element that has a very high thermal neutron absorption cross section. To meet the functional requirements for a structural material that will be used as an insert in the standardized canister, gadolinium must be alloyed into a corrosion-resistant structural metal that will meet ASME code requirements. In addition, because of the large volume of SNF and therefore the amount of absorber needed, it is imperative that the alloy be producible by conventional casting and hot rolling. The criticality safety requirements and waste package geometry constrain the alloy to a gadolinium level of about 2 wt%.

Accomplishment: The microstructure of the as-cast Ni-Cr-Mo-Gd alloy consists of primary Ni-Cr-Mo austenite and an austenite/GdNi5 eutectic constituent. At 2 wt% Gd, the volume fraction of the GdNi5 phase is approximately 6 vol%. This phase, which is stronger than the matrix at all temperatures up to the solidus, strongly affects the hot working response. In order to better understand the hot working behavior and optimize the resultant microstructure, we have developed new methods for hot deformation testing, and have applied advanced analytical techniques to assess the deformation characteristics.

The Iosipescu asymmetric flexure concept has been adapted to our weld thermo-mechanical simulator (Gleeble). This configuration is shown in Figure 1, and provides a deformation state of nearly pure shear in a small easily prepared sample. In comparison with hot uniaxial compression, the simplified strain state of the shear testing a provides more direct and less ambiguous method for assessing the deformation response of two phase microstructures such as those of the Gd-containing alloy.

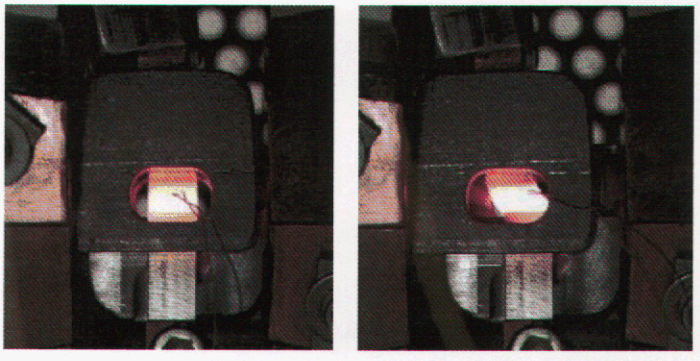

Figure 1. Photographs of Gleeble hot shear test before and after straining.

Analysis of the shear test samples was conducted by electron backscattered diffraction (EBSD) analysis in a scanning electron microscope, and an example image is shown in Figure 2. In this technique, a diffraction pattern is obtained,

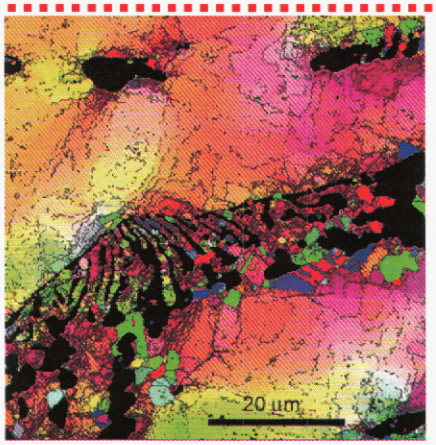

Figure 2. EBSD image from Gd alloy shear tested at 1050°C. Shear strain = 0.97, strain rate = 0.1/sec.

identified, and indexed at each pixel in an image area. In the image of Figure 2, the GdNi5 gadolinide phase is shown in black, while various orientations of the austenite are shown by different colors. In addition, misorientations between adjacent pixels of greater than 1° are shown by a thin line between the pixels as well as by gradation in the color. Dynamically recrystallized areas are shown as strain free regions bounded by higher angle boundaries. Thus, for the deformation conditions shown, the deformation is concentrated within the austenite of the eutectic region, and immediately adjacent to the eutectic. Larger volumes of dynamic recrystallization correlate with improved hot deformation response and hot ductility.

The effects of temperature and strain rate have been evaluated by this approach, and for a fixed strain of 1 and a strain rate of 0.1/sec, a maximum in the amount of dynamic recrystallization was observed at 1200°C. Similarly, the effect of strain rate at constant temperature and total strain, Figure 3, indicates that that the degree of dynamic recrystallization is maximum at strain rates in the range of 1-10/sec.

Significance: We have developed and demonstrated new testing and analysis procedures suitable for assessing the hot working response of the Gd-containing neutron absorbing alloy and other multi-component alloys. Hot working temperatures and procedures developed through this analysis have been used to specify working procedures for large scale Gd-alloy ingots. In turn, the mechanical properties data obtained from this plate have been used as part of an ASME Boiler and Pressure Vessel Code Case submission. It is expected that, ultimately, use of this alloy will help ensure safe and efficient disposal of SNF in the Yucca Mountain Repository.

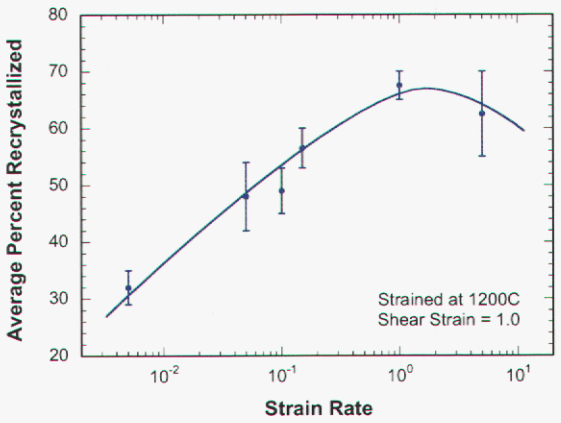

Figure 3. Effect of strain rate on the amount of dynamic recrystallization of a 2 wt% Gd Ni-Cr-Mo alloy at 1200°C and a shear strain of 1.

Contact: Charlie Robino, Joining & Coating Dept.
Phone: (505) 844-6557
Fax: (505) 845-9659
Email: cvrobin@sandia.gov

Highly Porous, Non-Ordered Metal Oxide Films Synthesized using a Templated Sol-Gel Route

D. Dunphy

Motivation: Porous films of metal and semimetal oxides (SiO_2, TiO_2, Al_2O_3, etc.) are promising materials for analyte preconcentration in chemical analysis, with potential applications in microanalytical systems. The surface charge, and thus the adsorption characteristics of the material, can be modified by choice of the specific metal oxide, while proper engineering of the pore structure can increase the available surface area available for molecular adsorption and introduce size selectivity for analyte discrimination, a useful property for analysis of biomolecules in complex matrixes. . Unfortunately, few metal oxide thin film materials have been produced with these characteristics (most notable TiO_2), and require very careful control of processing conditions, with a fairly time consuming procedure (t= ca. 24 hours, plus the time required for surfactant removal). Furthermore, these processing conditions are different for every material, precluding a generalized synthesis procedure that would enable rapid engineering of material properties. We have devised an alternate, more generalized sol-gel route to porous metal oxide films, and have used this procedure to produce a range of materials including ZrO_2, TiO_2, HfO_2, Al_2O_3, and Fe_2O_3.

Accomplishment: A simple method for the control of porosity in sol-gel films is templating by liquid-crystalline mesophases formed through concentration of amphiphillic surfactants (added to the precursor sol) by solvent evaporation during film formation, a process known as evaporation-induced self assembly (EISA). After template removal by pyrolosis or UV treatment, an ordered porous cast of the original mesophases is left behind, with pore sizes in the range of ca. 2-10 nm, a narrow pore size distribution, and (under the right conditions) a well-connected 3D pore network that enables mass transport throughout the thickness of the film. However, this approach has been most successful when applied to silica. The high reactivity of sol-gel precursors for other metal or semimetal oxides, coupled with poor oxide network formation ability after film formation and subsequent crystallization during template removal, greatly increases the difficulty of synthesizing porous films with open 3D pore structure and controlled pore size for these materials. This technique utilizes an epoxide-based proton scavenger (such as propylene oxide) to control the condensation of sol-gel precursors before film formation, while enabling a simplified post-deposition film treatment to strengthen the oxide network before surfactant

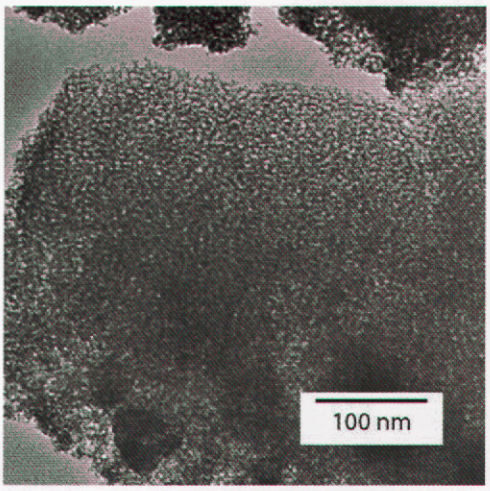

Figure 1. TEM image of a ZrO_2 film, synthesized using an epoxide-based route and templated with the surfactant Brij 56, showing a high degree of porosity for this material.

removal. In addition to decreased film processing time (t < 2 hours, not counting the time needed for template removal) and complexity, this technique produces films of very high macroscopic quality with an easily controlled average pore size.

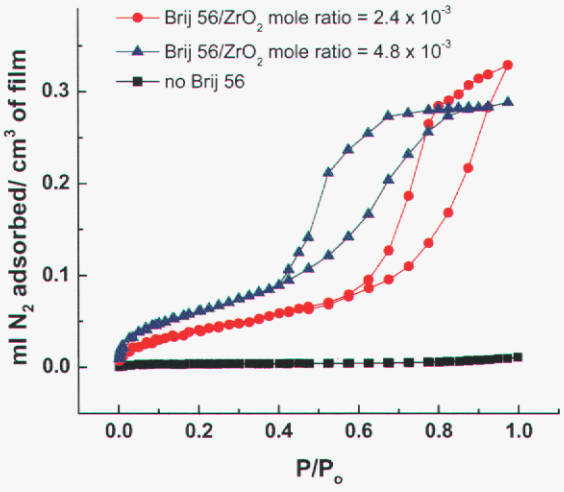

Figure 2. Nitrogen adsorption isotherms, obtained using a mass-sensitive surface acoustic wave (SAW) device, of ZrO_2 films templated with different amounts of the surfactant Brij 56. Note that the inverse relationship between the relative pressure where pore filling occurs (and thus pore size) and the Brij 56/ZrO_2 ratio is a real effect

We have performed extensive characterization of the pore network structure for ZrO_2 films produced using this epoxide-based approach. Unlike films made using standard sol-gel chemistry and EISA, the pore network obtained using this epoxide route do not possess any regular mesoscopic order (Figure 1), although nitrogen adsorption experiments are consistent with the presence of well-connected 3D porosity with average pore size (ca. 5-20 nm) controlled by the amount and identity of the surfactant template, and pore size distributions intermediate those of random structures and other, more ordered materials synthesized using EISA (Figure 2). It should be pointed out that this pore size range is larger than that easily obtained by the standard EISA route, an important characteristic that will allow more facile mass transport of larger biomolecules into the film structure. Total porosities of 30-50% have been confirmed using spectroscopic ellipsometry. Finally, x-ray diffraction shows the presence of crystallinity in the pore walls with domain sizes around 15 nm.

Using semi-quantitative fluorescent labeling, we have shown that porous ZrO_2 films synthesized in this manner can adsorb DNA from solution, and that this adsorption is stronger than that seen for pure silica.

Significance: We have demonstrated that we can rapidly synthesize a wide range of high-quality porous metal-oxide films using this epoxide-based approach, and that the average pore size of these films can easily be engineered by choice and amount of surfactant template. Also, the feasibility of using these films as biomolecule adsorbents has been established.

Contact: Darren Dunphy, Ceramic Processing & Inorganic Materials, Dept.
Phone: (505) 272-7120
Fax: (505) 272-7336
Email: drdunph@sandia.gov

Cadmium Amido Alkoxide and Alkoxide Precursors for the Synthesis of Nanocrystalline CdE (E = S, Se, Te)

T. Boyle, T. Alam, T. Headley

Motivation: Demonstrating control of the size, morphology, and composition of nanoparticles is necessary to help realize the potential of this exciting scale of matter. In order to gain this control, it is necessary to understand the variables that influence these important characteristics. Several literature reports indicate that the growth and morphology of CdE (E = S, Se, Te) or of quantum dots are independent of precursor or synthesis route. If true, then serious limitations will exist for the development of devices that incorporate CdE nanomaterials. Due to the incredible sensitivity of ceramic material properties on the structure of the metal alkoxide precursors, we elected to study the effect of $Cd(OR)_2$ and mixed ligand $Cd(NR_2)(OR)$, where $NR_2 = N(SiMe_3)_2$, on the resulting morphology of nanoparticles of CdE.

Accomplishment: The synthesis and characterization of a family of alternative precursors for the production of CdE nanoparticles (E = S, Se and Te) was undertaken to demonstrate the effect precursors have on nanoparticle morphology. From the reaction of $Cd(NR_2)_2$ where $NR_2 = N(SiMe_3)_2$ with *n* HOR led to the isolation of: *n* = 1 $[Cd(\mu\text{-}OCH_2CMe_3)(NR_2)(py)]_2$ (**1**, py = pyridine), $Cd[(\mu\text{-}OC_6H_3Me_2\text{-}2,6)_2Cd(NR_2)(py)]_2$ (**2**), $[Cd(\mu\text{-}OC_6H_3(CHMe_2)_2\text{-}2,6)(NR_2)(py)]_2$ (**3**), $[Cd(\mu\text{-}OC_6H_3(CMe_3)_2\text{-}2,6)(NR_2)(py)]_2$ (**4**, shown in Figure 1), $[Cd(\mu\text{-}OC_6H_2(NH_2)_3\text{-}2,4,6)(NR_2)(py)]_2$ (**5**), and *n* = 2 $[Cd(\mu\text{-}OC_6H_3Me_2\text{-}2,6)(OC_6H_3Me_2\text{-}2,6)(py)_2]_2$ (**6**), and $[Cd(\mu\text{-}OC_6H_3(CMe_3)_2\text{-}2,6)(OC_6H_3(CMe_3)_2\text{-}2,6)(THF)]2$ (**7**). For all but **3**, the X-ray crystal structures were solved as discrete dimeric units bridged by alkoxide ligands and either terminal $-NR_2$ or -OR ligands depending on the stoichiometry of the initial reaction. These complexes were further characterized in solution by multinuclear NMR and solid-state ^{113}Cd NMR spectroscopy.

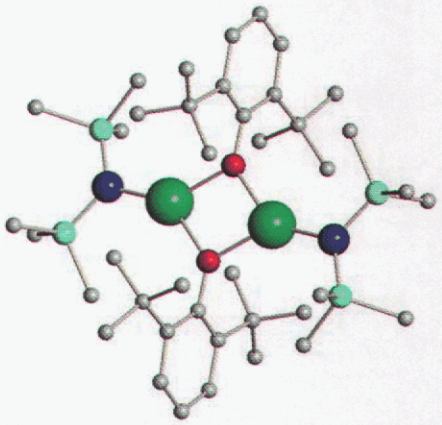

Figure 1. Plot of one of the novel precursor used for nanoparticle synthesis, $[Cd(\mu\text{-DBP})(NR_2)]_2$.

The utility of these complexes as "alternative precursors" for the controlled preparation of nanocrystalline CdE was explored. A survey of CdE nanocrystals was completed using a different precursor for each synthesis to determine if **any** morphological control was available. CdE nanoparticles, synthesized from **2 - 7**, were prepared by slight modification to a literature methods Experimentally, TOPO, ODPA or TDPA, and the cadmium precursor were heated until a transparent solution resulted. A chalcogenide solution was then injected and the growth temperature

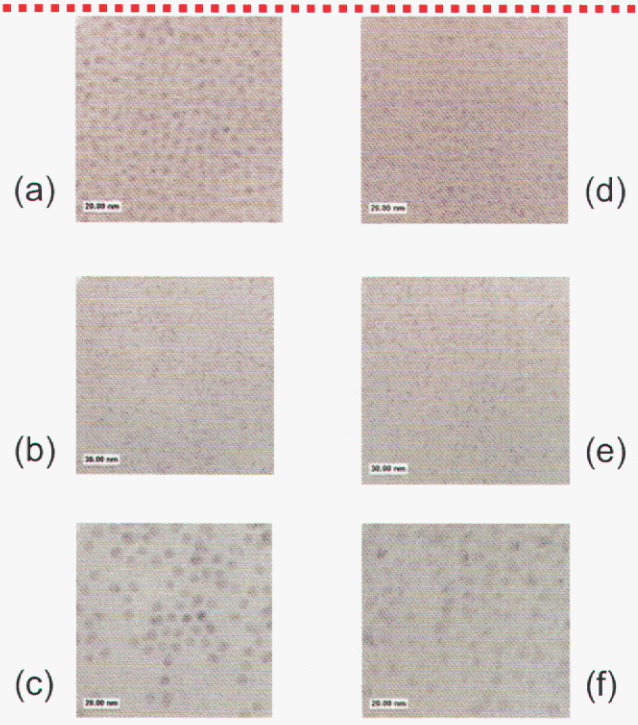

Figure 2. TEM images of CdE from (a) 2, E = S; (b) 3, E = Se, (c) 4, E = Te, (d) 5, E = S; (e) 6, E = Se and (f) 7, E = Te .

was set to 320 °C. The progress of crystal growth for each CdE was monitored by UV-*vis* spectroscopy and TEM. For all of the reactions, the ratio of cadmium precursor to surfactants, the moles of chalcogenide injected and the temperature of the reaction over a two hour time period were kept constant. Under these conditions, it was found that the oxide (CdO) and acetate ($Cd(OAc)_2$) derivatives yielded nanoparticles of similar sizes and shapes. For CdS (**2** and **5**; Figure 2a and d) 4 - 5 nm sized spherical and for CdSe (**3** or **6**; Figure 2 b and d) show ill-defined rods. Both results are somewhat consistent with literature reports. However, for compounds **4** and **7**, spherical CdTe (Figure 2c and f) were isolated which was surprising since the typical CdTe morphology is typically a tetrapod.

Significance: This work has demonstrated for the first time that CdE nanoparticle morphology can be controlled by the precursors. Thus, more control is available for CdE nanomaterials than previously reported, and, along with a better understanding of the growth process, will result in a potentially wider range of functionality for the nanomaterial assemblies.

Contact: Timothy J. Boyle, Chemical Synthesis & Nanomaterials Dept.
Phone: (505) 272-7625
Fax: (505)272-7336
Email: tjboyle@sandia.gov

Complex Functional Nanostructures

J. Voigt, E. Spoerke, J. Liu

Motivation: Extended and oriented nanostructures of technologically important materials are desirable for many applications. The ability to synthesize these materials in a range of different nano-architectures (from controlled morphology nanocrystals to surface templated 3-D structures) will provide new opportunities for the development of interactive interfaces for optics, electronics, and sensors. As nature has shown, solution-based synthesis is a powerful approach for creating nano-structured materials. Although there have been significant recent successes in its application to fabricating nanomaterials, the general principles that control solution synthesis processes remain not well understood. Building on our core capability of the solution synthesis of ceramics, we are working to develop the scientific principles required to design and build bio-inspired nanostructures in crystalline oxides, II/VI semiconductors and other materials using solution-based molecular self-assembly techniques.

Accomplishment: Using the aqueous-based synthesis of ZnO as a model system, we have been able to produce a wide range of unusual, complex microstructural features that are remarkably similar to biomaterials. For example, using multiple step seeded nucleation and growth, and using citrate as the surface modification agent, large arrays of ZnO nanostructures that are very similar to those from biogenic calcium carbonate were produced. Figures 1a and 1b compare the oriented columns of ZnO nanoplates with the structure of nacreous aragonite. Figure 1a shows the column-like growth of ZnO plates, where the nanoplates were grown on top of oriented ZnO nanorods. The growth of the oriented nanoplates is quite unusual, and is directly related to the function of the organic acid (citrate) that prohibited the growth of rods and promoted the growth of plates. This ZnO nanolaminate microstructure closely resembles the plate-like structure of layered nacre in Figure 1b. The film growth approach developed for the ZnO system has been applied to several other material systems to produce oriented nanostructures, including conductive polymers, TiO_2 nanowires, and mesoporous silicates. For example, a novel hierarchical and self-similar crystal-growth process has been used to produce controlled morphology mesoporous silicate film structures with ordering from the nano- to micro-scale (see Figure 2 for several examples of the unique structures that can be produced by this process).

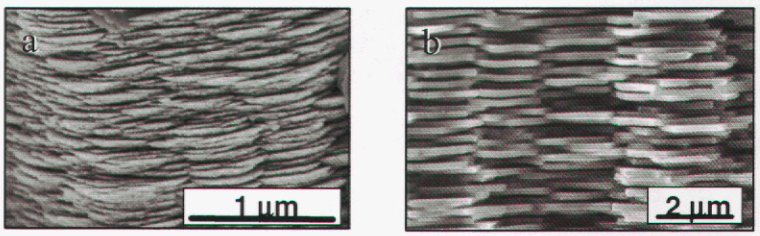

Figure 1. SEM photomicrographs of: a) nanoplate growth of ZnO and b) plate-like structure of layered abalone nacre ($CaCO_3$).

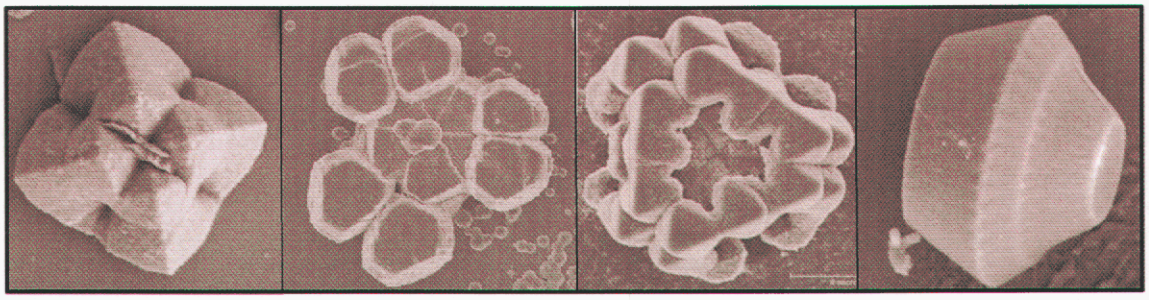

Figure 2. SEM photomicrographs of a sampling of the crystal morphologies and hierarchal structures of mesoporous silicates that have been grown on glass substrates.

Significance: The ability to nano-engineer complex architectures of technologically significant materials opens the door to new applications. The advantages of the architectured ZnO in the photocatalytic decomposition of volatile organic compounds (VOC) have already been demonstrated. The novel nanostructures we are developing are expected to have great potential for applications in sensing, catalysis, optical emission, piezoelectric transduction, actuations, etc.

Contact: Jun Liu, Chemical Synthesis & Nanomaterials Dept.
Phone: (505) 845-9135
Fax: (505) 844-5470
Email: jliu@sandia.gov

Modeling Studies of Droplets on Superhydrophobic Surfaces

F. van Swol, S. Challa

Motivation: Solid interfacial energy and rough surface topography confer to Lotus plants superhydrophobic (SH) properties like high contact angles, rolling and bouncing of liquid droplets, and self-cleaning of particle contaminants, easily justifying that Lotus' reputation as the symbol of purity. The detailed behavior of water or aerosol droplets impinging on an SH surface is a central issue that impacts particle collection and the (self-)cleaning of (bio-) contaminated surfaces as well as other applications such as water exclusion and inkjet printing. In general, water droplets will bounce off a SH surfaces rather than stick. Time lapsed photography shows that during a collision the droplets deform on contact (flatten) and reform upon leaving the surface. The degree of deformation and the associated dynamics of droplet collisions are of great relevance to the removal of small foreign objects. This project is concerned with the study of bouncing droplets at the smallest levels (1-100 nm), testing the hydrodynamic predictions made for larger length scales.

Accomplishment: Depending on the droplet's size and viscosity, as well as the presence of surface friction and impact velocity, a variety of outcomes are possible. These have been the focus of much recent fundamental work in this area. For similar reasons the development of detailed understanding of the nature of *lateral* motion of droplets, that is rolling and/or sliding, is of equal importance. These phenomena and recent experiments have inspired us to perform molecular dynamics (MD) simulations of both bouncing and rolling.

MD simulations were initiated to study the dynamic behavior of droplets bouncing off SH surfaces as well as rolling down inclined SH surfaces. The Lennard-Jones potential was used to study droplet diameters ranging from about 6 nm to 32 nm in contact with a smooth planar wall, representing the surface. The interactions of the wall and the fluid could be tuned to control the contact angle over the full range of 0 degrees for complete wetting to 180 degrees for complete drying on SH surfaces. In addition, an optional dissipative force was added within approximately 1 nm of the wall. This latter force represents the friction that fluid molecules in contact with a surface experience. Finally, we added an optional one-body external field to account for the gravitational force.

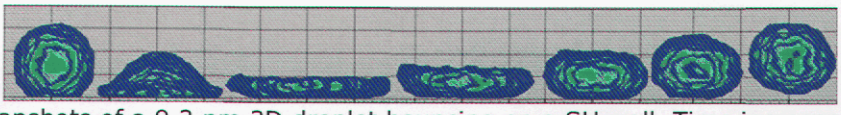

Figure 1 Seven snapshots of a 9.2 nm 3D droplet bouncing on a SH wall. Time increases from L to R. The sequence starts when the droplet first contacts the purely repulsive SH surface. The leading edge of the droplet distorts while the droplet spreads as the momentum continues to be pointed downward. The largest diameter is reached when the droplet is starting its rebound as the outer edges are already slightly lifted, and continues during the final frames. Lift-off occurs when the trailing edge of the droplet loses contact with the wall. Note that the spherical shape has not been fully re-established.

Bouncing Droplets–Experimental observations (Richard et al. (2002)) using a high speed camera have shown that the contact time for bouncing droplets (of constant radius R) is independent of impact velocity, despite the wide range of deformations observed. In contrast, the collision's impact time is a strong function of R (i.e. $\sim R^{3/2}$). We conducted MD simulations is to study the contact time behavior for nano-sized droplets, a size regime where conventional hydrodynamics might be expected to breakdown. A variety of sizes and impact velocities was studied, covering the same range of Weber ($We=V^2R\rho\gamma$) numbers as

probed in the experiments. An example of high impact velocity is shown in Figure 1. The drop is seen to flatten and spread over the surface to a diameter that is about twice the original size before reconstituting itself and lifting off. Observed contact times are collected in Figure 2, where we plot the contact time (t_c) as function of drop radius (R). We note that the observed R dependence, $\sim R^{1.66}$, is slightly stronger than what is predicted (and experimentally confirmed) for the continuum limit: $\sim R^{3/2}$. Further simulations will reduce the current uncertainty for the exponent. The droplet's deformation upon impact varies widely with impact velocity. At small values of We, the droplets simply exhibit an ellipsoidal shape upon contacting the wall, but at high We the droplets are seen to spread into toroidal shapes that can even exhibit cavitation, or dry spots in the center. We find that lift-off first starts at the edge of the drop and at high We the droplets will actually leave the wall while still in a deformed toroidal state. These results have implications for the most efficient particle collection from SH surfaces.

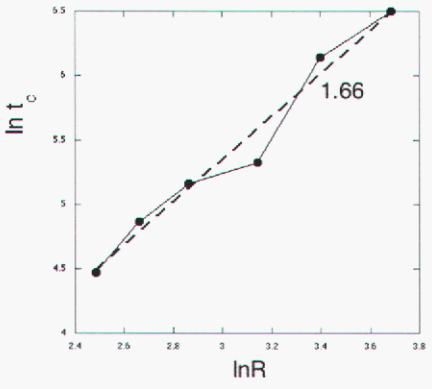

Figure2 MD results of the contact time of a bouncing droplet for varies radii.

Rolling Droplets–Recently, Mahadevan and Pomeau (MP) have provided several predictions for droplets on an inclined SH plane. Under the influence of gravity a droplet will start to move down the plane in a manner that (sliding versus rolling) has long been debated. MP distinguish droplets smaller (or larger) than the capillary length $a_c=(mgp/\gamma)^{1/2}$. Larger droplets flatten into a "puddle" shape of thickness $2a_c$ and reach a terminal velocity, V_0, that is, remarkably, found to be *independent* of either mass or gravity! Specifically, $V_0=0.75(\gamma\eta)\sin\alpha$, where α is the tilt angle, γ is the surface tension and η the viscosity. The terminal velocity stems from the balance of viscous dissipation and gravitational energy. The dissipation region of "puddle" drops coincides with the entire droplet (see MP). Smaller droplets ($R<a_c$) are expected to remain quasi-spherical, and their terminal velocity *exceeds* V_0. MP predict a dissipation region limited to the wall contact region with elsewhere a rigid-body rotation that induces zero dissipation. (On traditional non-SH surfaces, so-called partially wetted surfaces, the drop *slides* and the velocity *increases* with R.) Quere et. al. have confirmed some of the MP predictions for rolling mm-sized drops.

We have recently embarked on MD simulations of rolling droplets that are of nm size to 1) investigate what modifications occur at the nanoscale due to the increased role of fluctuations, and 2) identify in detail the nature of the motion and the extent of the dissipative region. Our initial calculation of the terminal velocity for a larger drop (i.e. $R > a_c$) agrees with the MP predictions. A detailed mapping of the velocity and pressure tensor field, predictions not tested thus far, is under way.

Significance: The degree of deformation and the associated dynamics of droplet collisions are of great relevance to the removal of small foreign objects. The bouncing droplet can cover an area that is substantially larger than its size (dynamic spreading), and this effect can be exploited to collect and pre-concentrate foreign particles (e.g. Anthrax spores) without any further mechanical contact or manipulation!

Contact: Frank van Swol, Computational Materials & Molecular Sciences, Dept.
Phone: (505) 845-9523, Fax: (505) 844-9781
Email: fbvansw@sandia.gov

Nanocrystalline Particles for Bio- and Nanotechnology

T. Lambert, T. Boyle

Motivation: Microbes have been found living under every condition imaginable from oceans to terrestrial to subsurface environments. The diversity of the functions displayed by these living species is astounding and are expected to be useful for the Genomics GTL program of the Office of Biological and Environmental Research of the Department of Energy for such issues as carbon sequestration, energy management, remediation of heavy metal contaminated sites, and hydrogen-production. To fully exploit and manipulate these species it will be critical to map the systems biology of these microbes. Hence, new probes that would allow for the temporal and spatial imaging of the makeup (lipids and proteins) of these microbes are required. Molecular fluorescent probes such as quantum dots (QD or CdSe nanocrystals) have become of increased interest as imaging "nanoprobes" since microscopic detection and measurement of a single localized bright nanoprobe is more quantitative and reliable than from an equivalent number of fluorophores dispersed throughout a larger volume. Quantum dots also exhibit high quantum yields, are resistant to photobleaching and their spectroscopic properties can be tuned. A number of our external collaborations have been with microbiologist interested in human cellular behavior and this work has been directly applicable to these systems as well. Therefore, a great deal of our research effort has been from our collaborative studies on human cells; however, the information garnered from mammalian cell lines can be applied to the DOE relevant microbes.

Accomplishment: Our research has integrated our nanotechnology and molecular recognition expertise with expert biologists to develop new probes to image events specific for the localization of key signaling proteins and lipids. Our biocompatible nanoparticles have shown outstanding potential as labels for extra-cellular determinants like receptors and adhesion molecules. For example, with an external collaboration with Professor B. D. Smith (Notre Dame), we have recently demonstrated for the first time the use of functionalized quantum dots for imaging the appearance of phosphatidylserine (PS) on the surface of apoptotic cells. In collaboration with Drs. J. Oliver and B. Wilson (University of New Mexico) new insight into the PS-distributions during RBL-2H3 mast cell activation has also been obtained (PS also appears in the outer leaflet of the membrane bi-layer during mast cell degranulation). For example, intact resting cells (not shown) failed to bind PS-

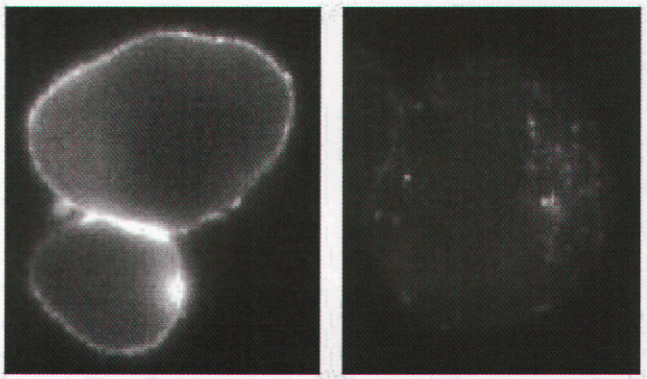

Figure 1. Fluorescence microscopy images of RBL-2H3 cells labeled with PS-sensing QDs. Activated cells (right) bound 550 nm QDs in a punctuate pattern. Permeabilized cells (left) show bright uniform staining.

sensing QDs while intact activated cells (Figure 1 – right panel) bound PS-sensing QDs in a punctuate pattern, most likely marking specialized sites of granule fusion with the plasma membrane. Activated and permeabilized cells (Figure 1 - left panel) showed bright uniform staining, most likely representing interactions of the functionalized QDs with PS that is believed to distribute uniformly in the inner leaflet of the membrane. We are currently developing other lipid-specific probes for application in live cell imaging.

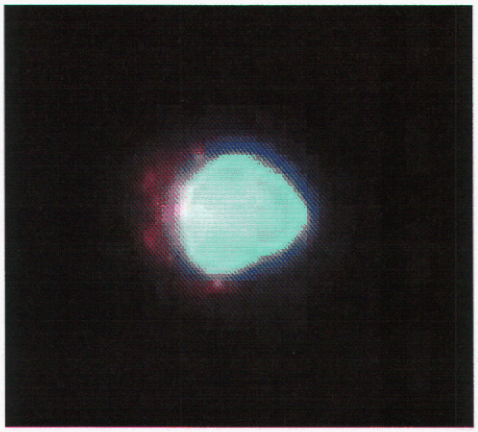

Figure 2. Fluorescence microscopy Images of RBL-2H3 cells stained with Hoechst (blue) and Streptavidin QD+biotin-polyarginine (red).

Realizing the full promise of nanoparticles for live cell-signaling imaging will require "gentle" methods to access intracellular targets. Functionalizing the nanoprobes to allow for transmembrane delivery is thus another challenge for chemists. To address delivery, translocation strategies based on coating fluorescent nanoparticles with poly(arginine) based cell-penetrating peptides have been developed. QDs coated with these peptides readily entered mast cells in what appears to be an endocytotic pathway as demonstrated by intracellular, extra-nuclear punctuate fluorescence (Figure 2). The application of this technology to study intracellular lipid/protein signaling and trafficking is ongoing.

Significance: The technologies currently under development here will ultimately allow for the real-time analysis of the lateral and trans-bilayer movement of lipids within a cell. Additionally, imaging the enzymatic modification of lipids during cell signaling as well as monitoring protein trafficking inside relevant microbes should be realized in due course. As many cell signaling events are mediated through lipid binding or enzymatic modification, these new probes should prove useful in understanding a variety of cell-signaling pathways. These new probes will also prove useful in developing Sandia's imaging capabilities, such as the hyper-spectral confocal microscope. Finally, the technologies being developed to produce these new probes will be readily applicable to new nanoparticle based sensor devices.

Contact: Timothy N. Lambert, Chemical Synthesis & Nanomaterials Dept.
Phone: (505) 845-9386
Fax: (505) 844-9781
Email: tnlambe@sandia.gov

Polarization Mediated Assembly of Functional Nanostructures

T. Boyle, B. Hernandez-Sanchez, T. Lambert, S. Daniel, L. Tribby, L. Ottley, R. Sewell, H. Pratt, C. Barros, P. Clem, T. Headley, B. Tuttle D. Li, D. Bonnell (U Penn)

Motivation: One pinnacle goal of nanoscience is the ability to control and produce complex devices that integrate nano-, micro-, and macro- length scales. It has been demonstrated that self assembly is useful in producing simple and repetitive structures; however the production of complex devices will require some form of directed process. The procedures described here are being performed through a collaboration between the Sandia National Laboratories and the University of Pennsylvania. These two research institutions are brought together through the Center for Integrated NanoTechnology (CINT) sponsored by the Office of Basic Energy Science.

Accomplishment: We have met the challenge for the direct integration of nanoscale materials and structures into the micro- and macro-scale through the Polarization Mediated Assembly of Functional Nanostructures (PMAFN). This methodology makes use of arrays of atomic polarization to direct site specific adsorption and chemistry. It also offers the advantage of using linkage chemistry not limited to reactions used in self assembly. Here ferroelectric lithography, Figure 1, is utilized for the directed assembly of multiple component structures in predefined locations. The sequential steps include: pattern polarization orientation, site selective reaction of nanomaterials, surface functionalization of the nanomaterial used, adding new polarization patterns, and further selective reaction of a different nanomaterial. This process can be repeated several times.

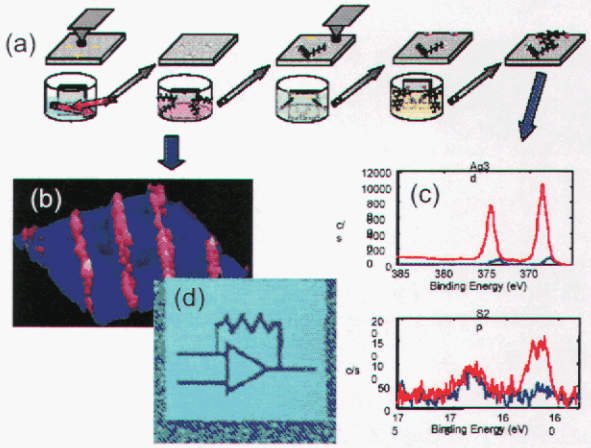

Figure 1. General schematic diagram (a) for Polarization Mediated Assembly of Functional Nanostructures. Patterned Ag "wire" structures (b) fabricated using PMAFN. Confirmation through XPS (c) of dodecanethiol functionality attached to Ag nanoparticles "wires". Piezoresponse image (d) of a "written" pattern on a pooled PZT substrate.

We have used both literature and novel synthetic procedures to generate a library of nanomaterials with various sizes, morphologies, and properties. The library comprises metals (i.e., Au, Ag, Cu, Pt, Co, Fe), semiconductors (i.e., CdS, CdSe, CdTe, InP, InAs), alloys (FePt, CuAu, IrPt, SnPt), and ceramics (ZnO, ZnS, $SrTiO_3$, $BaTiO_3$, PZT). Our ever expanding library of nanomaterials is aided by our continuous efforts in designing novel metal alkoxide precursors to explore final structure-property relationships of materials. Through the development of the

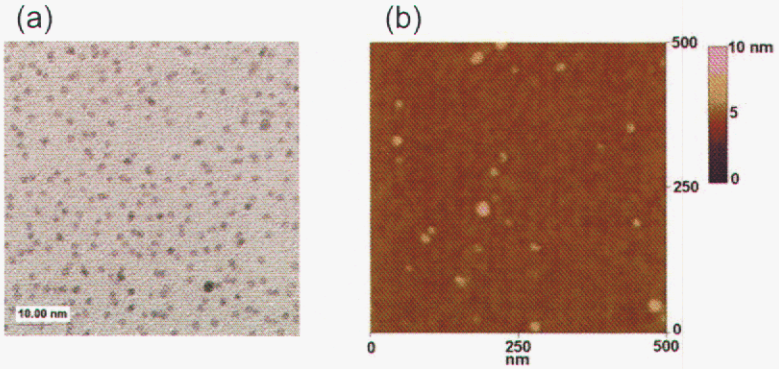

Figure 2. Analysis of FePt particles size and deposition of particles onto Si substrate. The TEM image (a) reveals 3–5 nm FePt nanoparticles were synthesized. Scale bar is 10 nm. AFM image (b) reveals that the as deposited particles on to a Si substrate with no pattern have ~5 nm heights.

synthetic routes used to generate nanomaterials, we are observing a direct correlation between the final resulting morphology of the nanomaterials and the precursor's molecular structure. The nanomaterials generated at Sandia National Laboratories are being investigated for their applications in polarized mediated assembly of functional nanostructures (PMAFN) at the University of Pennsylvania. Imaging studies and optimization of nanomaterials deposition onto a variety of substrates have been performed. Figure 2 shows transmission electron microscopy (TEM) and atomic force microscopy (AFM) images of 3–5 nm FePt particles dispersed with hexanes. Slow evaporation, spincast deposition, and langmuir bloggett techniques have been evaluated. The surface chemistry of the nanoparticles is also being modified through functionalization. Here, reactivity of the nanomaterials are enhanced by the incorporation of $-NH_2$, -SH, and –COOH end groups. In addition, a variety of new patterns is being generated. Figure 3 illustrates the capabilities of ferroelectric nanolithography to write complex patterns. The size of the pooled area can be as small as 10–20 nm based on the ferroelectric domain.

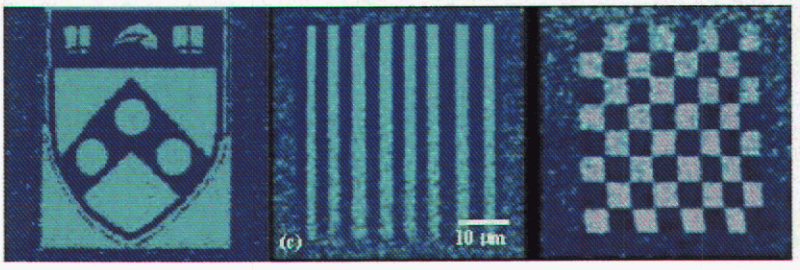

Figure 3. Piezoresponse images demonstrating the complexity of patterns that can be made using ferroelectric nanolithograpy.

Significance: The development of novel, complex, and functional nanostructures is underway. The formation of these structures will contribute to a deeper understanding of the interface between Å, nm, and μm length scales. The integration of nanomaterials to micro and macro materials will also aid in determining new structure-properties that will be useful to DOD, DOE, homeland security, and medical applications.

Contact: Timothy J. Boyle, Chemical Synthesis & Nanomaterials Dept.
Phone: (505) 272-7625
Fax: (505)272-7336
Email: tjboyle@sandia.gov

Self-Assembly and Integration of Water-Soluble Nanocrystal-Micelles

H. Fan

Motivation: We have developed methods to synthesize monodisperse nanocrystals (NCs) in aqueous conditions providing the abilities to 1) conjugate with biospecies (e.g., DNA antibodies etc.) for bioimaging, and to 2) create robust multifunctional NC arrays for development of collective eletronic/photonic behavior and controlled catalysis.

Accomplishment: We have developed the direct synthesis of water-soluble nanocrystalline micelles (NC-micelles). Our concept is to consider organically-passivated nanocrystals as large hydrophobic molecules that, if incorporated individually into the hydrophobic interiors of surfactant micelles, would result in the formation of NC-micelles composed of a metallic (or other) NC core and a hybrid bilayer shell with precisely defined primary and secondary layer thicknesses (see Fig.1). The hydrophilic NC micelle surfaces would cause them to be water-soluble and allow further assembly or derivatization as depicted in Fig.1. Using gold NCs as a model system, we have demonstrated that for single-tailed surfactants, an alkane chain of eight or more carbons is required to form micelles with gold nanocrystals stabilized by C_{12} alkanethiols. Cationic, anionic, and non-ionic surfactants can all form NC-micelles. In addition, fluorescent semiconducting (e.g., CdSe etc.), magnetic (e.g., FePt, $FeMnO_4$ etc.) NCs, have been formed into NC-micelles with maintenance of optical and magnetic properties. NC-micelle solutions are colored and indefinitely stable (>2-years). By using a mixture of phospholipids containing head groups functionalized with polyethylene glycol (-PEG), carboxylic (-COOH),

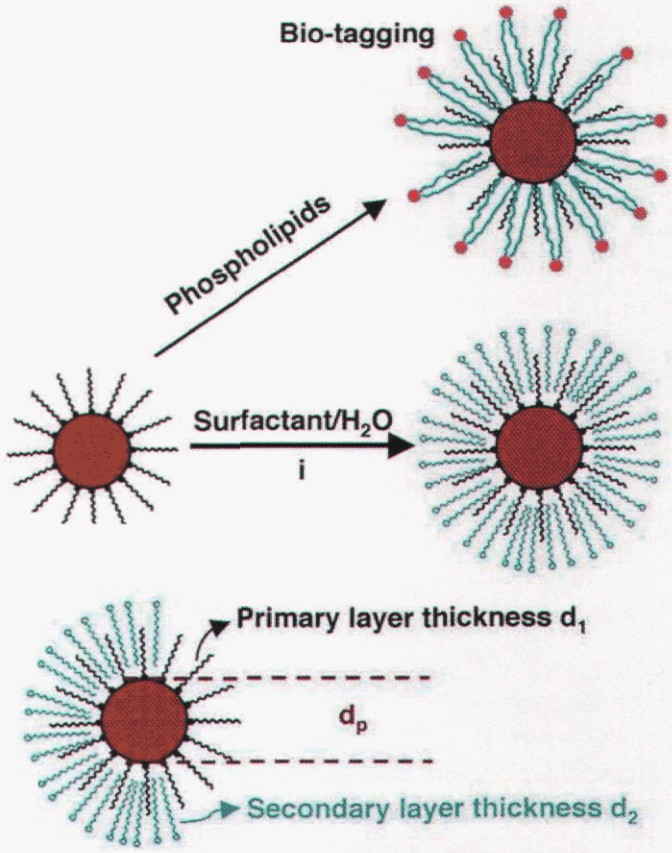

Figure 1. Thiol-stabilized nanocrystals encapsulated in surfactants to form water-soluble NC micelles (path I), or polyethylene glycol-surfactants or lipids can be used to prepare biocompatible water-soluble NC micelles for biolabeling. The lattice constant of the NC/silica superlattice is controlled by the nanocrystal size (d_p), the primary layer thickness of the alkanethiol, d_1, and/or the secondary layer thickness of the surfactant, d_2.

and amine (-NH_2) groups, we were able to synthesize water-soluble and biocompatible NC-micelles that can further conjugate with biospecies.

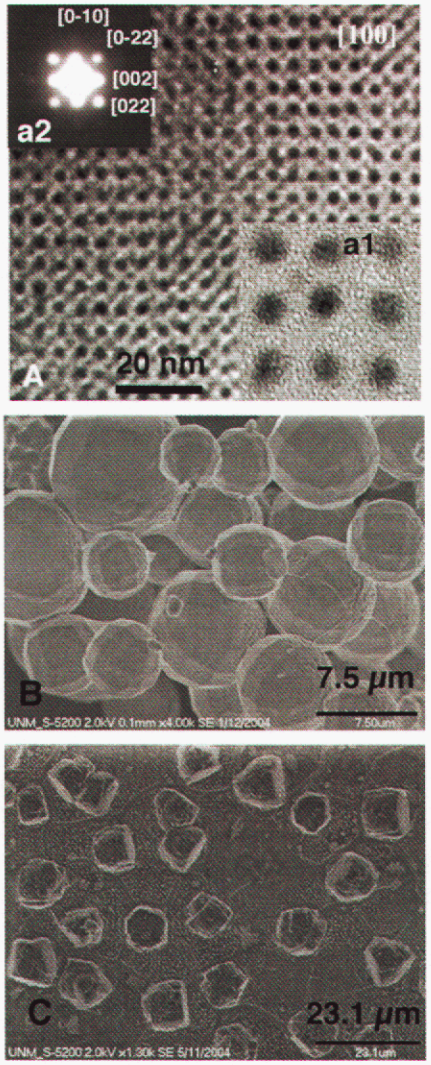

Figure 2. (A) [100] orientations of bulk samples. Inset (a1): high resolution TEM. Inset (a2): selected area diffraction pattern. (B) well-shaped superlattice solids. (C) Hierarchically ordered superlattice crystals on glass

We have synthesized a series of new NC/silica superlattice films and solids through self-assembly of water-soluble NC-micelles with silica. The superlattice comprises gold NCs arranged within a silica matrix in a face-centered-cubic lattice with unit cell dimensions that are adjustable through control of the nanocrystal diameter and/or the alkane chain lengths of the primary alkanethiol or the surrounding secondary surfactants. Under kinetically controlled silica polymerization conditions, highly orientated films, well-shaped solids (Fig.2), and hierarchically ordered superlattice crystals have been synthesized. Initial studies of charge transport within gold NC/silica superlattice films show non-linear current-voltage behavior at low temperature and complete Coulomb Blockade at 78k. Linear Arrhenius plot at zero bias conductance testifies both to the uniformity of NC sizes and to the dominance of charge transport mechanism at room temperature. Calculated activation energy is U=90.4mev. By measuring the *I-V* characteristics at T>the threshold temperature, we established for the first time current voltage scaling relationship for a well-defined 3-D array, $I \sim V^{2.9}$.

Significance: The new method invented is a very simple, one-step process to self-assemble hydrophobic nanocrystals into water-soluble micelles. The flexibility of incorporating functional groups on the outer micelle surface should enable these water soluble nanocrystal to efficiently couple with DNA or proteins for biomolecular tagging. The formation of highly ordered robust superlattice with controlled nanocrystal spacings, orientation, patterned features, and high particle loadings provides great opportunities in the development of new quantum solids with unique collective optical, electronic, and magetic properties.

Contact: Hongyou Fan, Ceramic Processing Inorganic Materials Dept.
Phone: (505) 272-7128
Fax: (505) 272-7336
Email: hfan@sandia.gov

Characterization, Optimization and Qualification of Piezoelectric Polymer Films for Novel Space Applications

M. Celina, T. Dargaville, P. Chaplya, R. Assink, J. Martin

Motivation: The challenge in designing novel large-aperture adaptive optics systems providing improved sensitivity and ground resolution for future space-based remote sensing systems is to identify suitable high performance thin film polymeric materials (the concept of using thin polymer films for novel space applications is shown in Fig. 1). The shape control in adaptive optics utilizes the responsiveness of piezoelectric polymers such as polyvinylidene fluoride (PVDF). Besides developing charge deposition control feedback loops and addressing engineering design issues, a detailed understanding of PVDF material changes and performance when exposed to vacuum UV irradiation, thermal cycling, atomic oxygen and other environmental factors in low earth orbit space environments is absolutely critical. Materials performance depends on primary polymer properties, copolymer type, film processing, molecular orientation, morphology and the applied poling technologies (piezoelectric optimization), as well as relative sensitivities to the various conditions in the space environment. There is no commercial material available that is optimized for the intended application. We are investigating the various features of many PVDF copolymers, and the accelerated degradation of these polymers to understand how piezo performance limitations depend on molecular structure, morphology and synergistic damage accumulation during radiation, temperature and atomic oxygen exposures.

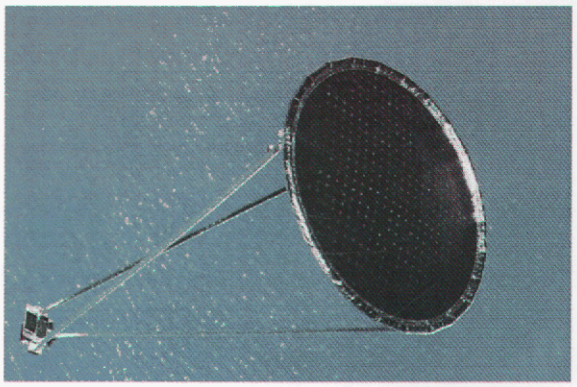

Figure 1. Photograph of a polymer film based inflatable antenna in orbit (taken from the space shuttle, Spartan 207, deployed May 1996)

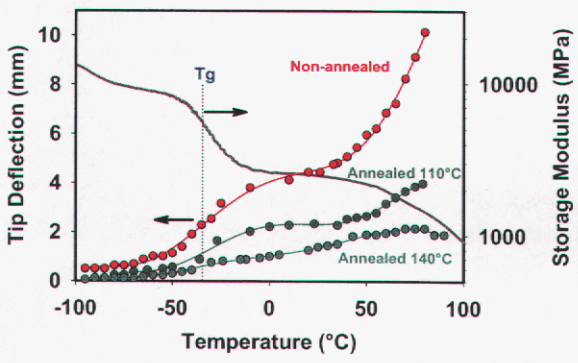

Figure 2. Influence of temperature exposure on piezoelectric responsiveness (deflection) of a PVDF homo-polymer.

Accomplishment: An extensive range of PVDF copolymers, manufactured films and piezo sensors has been obtained, their primary chemical and physical properties characterized, and their sensitivity to radiation and thermal exposures evaluated. These studies showed that the d_{33} piezoelectric coefficients (a measure of the change in polarization of the polymer in the thickness direction) for a series of commercially poled PVDF homopolymers and a TrFE (trifluoroethylene) copolymer aged using radiation, thermal treatment

or a combination of the two, is sensitive to a rapid depolarization process at elevated temperatures (>80°C). Some copolymers have shown better retention than others. Further experiments have focused on testing the magnitude of actual electromechanical responses of custom-made bimorphs over the temperature range of -100 to +130°C, to complement physical property measurements, such as d_{33} (an example of temperature effects is shown in Fig. 2). We have also conducted synergistic accelerated aging exposures measuring erosion rates of test specimens exposed to atomic oxygen and vacuum UV radiation, in collaboration with NASA Glenn. Based on these studies, the range of available polymers has been reduced to the two most promising materials, a PVDF homopolymer and a P(VDF-TrFE) copolymer with low (20%) comonomer content. This copolymer has the advantage that it can be solution processed and that an optically smooth surface is more easily obtained when cast onto an appropriate substrate. The erosion rates of both polymers due to AO/VUV exposure are at the upper end of the range for organic materials and pose a significant limitation to the lifetimes of the polymers (see Figure 3). Unexpectedly, the piezoelectric responses appear largely unaffected by the exposure to AO/VUV due to the bulk of the material remaining unchanged.

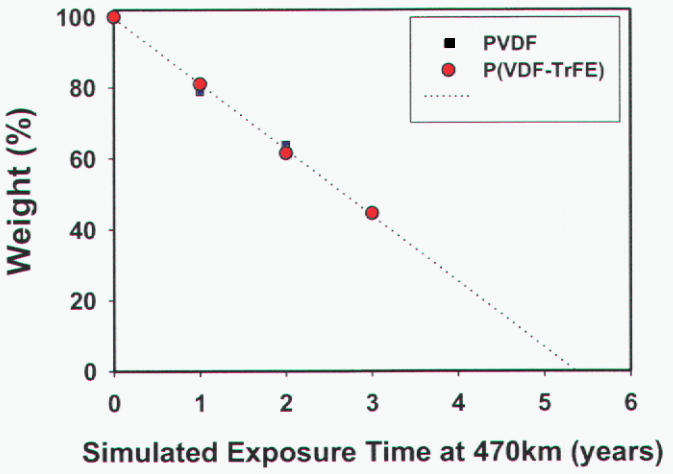

Figure 3. Limited lifetime of 30μm PVDF films due to significant erosion under combined AO/VUV exposure.

Significance: These fundamental studies have established the background for selecting a suitable material with long-term performance potential. The most important performance determining properties for this group of polymers have been identified. Through contacts at NASA Glenn and Boeing, we have been invited to participate in active material evaluation experiments on the outside of the International Space Station as part of the upcoming MISSE-6 mission. Preparation for these experiments has involved designing novel, small, robust excitation and sensing experiments capable of recording piezoelectric response remotely. Results from the MISSE-6 experiment, with plans for monitoring the piezoelectric performance over a period of 8 months in space, will offer the ultimate validation of ground testing and performance qualification for the real space environment.

Contact: Mathew Celina, Organic Materials Dept.
Phone: (505) 845-3551
Fax: (505) 844-9781
Email: mccelin@sandia.gov

Materials Synthesis

Computational Modeling of Thermally Responsive Surfaces

J. Curro, S. Mendez, J. McCoy, M. Kent, G. Lopez

Motivation: It is of technological interest to develop modified surfaces that are thermoresponsive and allow reversible modulation of surface properties with temperature. Surfaces grafted with Poly(N-isopropyl acrylamide) (PNIPAM) have been used in the past to reversibly switch wettability, adhesion of cells and proteins, and membrane porosity with temperature. Bulk, aqueous solutions of PNIPAM exhibit a lower critical solution temperature (LCST) near 30°C. Surfaces to which PNIPAM chains are tethered exhibit dramatic changes in hydrophobicity when heated through the LCST of the bulk solution. This can be observed in Figure 1 which shows the difference in contact angles at temperatures below and above the LCST. To help optimize this system for future applications, we used computational modeling to investigate how temperature affects the equilibrium structure.

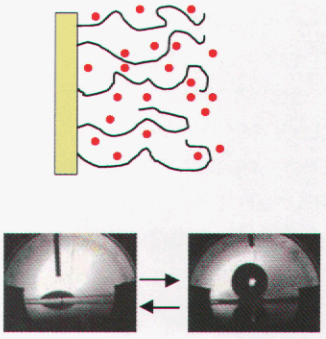

Fu et al *JACS* **126** 8904 (2004)

Figure 1. Top - A schematic depiction of PNIPAM chains tethered to a surface in the presence of water molecules. Bottom - A water drop on a cold surface (left) and hot surface (right)

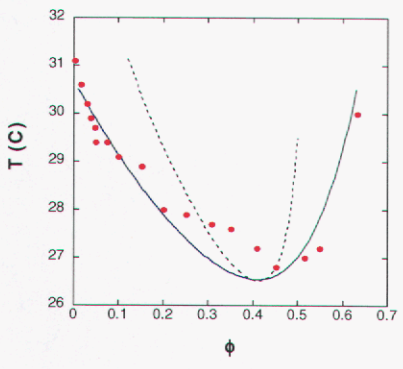

Afroze et al, *J. Mol. Struct.* **554**, 55 (2000)

Figure 2. The phase diagram of a bulk solution of PNIPAM in water. Note that the solution will phase separate into polymer-rich and solvent-rich phases when the solution is heated above the blue curve.

Accomplishment: We developed a self-consistent field theory (SCF) to compute the density distribution of monomers of PNIPAM chains tethered to a surface in the presence of water. As input to the SCF theory we used the experimental phase diagram of Afroze and coworkers shown in Figure 2. From this information, the theory predicts the concentration profile of polymer as a function of the distance z from the surface. Figure 3 shows our calculation of the concentration profiles over a range of temperatures that span the bulk coexistence curve. Note that at low temperatures the profile is broad indicating that the tethered PNIPAM chains extend into the water. As the temperature is raised the profiles gradually become narrower until, at 22°C, there is an abrupt change to a collapsed profile. These concentration distributions are qualitatively similar to profiles measured experimentally by M. Kent and H. Yim using neutron reflectivity. The sudden change from an extended to a collapsed density distribution is the manifestation of a first-order phase transition near the surface. As a result of the chain tethering constraint, the bulk phase diagram shown in Figure 2 becomes

distorted as shown in Figure 4 for the tethered system. The coexistence curve, shown by the red dashed line, suggests that the tethered chain phase diagram is of the *closed loop* type with both an upper and lower critical point. We have also calculated force-distance profiles at low and high temperature that are in agreement with atomic force microscope (AFM) measurements.

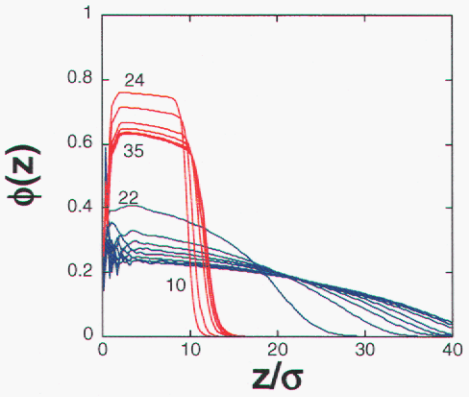

Figure 3. The computed PNIPAM volume fraction φ as a function of the distance from the surface over a range of temperatures from 10°C to 24°C

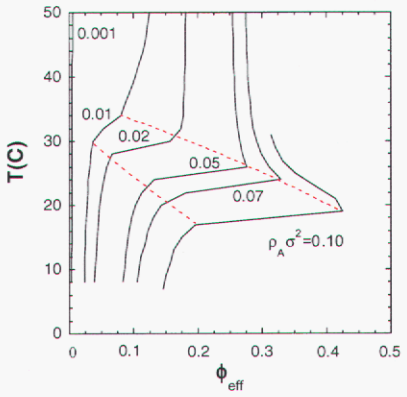

Figure 4. The calculated phase diagram of tethered PNIPAM chains in water. φ_{eff} is the average volume fraction of PNIPAM within the polymer layer. The solid curves correspond to lines of constant surface coverage. The red dashed line is an estimate of the coexistence curve.

Significance: We now have the capability to rapidly obtain polymer profiles, layer thickness, and forces on thermoresponsive surfaces modified with tethered PMIPAM chains. Such quantities are very difficult to measure experimentally. G. Lopez and coworkers have shown that these thermoresponsive surfaces can reversibly adsorb and desorb bacteria as the system is heated through the coexistence curve in Figure 4. This phenomenon suggests applications for bacterial sensors and water purification. Other applications for thermoresponsive surfaces exist in microfluidics and biotechnology.

Contact: John G. Curro, Ceramic Processing & Inorganic Materials Dept.
Phone: (505) 272-7129
Fax: (505) 272-7336
Email: jgcurro@sandia.gov

Development of Chemical Sensors Based on Magnetically Structured Composites

R.. Williamson, J. Martin

Motivation: Magnetic field structured composites (MFSCs) are anisotropic particle composites produced in a magnetic field. Samples are prepared by hosting magnetic particles (e.g. Ni) in a liquid monomer and polymerizing the mixture in the presence of a magnetic field. Various magnetic field configurations may be applied to produce MFSCs exhibiting chain, sheet-like, or complex three-dimensional structures (e.g. foams) possessing highly anisotropic properties that are sensitive to changes in specific volume. For example, stable, electrically conductive MFSCs can be produced having conductivities that show extreme sensitivity to strain, temperature, chemical and magnetic environment. Thus, MFSCs show great promise as inexpensive, sensitive sensors. Our goal is to construct practical chemical sensors that have reproducible, reliable response characteristics, and long shelf life. Prototype devices show immense changes in conductivity in response to relatively dilute flows of toluene in nitrogen, changing reversibly by 10-12 orders-of-magnitude at concentrations as low as 20 μg/mL. Our work is currently focused on exploring and learning how to tailor the sensor response characteristics, optimizing sensitivity, and exploring the effects of varying particle size, concentration, and polymer host.

Accomplishment: We have built several prototype sensor devices and tested their responses to dilute toluene vapors under different temperature conditions. The sensors were made by placing 4-7 micron diameter gold-coated nickel particles in silicone and polymerizing the mixture in a static magnetic field. Some example steady state response curves are shown in Figure 1 as a function of temperature. Note that the response broadens and the slope decreases as temperature is increased toward the cure temperature (55 °C). The sensors developed thus far have not been optimized for sensitivity.

Significance: MFSC sensor technology has the potential of enabling mass production of inexpensive, sensitive sensors, with long shelf life, that exhibit a reversible, extremely large response to small quantities of organic vapors. These sensors could be manufactured in a wide variety of shapes and sizes for various applications. A variety of polymer hosts could be used to tailor the response to different sizes and types of molecules. Arrays of such sensors could be produced and the array response patterns used to identify classes of organic molecules.

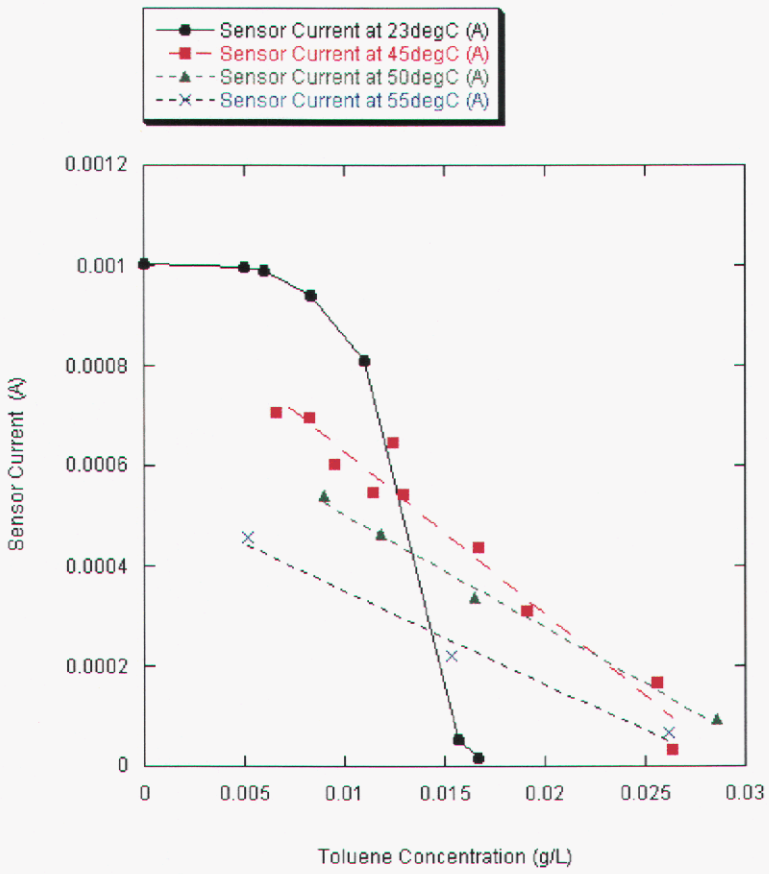

Figure 1. Plot of steady-state sensor current as a function of toluene vapor concentration at four different temperatures.

Contact: Rod Williamson, Chemical Synthesis & Nanomaterials Dept.
Phone: (505) 284-8223
Fax: (505) 844-9781
Email: rodwill@sandia.gov

Epoxidation of Olefins Using Homogeneous Catalysts

R. Kemp, K. Goldberg

Motivation: The Department of Energy has designated several difficult chemical transformations as "Holy Grails" in terms of economic impact if and when they are ever realized. High on the list is selective oxidation reactions using molecular oxygen as the oxidant. Selective oxidation reactions are considered especially demanding because the partially-oxidized products are significantly more reactive than the starting materials! It is extremely difficult to stop reactions prior to the thermodynamically favored state of total oxidation. However, if reaction pathways were designed that allowed these selective, partial oxidation reactions to occur, the economic advantages would be tremendous. Products that currently require multiple energy-intensive steps to prepare could be converted to one step syntheses, or more importantly, metal catalyzed reactions that require only organic feedstock, oxygen, and catalyst to prepare highly valued-added products. We have chosen to examine the partial oxidation of alkenes to prepare epoxides. While we are examining several alkenes, our intent is to prepare propylene oxide (PO) by direct oxidation of propylene with oxygen gas. We focus on this particular reaction due to the commercial significance of PO (over 12 billions lbs/yr).

Accomplishment: The core tenet of our proposed catalytic cycle is to use control of the active site architecture provided by molecular, homogeneous catalysts (Figure 1), instead of the more commonly used heterogeneous catalyst approach. While Ag is a well-known heterogeneous catalyst for epoxidation of ethylene and butadiene, it is not effective for other alkenes, thus new chemistry must be developed. In addition, if homogeneous catalysts are to be used, the ligand and catalyst system must be robust enough to withstand oxygen gas and the metal must be balanced to be equally effective in all steps of the catalytic cycle (otherwise, the reaction will not be catalytic). There is a class of ligands that are relatively air stable, the so-called pincer ligands. We have prepared a variety of pincer ligands complexed to late transition metals (Figure 2). In order to study the catalytic cycle more effectively, we have divided the cycle into individual component reactions that are easier to study. Using phosphorus-based pincer-Pd complexes (Figure 2 – compound a) we have demonstrated the reactivity of each step of the proposed cycle. PCP-Pd-H species can be easily prepared, and we have demonstrated that O_2 gas inserts into the Pd-H bond to form a Pd-OOH hydroperoxide (Figure 1, state 1 – 2). The reactivity of this species can be shown in that it transfers an O atom to

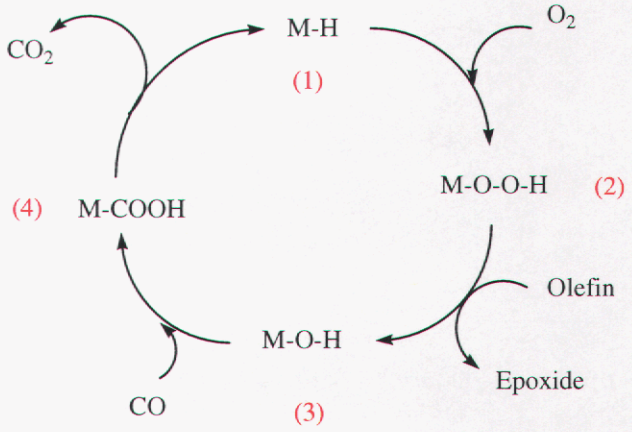

Figure 1. Proposed catalytic cycle for preparation of propylene oxide

acceptors such as phosphines and some alkenes like cyclohexene (state 2 – 3). The PCP-Pd-OH formed after O atom transfer can react with CO to form what we believe is a PCP-PD-COOH species (state 3 – 4). Interestingly, to our knowledge this reaction is without precedent – normally metal hydroxides add CO to yield formyl species, not carboxylates! In sealed systems, the PCP-Pd-COOH appears to eliminate CO_2 to regenerate our catalyst (state 4 – 1); however, this reaction appears to be reversible. Current efforts are underway to optimize this particular ligand/metal system for the complete reaction cycle, and to explore other ligand systems.

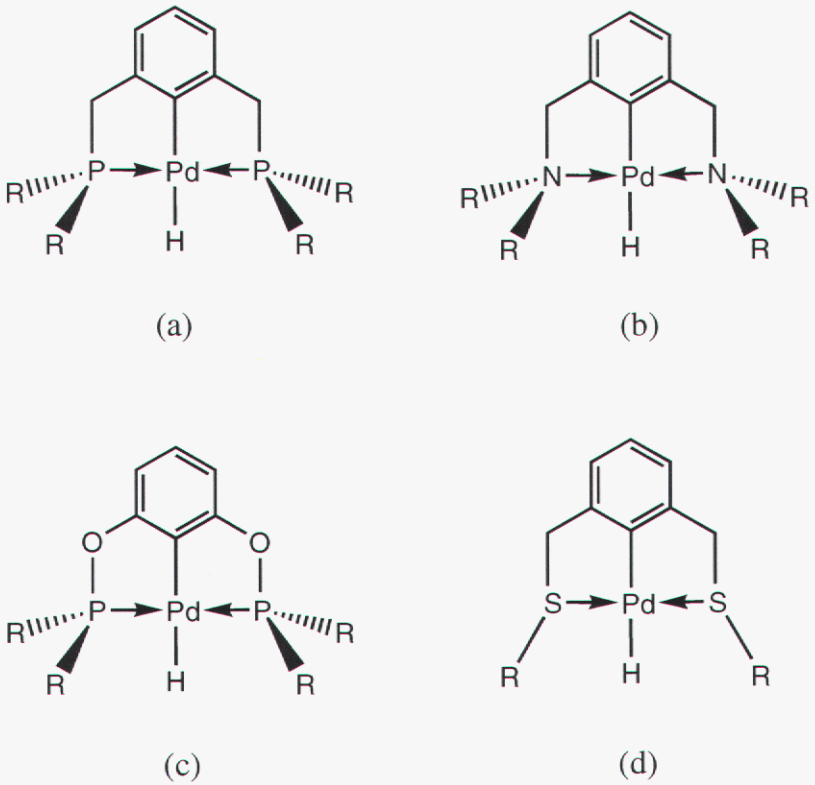

Figure 2. Some examples of pincer ligand – metal systems

Significance: We have made outstanding progress on this "Holy Grail" in a short time. Principles learned during this study should be applicable to other partial oxidation systems. If we can develop a singular system to catalyze this reaction, it should provide ample opportunities for Sandia to license this technology for PO and other partial oxidation processes.

Contact: Rick Kemp, Ceramic Processing & Inorganic Materials Dept.
Phone: (505) 272-7609
Fax: (505) 272-7336
Email: rakemp@sandia.gov

Non-Shrinking Materials Through Ring-Opening Polymerization (ROP)

K. Rahimian, C. Yun

Motivation: Sol-gel polymerization of tetraalkoxysilanes suffers considerable shrinkage from the net replacement of four alkoxide groups with two siloxane bonds per monomer repeat unit in the fully condensed silica gel, as well as the loss of the alkoxide groups themselves. This, coupled with the requirement of an alcohol or ethereal solvent to mix the hydrophobic monomer with two or more equivalents of water, leads to shrinkages of up to 95% during the air-drying of gels to afford xerogels. Shrinkage can be reduced by supercritical drying to afford porous aerogels or by performing "solvent-free" polymerizations with mixtures of tetralkoxysilane, water and catalyst to prepare porous xerogels. An even more elegant strategy uses monomers with the alkoxide groups modified to be polymerizable by either free radical or ring opening metathesis polymerization chemistry. This prevents shrinkage due to loss of volatile organic constituents, but does not compensate for shrinkage that comes from conversion of non-bonding distances between monomers to the higher densities arising from covalent linkages between monomers. These issues limit the utility of sol-gel materials in applications such as MEMS packaging and thin film applications such as conformal coatings.

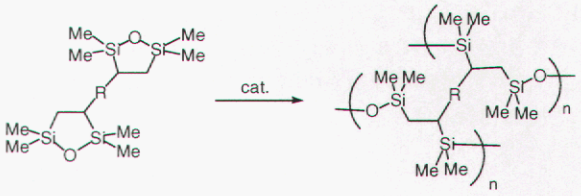

Scheme 1. Ring-opening polymerization of bridged disilaoxacyclopentanes to afford polycarboxosiloxane gels with four bonds to every monomer repeat unit (R = para-phenylene, meta-phenylene, ethylene, butylene, etc.).

One well-proven strategy for reducing shrinkage associated with the preparation of organic polymers is ring-opening polymerization of cyclic monomers such as epoxides, spirocarbonates, and cyclic ethers. Ring strain provides the thermodynamic driving force, the chain growth mechanism eliminates co-reactants (such as water), solvents and condensation products, and the ring-opened structure compensates for the volumetric losses resulting from the polymerization.

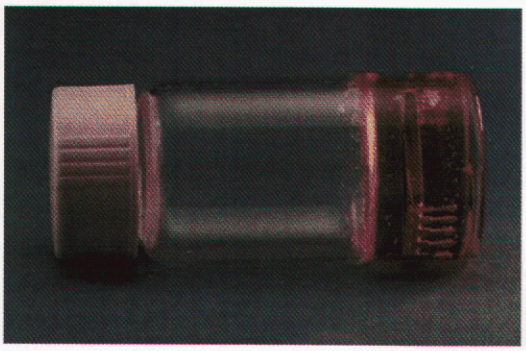

Figure 1. Test microchip encapsulated with a polydisilaoxacyclopentane.

Accomplishment: Bronsted base or acid-catalyzed, ring-opening polymerization (ROP) of bridged disilaoxacyclopentanes is a new, solvent-free alternative to sol-gel processing of highly cross-linked, hybrid organic-inorganic materials (Scheme 1). Using this synthetic methodology, a variety of monomers have been synthesized in our laboratory, which when polymerized, provide highly thermally stable, transparent, non-shrinking and VOC-free

polymers which have proven to be excellent candidates for MEMS packaging materials (Figure 1). ROP precursors can be polymerized using both Bronsted base and Bronsted acids, which allows for tailored polymerization where either acid or base is suitable/unsuitable. They can be polymerized using a variety of photo-acid generators, which allows for these materials to be used in lithography related applications as well as conformal coatings. We have demonstrated a variety of materials with easily tailorable thermal properties, from glassy materials (para-phenylene bridge) to materials with low Tg's (mixture of a bridged ROP precursor with 2,2,5,5-tetramethyl-2,5-disila-1-oxacyclopentane as a linear component).

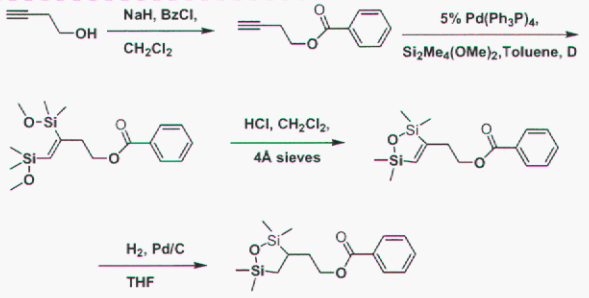

Scheme 2. Synthesis of benzoyl functionalized 3-butyn-1-ol bridged ROP precursor.

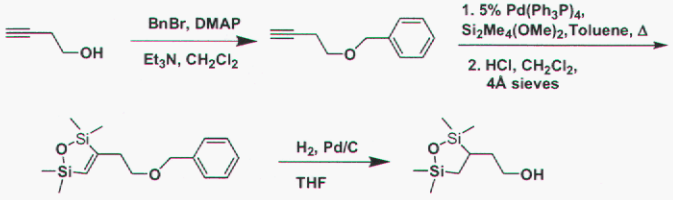

Scheme 3. Synthesis of benzyl protected ROP monomer.

We have recently synthesized functionalized (Scheme 2) and functionalizable (Scheme 3) ROP precursors, providing reactive sites introduced into the precursors at the beginning and at the conclusion of precursor synthesis. This should allow for introducing further functionalities into these materials and allow for the potential use in sensor type applications. Furthermore, this could allow for the introduction of thermally labile linkages into the final polymers, which will permit for thermally removing these materials. This is important because for instance, it will allow for potentially easy access to a MEMS device which has been encapsulated by the polymer.

Significance: Initial results show great promise for the use of ROP materials, polymers containing the stable siloxane bond, in packaging of MEMS devices based on their favorable properties: Thermal stability, transparency, no physical shrinkage, low/no VOC. Properties of these materials can easily be tailored based on the need and application and they can be polymerized using a variety of catalysts, including photo-acid generators which potentially allows for their use in applications such as conformal coatings.

Contact: Kamyar Rahimian, Organic Materials Dept.
Phone: (505) 844-7935
Fax: (505) 844-9624
Email: krahim@sandia.gov

Removable Encapsulants for Protecting Electromechanical Components

E. Russick, J. Aubert, P. Sawyer, T. Huber, M. Stavig

Motivation: Encapsulants are used in weapon systems to provide environmental protection and to mitigate shock and vibration of electromechanical components. However, when malfunctions of encapsulated systems take place or surveillance of stockpile units is necessary, conventional encapsulants are not removable except with aggressive solvents or by mechanical means. These removal techniques may damage sensitive equipment and mask long-term aging and reliability issues in the electromechanical system. For decades, there has been a desire for encapsulants that allow for damage-free removal so that malfunctioning components can be repaired or surveillance can be performed to assess the condition of aged components.

Accomplishment: The Materials and Process Sciences Center encapsulation team has developed removable encapsulants that allow for the repair and surveillance of components. Epoxy resins that incorporate Diels-Alder thermally-reversible adducts have been synthesized. These resins have been formulated with conventional resins and curatives into removable adhesives, coatings, and foams. The encapsulants can be removed by taking advantage of the reversible nature of the adducts, as shown in Figure 1. At low temperatures, the adducts are favored and the encapsulants have structures and properties similar to conventional epoxy encapsulants. At higher temperatures some of the adducts revert (open). If solvent is present, the open adducts can be solvated and then do not reform. Over time and in the presence of solvent, more and more of the adducts open and are solvated. Eventually the encapsulant can be dissolved in this manner.

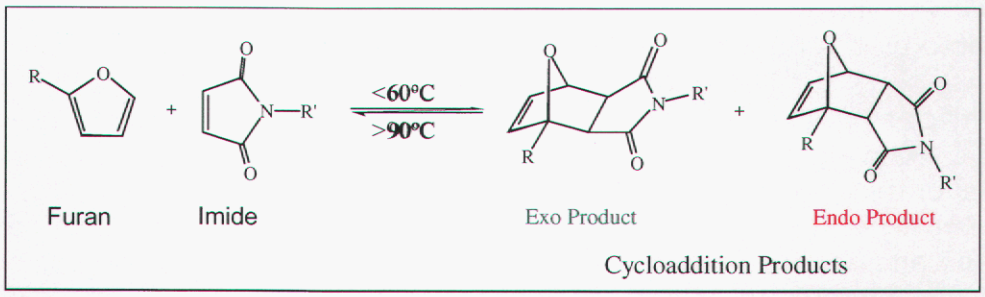

Figure 1. Diels-Alder thermally-reversible adduct equilibrium illustrates the removal mechanism.

FTIR with chemometrics has been utilized to characterize this reversible adduct formation. We found that the IR spectrum changes reversibly with temperature. Changes in the IR spectrum correspond to spectral regions associated with the adduct formation and reversion. The extent of adduct formation fits an Arrhenius equation. Encapsulant removal has been accomplish with two mild removal schemes; 1) 50 °C furfuryl alcohol, and 2) 90 °C 80% 1-butanol/20% toluene. The Arrhenius equation predicts that 3% of the adducts are open at 50 °C and 15% of

the adducts are open at 90 °C. Encapsulant removal occurs at approximately the same rate using either scheme because furfuryl alcohol partakes in the equilibrium through the furan/maleimide interaction shown in Figure 1.

Removable adhesives, coatings, and foam encapsulants, have been developed that use Diels-Alder thermally-reversible adducts as the removal mechanism. Encapsulant removal from electromechanical assemblies has been accomplished in cases where the units have experienced electrical failures. This allows for repairs or to recover expensive electrically functional components. An example of an encapsulant removal is shown in Figure 2. The removable encapsulant technologies have been transferred to Honeywell, KCP for production applications.

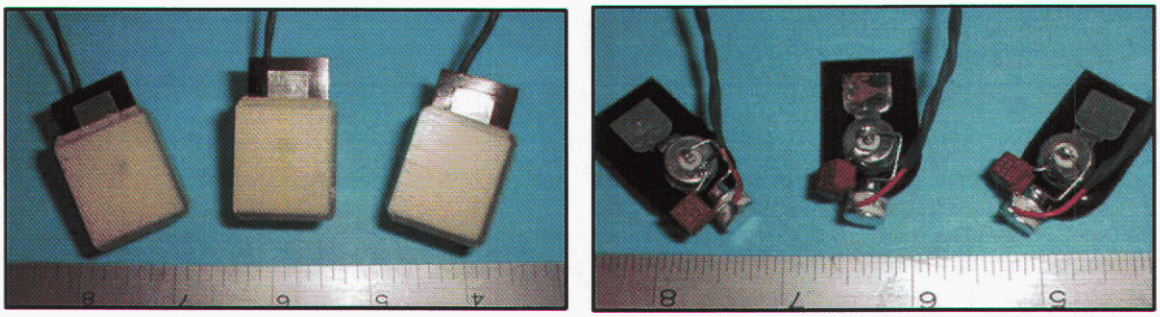

Figure 2. Functional electromechanical components encapsulated in removable epoxy foam (left), then after encapsulant removal with 90oC 1-butanol (right).

Significance: Removable encapsulants were developed to allow us to repair, upgrade, and perform surveillance on electromechanical components in weapon systems. Past systems used conventional non-removable encapsulants; thus, the units could not be easily repaired in the event of a system failure. Several major weapon systems are being refurbished and the new removable encapsulants have been chosen for use in these systems so that encapsulants can be more easily removed during development, production, and stockpile surveillance. The ability to remove encapsulants without undue damage to assemblies will allow for a better understanding of the reliability and aging of electromechanical systems and subsystems in the enduring weapons stockpile.

Contact: Ed Russick, Organic Materials Dept.
Phone: (505) 844-4357
Fax: (505) 844-9624
Email: emrussi@sandia.gov

Jim Aubert, Organic Materials Dept.
Phone: (505) 844-4481
Fax: (505) 844-9624
Email: jhauber@sandia.gov

Reversible Photonics

N. Bell

Motivation: Colloidal crystal arrays (CCAs) have been increasingly investigated for the potential formation of a full photonic bandgap. Based on the periodicity and the material properties, these materials can prevent the transmission of electromagnetic energy in a specified wavelength, and have applications as filters. These wavelengths have been demonstrated to cover the optical to infrared spectra. As such, these films can be used to mask thermal signatures. However, current methods for growth are limited to the cm^2 size range and are very slow. In the synthesis of these arrays, there are a number of processing difficulties including cracking due to drying stresses, misordered domains, and orientation control of the particle crystal lattice. A technological approach that allows for the formation of these films over large areas and minimizes the defects of the materials must be developed to realize the benefits of this technology.

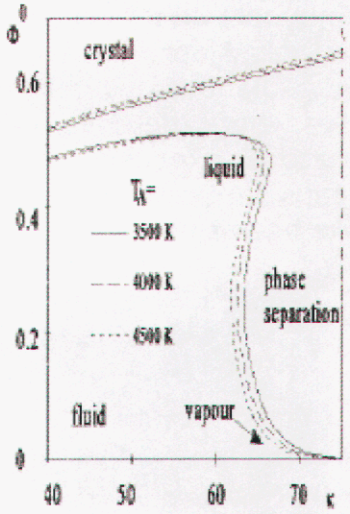

Figure 1. Phase diagram for ordering of colloids in electrostatically stabilized systems. J. Kaldasch, et al., Langmuir, 12, (1996) 6197-6201.

The process of nucleating a (single) crystal region and growing an ordered colloidal film is a difficult process based on kinetic constraints of controlling the phase space of increasing particle concentration, as shown in Figure 1. Operationally, there are additional concerns with surface defects, solvent-substrate wetting, evaporation rates, and the kinetics of nucleation and growth. As a result of the complications present from the kinetic nature of forming colloidal crystals, it will be manifestly improved if particles can be crystallized and melted reversibly. This would allow for directed deposition, orientation control and input of desired defects. This process requires reversible control over the adhesion and repulsion between colloidal particle components in the crystallization process. The approach to achieve this goal is the incorporation of photo-switchable groups in polymer layers grafted on the particles.

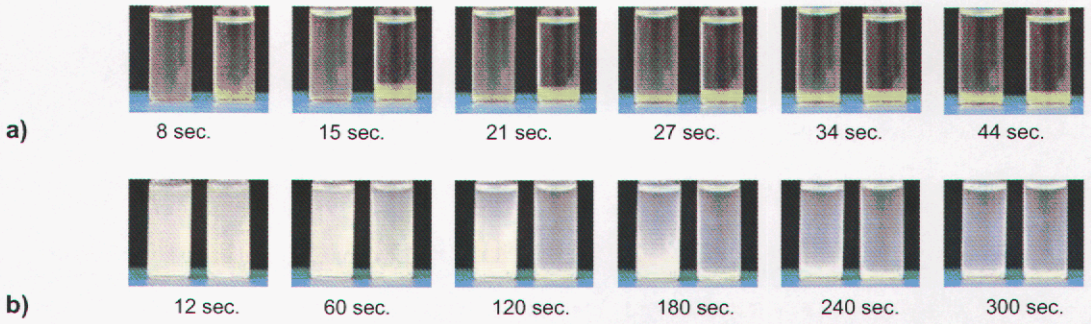

Figure 2. Aggregation/sedimentation behavior of 1 micron diameter silica particles modified with azobenzene monolayer and dispersed in a) cyclohexane, or b) toluene.

Accomplishment: Incorporation of these units into polymer grafted films has created photo-controlled systems where particle agglomeration can be directed and reversed externally by stimulation with the proper wavelength of light. Figure 2 shows the sedimentation behavior for 1 micron particles modified with azobenzene monolayers in cyclohexane and toluene solvent systems. Azobenzene is fairly nonpolar in the trans conformation, but becomes six time more polar when photostimulated into the cis conformation by UV light. In the series shown, the left vial is exposed to visible light, and the right to UV light for 15 minutes. Sedimentation is much faster after exposure to UV light in each system, due to the agglomeration of the particles into larger units.

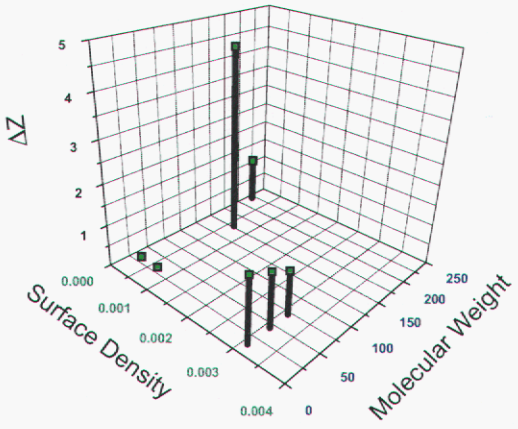

Figure 3. Expansion factors for planar films of PNIPAM as a function of surface density and molecular weight. (M. Kent, Org. 01812, SNL/NM)

For the response necessary for the directed deposition and control of colloidal crystallization, particles must both aggregate and disperse merely by the stimulation of light. This requires more than a change in surface polarity generated by photo-stimulated changes in the dipole moment of surface organic species. A polymer layer which can be directed through a phase transition should be able to change volume during photo-stimulation, and thereby undergo reversible attachment and removal. Figure 3 shows the thermally controlled phase behavior of poly(n-isopropyl acrylamide) (PNIPAM) layers grafted to surfaces. Based on properties such as molecular weight, surface density, and temperature, the layer can be compressed and expanded. This polymer has been investigated after incorporation of azobenzene units, and the phase transition can be shifted to room temperature and controlled externally.

Significance: Avenues for directing the deposition and removal of colloidal building units for the formation of photonic lattices are being explored and optimized. When fully successful, particle deposition can be initiated at desired locations allowing for the writing of photonic waveguides, and for the removal of defects in photonic lattices similarly to the process of zone refining in metals. We are continuing to build on our understanding of these systems and to optimize them for these purposes.

Contact: Nelson Bell, Chemical Synthesis & Nanomaterials Dept.
Phone: (505) 844-6234
Fax: (505) 844-9781
Email: nsbell@sandia.gov

DISTRIBUTION

	MS&T External Advisory Panel: 1 copy each				
	Dr. David J. Bishop Vice President of Nanotechnology Bell Laboratories Lucent Technologies 600 Mountain Ave. – Rm 6A-502 Murray Hill, NJ 07974			Professor Thomas Eagar Department of Materials Science & Engineering Massachusetts Institute of Technology 77 Mass. Ave, 4-136 Cambridge, MA 02139	
	Dr. Maxine Savitz 10350 Wilshire Blvd., #604 Los Angeles, CA 90024			Dr. Harry Saxton 11257 Golden Chestnut Place Las Vegas, NV 89135	
	Dr. Steven Wax, Deputy Director Defense Sciences Office DARPA/DSO 3701 N. Fairfax Dr. Arlington, VA 22203-1714			Professor John H. Weaver, Department Head Materials Science & Engineering University of Illinois 1304 W. Green Urbana, IL 61801	
	Dr. Thomas Zacharia Oak Ridge National Laboratory Computing and Computational Sciences PO Box 2008 MS-6163 Oak Ridge, TN 37831-6163			NOTE: MEMBERS OF EXTERNAL PANEL HAVE ALREADY RECEIVED CD'S OF THIS PUBLICATION. DO NOT SEND PRINT COPIES.	
1	MS 0102	J. Woodard, 2	1	MS 0186	K. Adams, 3000
1	MS 0513	J. P. Vandevender, 1000	1	MS 0143	R. Detry, 4000
1	MS 0323	H. Westrich, 1011	1	MS 1231	A. D. Romig, 5000
1	MS 0511	C. Adkins, 1020	1	MS 1202	A. Campbell, 5620
1	MS 1427	J. Phillips, 1100	1	MS 0970	A. Medina, 5700
1	MS 0121	T. Bickel, 1200	1	MS 1205	S. Gutierrez, 5900
1	MS 0185	D. Goldheim, 1300	1	MS 0724	L. Shepard, 6000
1	MS 1190	K Matzen, 1600	1	MS 0701	P. Davies, 6100
1	MS 1079	M. Scott, 1700	1	MS 0342	K. McCaughey, 6300
2	MS 0887	M. Cieslak, 1800	1	MS 9001	M. John, 8000
2	MS 0885	D. Dimos, 1810	1	MS-9153	D. Hensen, 8200
2	MS 0885	D. Salzbrenner, 1820	1	MS 1413	T. Michalske, 8300
15	MS 0885	J. Overall, 1820	1	MS 0885	G. Heffelfinger, 8330
1	MS 0886	S. Lott, 1812	1	MS 9403	J. Hruby, 8700
1	MS 0889	M. Hosking, 1813	1	MS 8750	G. Kubiak, 8750
1	MS 1411	H. E. Fang, 1814	1	MS 9161	W. Even, 8760
1	MS 1349	W. Hammetter, 1815	1	MS 9405	K. Wilson, 8770
1	MS 1411	J. Liu, 1816	1	MS 0151	T. Hunter, 9000
1	MS 0888	R. Clough, 1821	1	MS 0384	A. Ratzel, 9100
1	MS 0886	R. Goehner, 1822	1	MS 0825	W. Hermina, 9110
1	MS 0888	D. Wall, 1823	1	MS 0847	P. Wilson, 9120
1	MS 0889	J. Custer, 1824	1	MS 0134	J. Rice, 9700
1	MS 0889	J. Braithwaite, 1825	1	MS -112	F. Figueroa, 10000
1	MS 0865	D. Cook, 1900	1	MS 0960	G. Herrera, 14100
1	MS 0457	J. Stichman, 2000	1	MS 0961	M. Smith, 14100
1	MS 0429	J. Rottler, 2100	1	MS 0868	J. Sayre, 14400
1	MS 0509	M. Callahan, 2300	1	MS 1221	J. McDowell, 15000
1	MS 0503	D. Plummer, 2330			
1	MS 512	T. Blejwas, 2500			
1	MS 1453	W. Cieslak, 2501			
1	MS 0507	B. Walker, 2600	1	MS9018	Central Technical Files, 8945-1
1	MS 0121	C. Hart, 2800	2	MS0899	Technical Library, 9616